Study of Spin-Dependent ΛN Interactions by Gamma-Ray Spectroscopy of p-Shell Hypernuclei

A dissertation

by

MIFUYU UKAI

Submitted to

Department of Physics, Tohoku University

in partial fulfillment of the requirements

for the Degree of

Doctor of Science

February, 2004

Abstract

We performed γ-ray spectroscopy experiment on p-shell hypernuclei with Hyperball, a germanium detector array, at the BNL-AGS D6 line (BNL E930('01)). The purpose of the experiment is a determination of the strengths of all four ΛN spin-dependent interactions for p-shell hypernuclei. In the experiment, we took data for the ^{16}O $(K^-, \pi^-\gamma)$ and the ^{10}B $(K^-, \pi^-\gamma)$ reactions.

For the ΛN tensor interaction, we observed M1 transitions ($1^-\rightarrow 0^-$, $1^-\rightarrow 1^-$) from the 1_2^- state of $^{16}_{\Lambda}$O at 6.55 MeV and succeeded in a measurement of the ground state doublet spacing of $^{16}_{\Lambda}\mathrm{O}(1^-, 0^-)$ and a determination of the order of the spins. From the spacing, we derived a small value for the tensor force. It is the first time that information on the ΛN tensor force was experimentally obtained.

For the spin-spin interaction, we succeeded in measurements of the upper doublet spacing of $^{15}_{\Lambda}\mathrm{N}(\frac{1}{2}^+_2, \frac{3}{2}^+_2)$ based on the second 1^+ state of ^{14}N and of the upper doublet spacing of $^{7}_{\Lambda}\mathrm{Li}(\frac{7}{2}^+, \frac{5}{2}^+)$. We also obtained the upper limit of the ground doublet spacing of $^{10}_{\Lambda}\mathrm{B}(2^-, 1^-)$. Thus, we obtained information on the spin-spin interaction independent of the previous $^{7}_{\Lambda}\mathrm{Li}(\frac{3}{2}^+, \frac{1}{2}^+)$ data.

For the Λ-spin-dependent spin-orbit interaction, we succeeded in assigning the spins of the excited state doublet in $^{9}_{\Lambda}\mathrm{Be}(\frac{5}{2}^+, \frac{3}{2}^+)$. We confirmed the negative sign of the Λ-spin-orbit interaction.

For the nucleon-spin-dependent spin-orbit interaction, we succeeded in determining the excitation energies and spins of all of the bound state of $^{7}_{\Lambda}$Li. Then we deduced the strength of the N-spin-orbit interaction with high precision.

With those results, we determined the strengths of all the ΛN spin-dependent interactions.

Contents

List of Figures

List of Tables

Chapter 1

Introduction

A half century has passed since the first observation of Λ hypernuclei in nuclear emulsion exposed to cosmic rays. A decade after, reaction spectroscopy experiments started. Experimental techniques were developed, and the energy resolution of hypernuclear levels has been improved from several MeV to 1 MeV (FWHM). At the end of the last century, high precision γ-ray spectroscopy experiments on Λ hypernuclei using germanium detectors, the Hyperball project, started and achieved a few keV resolution, three orders of magnitude better than the resolution by reaction spectroscopy. In this century, the Hyperball project is taking a step forward to the next stage, γ-ray spectroscopy with the γ-γ coincidence technique and for various hypernuclei produced by baryonic decays of highly excited hypernuclei.

1.1 The study of Λ hypernuclei and ΛN interaction

Study of hypernuclei has three aspects: study of production, structure and decay. Study of hypernuclei is one way of investigating baryon-baryon interactions in which study of NN interaction is extended to studies of YN and YY interactions. We investigate the ΛN interaction through study of hypernuclear level structure. The goal of our study is a unified understanding of baryon-baryon interactions.

The effective ΛN interaction in a nuclear medium is reflected in the level structure of hypernuclei. The observed level structure can be used to obtain information on the effective ΛN interaction because the weakness of the ΛN interaction, which is relatively weaker than the NN interaction, and the lack of the Pauli principle for the Λ means that the Λ couples rather weakly to the core nucleus. The connection to the free YN interaction is made through the ΛN effective interaction which can be calculated from the free interaction by G-matrix method.

The forces between baryons are considered to be mediated by bosons. The long-range NN interaction is explained by one-pion exchange, but the short-range interaction, which is attributed to heavier meson exchange, is not understood well. Since baryons have internal structure, we should understand the short-range interaction in terms of the quarks in baryons. For the short-range interaction, such as the spin-orbit interaction, the quark models in which interaction is mediated by one gluon exchange seem to be plausible. The propriety of models should be determined by experimental data.

In order to investigate baryon-baryon interactions in terms of quarks, experimental information on interactions between baryons composed of u and d quarks, namely, the nuclear force, is not enough. The study of interactions between baryons with strange

quarks as well as u and d quarks is necessary for a unified understanding of baryon-baryon interactions.

In the meson-exchange picture, the baryon-baryon interactions including YN and YY interactions are described by SU(3) one-boson exchange (OBE) models which assume flavor SU(3) symmetry. The YN interaction data also tests the validity of the meson-exchange picture.

1.2 Historical background

The binding energy of a Λ in hypernuclei gives the depth of the potential which the Λ feels. In 1960s, the Λ-binding energies for the ground states of light hypernuclei were measured with nuclear emulsion with a mass resolution less than 100 keV. This is still the best method for determining the binding energy. However, available hypernuclei for emulsion experiments are limited to A $\leq$ 15 and only the binding energy of the ground state can be measured. Reaction spectroscopy with the (K^-, π^-) reaction started in 1960s, and with the (π^+, K^+) reaction started in 1980s. The reaction spectroscopy experiments opened a way to heavier hypernuclei. The (π^+, K^+) reaction, in particular, succeeded in the measurement of single-particle binding energies up to ${}^{208}_{\Lambda}$Pb due to its large momentum transfer. Thus, the nuclear potential depth for the Λ has been determined to be 30 MeV, about 2/3 of the potential depth for a nucleon, establishing the ΛN interaction that is weaker than the NN interaction.

The first data on the ΛN spin-dependent force was the observation of ${}^{4}_{\Lambda}$H, ${}^{4}_{\Lambda}$He $(1^+ \rightarrow 0^+)$ γ ray at 1 MeV. The level spacing of $(1^+, 0^+)$ gave the strength of the ΛN spin-spin force [1, 2]. The first indication of a small Λ-spin-dependent spin-orbit interaction was obtained by the spectroscopy of ${}^{16}_{\Lambda}$O via the (K^-, π^-) reaction [21] and the old γ-ray spectroscopy experiment of ${}^{9}_{\Lambda}$Be using NaI counters also reported a small strength [14].

The spin-dependent interaction between nucleons was successfully studied by elastic NN scattering experiments. The YN scattering experiments were also performed but the statistics are not yet good enough. Therefore, high resolution spectroscopy of hypernuclei is essential to study of YN spin-dependent interactions.

1.3 The spin-dependent Λ-N interaction

The effective ΛN interaction may be written as :

$$V_{\Lambda N} = V_0(r) + V_\sigma(r)\boldsymbol{s}_N \cdot \boldsymbol{s}_\Lambda + V_\Lambda(r)\boldsymbol{l}_{N\Lambda} \cdot \boldsymbol{s}_\Lambda + V_N(r)\boldsymbol{l}_{N\Lambda} \cdot \boldsymbol{s}_{\ N} + V_T(r)\mathbf{S}_{12}, \qquad (1.1)$$

where $\boldsymbol{l}_{N\Lambda}$ is the relative orbital angular momentum and

$$\mathbf{S}_{12} = 3(\boldsymbol{s}_N \cdot \hat{\mathbf{r}})(\boldsymbol{s}_\Lambda \cdot \hat{\mathbf{r}}) - \boldsymbol{s}_N \cdot \boldsymbol{s}_\Lambda$$

with $r = |\mathbf{r}_N - \mathbf{r}_\Lambda|$. The terms in Eq. 1.1 correspond to the spin-averaged central force, the spin-spin force, the Λ-spin-dependent spin-orbit force, the N-spin-dependent spin-orbit force and the tensor force, respectively. The strength of the spin-averaged central force is well known to be 2/3 of that of the nucleon-nucleon case from the systematic study of Λ binding energies. The other terms are the spin-dependent.

Low-lying levels of hypernuclei are described as follows. When the core nucleus $({}^{A-1}$Z) has a non-zero spin J, and a Λ particle in a $0s$ orbit is added to the core

nucleus, the state splits into spin-doublet states with the spins of $J + 1/2$ and $J - 1/2$ as shown in Fig. 1.1. Since the spin-doublet states have the same spatial wave functions, such an energy spacing of spin-doublet states is determined only by the spin-dependent terms in the ΛN interactions.

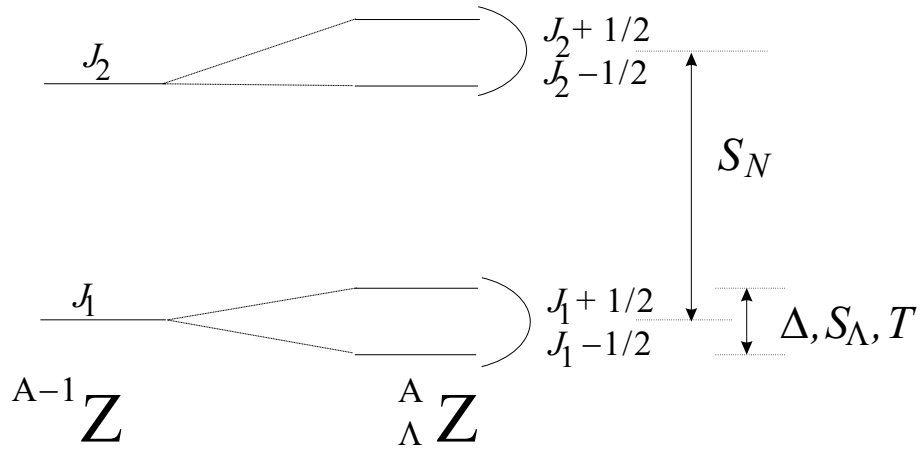

Figure 1.1: *Low-lying hypernuclear level structure and main contribution for the level energies*

Shell model approach

Here we explain a phenomenological approach to calculate hypernuclear levels with shell model which was first made by Dalitz, Gal and Soper [3, 4, 5] and then improved by Millener [6, 7, 8].

For p-shell hypernuclei, the radial integrals for the $p_N s_\Lambda$ shell-model matrix elements of each term in Eq. 1.1 are denoted as the parameters $\bar{V}$, Δ, S_Λ , S_N and T. For example, T is defined as

$$T = \int \phi^*_{\Lambda N}(\boldsymbol{r}) V_T(r) \phi_{\Lambda N}(\boldsymbol{r}) d\boldsymbol{r}. \tag{1.2}$$

Energies of low-lying levels of p-shell hypernuclei described by $\{s^4 p^{A-5} s_\Lambda\}$ configuration in the shell model can be expressed in terms of these five parameters. These parameters are taken to be approximately constant throughout the shell.

The energy spacing of the spin-doublet is determined mainly by Δ, S_Λ and T, while S_N changes the effective spacing of core levels. In addition, the contributions of these four terms to the energy spacings are different among levels and hypernuclei. Therefore, these four parameters can be determined by studying specific hypernuclear levels as follows. In the jj-coupling limit, the energy spacing of the spin-doublet states for $p^{-1}_{3/2} s_{1/2}$ at the beginning of p-shell such as ${}^{10}_{\Lambda}$B and ${}^{12}_{\Lambda}$C is expressed as

$$E(2^-) - E(1^-) = \frac{2}{3}\Delta + \frac{4}{3}S_\Lambda - \frac{8}{5}T, \tag{1.3}$$

while for $p^{-1}_{3/2} s_{1/2}$ at the end of p-shell such as ${}^{16}_{\Lambda}$O and ${}^{14}_{\Lambda}$N

$$E(1^-) - E(0^-) = -\frac{1}{3}\Delta + \frac{4}{3}S_\Lambda + 8T. \tag{1.4}$$

For the purpose of determining the tensor force, measurement of ground-state doublet of $p_{1/2}$-shell hypernuclei is suitable. Equations (1.3) and (1.4) given in the jj-coupling limit should be modified considering realistic nuclear structure. We refer to some hypernuclear structure calculations, in particular, to the shell-model calculations by D. J. Millener. He made shell model calculations for $\{s^4p^{A-5}s_\Lambda\}$ configurations using the interaction of Cohen Kurath for the core nucleus wave functions [25]. Then, Eq. 1.3 for ${}^{10}_{\Lambda}$B is modified as

$$E(2^-) - E(1^-) = 0.578\Delta + 1.414S_\Lambda + 0.014S_N - 1.068T \tag{1.5}$$

and Eq. 1.4 for ${}^{16}_{\Lambda}$O is modified as

$$E(1^-) - E(0^-) = -0.382\Delta + 1.378S_\Lambda - 0.004S_N + 7.850T. \tag{1.6}$$

The parameters Δ, S_Λ , S_N and T determined by comparing experimental data and shell model calculations can be then compared with the ΛN interaction models in free space, such as the meson-exchange models of the Nijmegen and Julich groups and quark models, through G-matrix calculations.

Experimental determination of parameters

An energy spacing of the ground-state doublet of p-shell hypernuclei is expected to be typically as small as a few hundreds keV or a few tens keV, and it is called hypernuclear fine structure. The first experimental determination of the ground-state doublet spacing of hypernuclei was made for the s-shell hypernuclei, ${}^{4}_{\Lambda}$H and ${}^{4}_{\Lambda}$He using NaI counters [1, 2]. The spacings for these s-shell hypernuclei are 1.1 MeV. Some γ-ray spectroscopy of p-shell hypernuclei were performed using NaI counters, but the ground-state doublet separations could not be measured because of the limited energy resolution [14]. Thus, keV-resolution spectroscopy of hypernuclei has been long awaited to resolve the hypernuclear fine structure. A germanium detector array, Hyperball, was built for the purpose of precise measurement of hypernuclear structure, and of determination of all the spin-dependent interactions.

1.3.1 The spin-spin force

The first experimental data which gave the information on the spin-spin force was the γ-ray spectroscopy of ${}^{4}_{\Lambda}$H and ${}^{4}_{\Lambda}$He using NaI counters via stopped K^- absorption [1, 2]. Each spin-flip M1 transition of the ground-state doublet ($1^+ \to 0^+$) was observed with an energy of about 1.1 MeV. This result provided $\Delta \sim 0.5$ MeV in the calculation by Millener et al. [6]. However, since the three-body ΛNN effect is expected to be large for this spacing, the strength of the spin-spin force was not definitely determined.

For p-shell hypernuclei, the spin-flip M1 transition between the ground-state doublet of ${}^{7}_{\Lambda}$Li($\frac{3}{2}^+ \to \frac{1}{2}^+$) was observed using Hyperball via the (π^+, K^+) reaction. The ground state of the core nucleus ^{6}Li(1^+) has an almost pure ${}^3S_1$ configuration and thus the ground-state doublet spacing is dominantly determined by the spin-spin force. The measured spacing energy of 692 keV determined the strength of the ΛN spin-spin force, Δ, to be 0.5 MeV [9, 10]. On the other hand, an old γ-ray spectroscopy experiment using germanium detectors reported that the spin-flip M1 transition between the ground-state doublet of ${}^{10}_{\Lambda}$B($2^- \to 1^-$) was not observed and that result corresponded to $\Delta < 0.2$ MeV [11]. To clarify this inconsistency is important.

1.3.2 The spin-orbit force

The γ-ray spectroscopy experiment on ${}^{9}_{\Lambda}$Be using Hyperball via the (K^-, π^-) reaction determined S_Λ [12]. It reported that the spacing energy of the spin-doublet states $(\frac{5}{2}^+, \frac{3}{2}^+)$ of ${}^{9}_{\Lambda}$Be, which is described as Λ coupled to the 3040 keV excited state (2^+) of ^{8}Be, is about 43 keV. The spacing corresponds to the spin-orbit strength $\mid S_\Lambda \mid < 0.03$ MeV [12, 13]. This result supports quark models predicting very small values ($\sim$ 0.0 MeV) and does not support one-boson exchange models predicting with large values ($\sim$ 0.15 MeV) [33]. The spins of the spin-doublet states $(\frac{3}{2}^+, \frac{5}{2}^+)$ could not be determined in this experiment because the cross section to populate each state is predicted to be almost the same by the (K^-, π^-) reaction. Therefore, the sign of S_Λ is not determined from this experiment.

For the other spin-orbit force, a value of $S_N = -0.4 \sim -0.5$ MeV was suggested by measurements on the core excited states such as ${}^{7}_{\Lambda}$Li $({}^{6}\mathrm{Li}(3^+)\otimes s_\Lambda)$ [15, 14] and ${}^{13}_{\Lambda}$C $({}^{12}\mathrm{C}(2^+)\otimes s_\Lambda)$ [16]. However, for each case the energy of only one of the spin-doublet members was measured. For more precise determination of S_N, it is necessary to measure the centroid energy of hypernuclear doublets. In other words, it is necessary to measure all the energies and the spins for the states of $j_1 \pm 1/2$ and $j_2 \pm 1/2$ in Fig. 1.1.

1.3.3 The tensor force

There are no experimental data which give information on the ΛN tensor force before the present experiment (E930('01)). The strong tensor force in NN interaction is well understood by one-pion exchange. But the case of ΛN interaction, one-pion exchange is forbidden because of isospin conservation. However, other contributions for the tensor force such as kaon exchange and two-pion exchange with ΛN-ΣN mixing are expected. Meson-exchange models predict small strengths of the tensor force, T, of the order of a few tens keV in G-matrix calculations. The predicted values of T are summarized in Table 1.1. The difficulty of determining the tensor force strength is not only due to its small value, but also to the small spacing of spin doublets in hypernuclei. T is expected to have a small positive value, and Δ have a relatively large positive value. Therefore, as seen in Eq. 1.4, the contributions of Δ and T are expected to cancel strongly in the $p_{1/2}$-shell hypernuclei.

Table 1.1: *The strength of the tensor force [7]*

models	ND	NF	NSC89	NSC97f
T [MeV]	0.018	0.033	0.036	0.054

1.4 The effect of the ΛNN three-body force

Recently, Akaishi et al. solved the so-called overbinding problem for the ${}^{5}_{\Lambda}$He hypernucleus [18]. They found that the ΛNN three-body force due to the Λ-Σ coupling makes the ground state (0^+) energy of ${}^{4}_{\Lambda}$H and ${}^{4}_{\Lambda}$He lower but does not change the ground state $(\frac{1}{2}^+)$ energy of ${}^{5}_{\Lambda}$He. This is why previous calculations which fit the A=4 binding energy overestimated the A=5 binding energy. Figure 1.2 shows the diagram of the ΛNN three-body force. The extended calculation from s-shell to p-shell hypernuclei

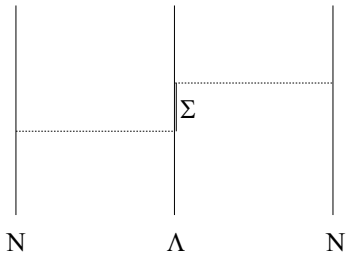

Figure 1.2: *Diagram for the ΛNN three body force*

was performed by Millener [27], in which the Nijmegen interaction was assumed and G-matrix calculation was made. The energy shift of the hypernuclear states is expected to be smaller than those for A = 4 system and limited to about 150 keV. Including this approach, Δ is estimated to be 0.45 MeV from the ${}^{7}_{\Lambda}$Li $(\frac{3}{2}^{+}, \frac{1}{2}^{+})$ spacing [8, 27].

Another shell model approach was suggested by Fetisov. It includes zero-range effective ΛNN force inferred from a Λ-nucleus description of *s*-shell hypernuclei in addition to the spin-dependent forces [17]. This calculation derived Δ of about 0.3 MeV and seems to explain both results of ${}^{7}_{\Lambda}$Li and ${}^{10}_{\Lambda}$B.

1.5 Motivation and purposes of the present experiment

The ΛN spin-dependent interactions have been studied with Hyperball experiments and the parameters of Δ, S_Λ and S_Λ were already determined. In the present experiment (BNL-E930('01)), the purposes are determination of the strength of the tensor force by the ^{16}O$(K^-, \pi^-\gamma)$ reaction and consistency check of the strengths of the other terms by the ^{10}B$(K^-, \pi^-\gamma)$ reaction. ${}^{16}_{\Lambda}$O and ${}^{10}_{\Lambda}$B hypernuclei including their unbound states, were produced by the (K^-, π^-) reaction with kaon momentum of 0.93 GeV/c and with the spectrometer covering pion scattering angles of roughly 2 to 12 degree. In this condition, due to the medium momentum transfer of about 150 MeV/c, both of the $\Delta L = 0$ and 1 states can be produced. The bound states of ${}^{16}_{\Lambda}$O and ${}^{10}_{\Lambda}$B, and the proton unbound states of ${}^{10}_{\Lambda}$B are produced by a $\Delta L = 1$ reaction, in which a neutron in *p*-orbit is replaced by a Λ in *s*-orbit to make the configuration $(p_j)_n^{-1}(s_{1/2})_\Lambda$. With the $\Delta L = 0$ reaction, a neutron in *p*-orbit or *s*-orbit is replaced by the Λ in the same orbit, in which the configurations of $(p_j)_n^{-1}(p_j)_\Lambda$ or $(s_{1/2})_n^{-1}(s_{1/2})_\Lambda$, called substitutional state, are produced. Such substitutional states are usually particle unbound states and partly decay to lighter hypernuclei called hyperfragments.

1.5.1 The ^{16}O $(K^-, \pi^-\gamma)$ reaction

Motivation

The measurement of the ground-state doublet spacing of $p_{1/2}$-shell hypernuclei is suitable for the study of the ΛN tensor force. In the ^{16}O (K^-, π^-) reaction, both ${}^{16}_{\Lambda}$O and ${}^{15}_{\Lambda}$N can be produced. The ${}^{15}_{\Lambda}$N hypernucleus can be produced via proton emission from substitutional states (0^+) of ${}^{16}_{\Lambda}$O.

In a precise calculation by Millener [27], based on shell model with Cohen-Kurath effective interaction [25] for the core nuclei, ^{15}O and ^{14}N, the spacing energies are given

by

$$^{16}_{\Lambda}\mathrm{O}:\ E(1^-) - E(0^-) = -0.382\Delta + 1.378S_\Lambda - 0.004S_N + 7.850T + \Lambda\Sigma$$

$$^{15}_{\Lambda}\mathrm{N}:\ E(\tfrac{3}{2}^+) - E(\tfrac{1}{2}^+) = -0.756\Delta - 2.25S_\Lambda + 0.035S_N - 9.862T + \Lambda\Sigma$$

where $\Lambda\Sigma$ is the shift energy from Λ-Σ coupling. Applying the already determined values of Δ, S_Λ and S_N and the predicted value of T, we obtained the expected value of the energy spacing. Millener modified the experimentally determined parameters to take into account the nuclear size effect for $^{16}_{\Lambda}$O and $^{15}_{\Lambda}$N. He suggested the parameter set as follows,

$$\Delta = 0.47, \quad |S_\Lambda| < 0.03, \quad S_N = -0.35 \quad [\mathrm{MeV}]$$

and $\Lambda\Sigma$ is -31 keV for $^{16}_{\Lambda}$O and 46 keV for $^{15}_{\Lambda}$N. Then the spacing energies of -50 to 290 keV for $^{16}_{\Lambda}$O and -150 to 295 keV for $^{15}_{\Lambda}$N were obtained. If the spacing energy is larger than 100 keV, we can detect the spin-flip M1 transitions between the doublet states, and if the spacing energy is larger than 20 keV, we can measure the difference of energies between the two M1 transitions from an upper excited state to both of the ground-state doublet members.

Production

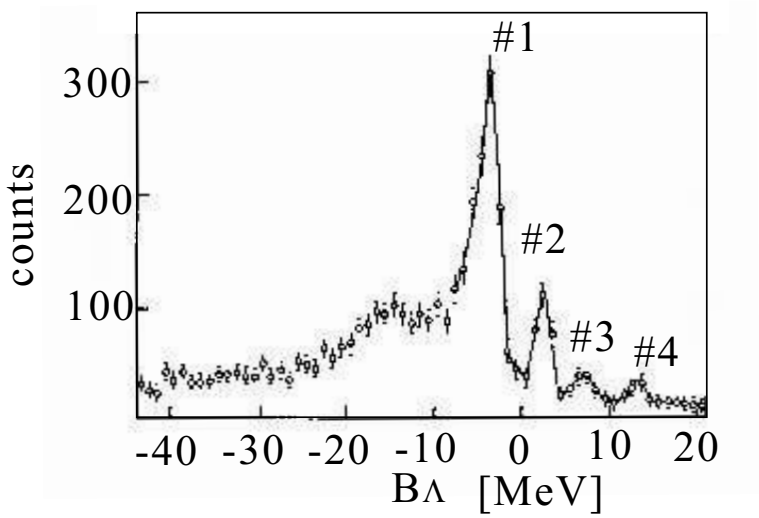

Figure 1.3: *Mass spectrum of $^{16}_{\Lambda}O$ by the (K^-, π^-) reaction at 0 degree with p_K = 0.715 GeV/c [21]. Dominant configurations and spins are #1: $(p_{3/2})_n^{-1}(p_{3/2})_\Lambda\ 0^+$, #2: $(p_{1/2})_n^{-1}(p_{1/2})_\Lambda\ 0^+$, #3: $(p_{3/2})_n^{-1}(s_{1/2})_\Lambda\ 1^-$, #4: $(p_{1/2})_n^{-1}(s_{1/2})_\Lambda\ 1^-$, and the broad peak around -15 MeV: $(s_{1/2})_n^{-1}(s_{1/2})_\Lambda\ 0^+$.*

Figure 1.3 is the mass spectrum of $^{16}_{\Lambda}$O as a function of B_Λ[1] via the (K^-, π^-) reaction with a kaon momentum of 0.715 GeV/c at 0 degree measured in an old experiment [21]. The main configuration and spin of each peak is $(p_{3/2})_n^{-1}(p_{3/2})_\Lambda\ 0^+$ for #1, $(p_{1/2})_n^{-1}(p_{1/2})_\Lambda\ 0^+$ for #2, $(p_{3/2})_n^{-1}(s_{1/2})_\Lambda\ 1^-$ for #3, $(p_{1/2})_n^{-1}(s_{1/2})_\Lambda\ 1^-$ for #4,

[1]The binding energy of a Λ in a hypernuclei, B_Λ is defined as $B_\Lambda = M_{hypernucleus} - M_{core} - M_\Lambda$. Details are described in Section 3.7.1

and $(s_{1/2})_n^{-1}(s_{1/2})_\Lambda$ 0^+ for a broad peak around -15 MeV. The peaks of #1 and #2 corresponding to the substitutional state were strongly populated with a small momentum transfer. In the case of 0.93 GeV/c momentum, the same states as in Fig. 1.3 are expected to be produced with different cross sections. Figure 1.4 shows the calculated cross sections by Motoba [26] of these four states at 0.9 GeV/c momentum.

Figure 1.5 shows the expected level schemes, γ transitions and proton emission schemes on ${}^{16}_{\Lambda}$O and ${}^{15}_{\Lambda}$N produced by the ^{16}O (K^-, π^-) reaction. The detailed structure and the experimentally obtained excitation energies and calculated excitation energies of ${}^{16}_{\Lambda}$O are shown in Fig. 1.6. The calculated excitation energies and the calculated lifetimes of ${}^{15}_{\Lambda}$N are shown in Fig. 1.7. Although the binding energy of ${}^{15}_{\Lambda}$N is not well determined[2], it is suggested that the mass of ${}^{15}_{\Lambda}$N+p threshold is as high as about 7.8 MeV from the ground state of ${}^{16}_{\Lambda}$O according to the binding energy relation between ${}^{A}_{\Lambda}$Z and ${}^{A-1}_{\Lambda}$Z [3]. Therefore, the 1^-_2 state of ${}^{16}_{\Lambda}$O is expected to be a particle bound state.

When the ground-state doublet spacing is smaller than 100 keV, it is difficult to detect the spin-flip M1 transition between the doublet states because of competition with the weak decay and a small Hyperball sensitivity. Since the excited states of ${}^{16}_{\Lambda}$O (1^-_2) and ${}^{15}_{\Lambda}$N $(\frac{1}{2}^+;$T=1) are expected to be produced, we can separately measure the M1 transitions to both of the ground-state doublet members, ${}^{16}_{\Lambda}$O$(1^-_2 \rightarrow 1^-_1, 1^-_2 \rightarrow 0^-)$ and ${}^{15}_{\Lambda}$N$(\frac{1}{2}^+;$T=1$\rightarrow$ $\frac{1}{2}^+_1$, $\frac{1}{2}^+;$T=1$\rightarrow$ $\frac{3}{2}^+_1$) if the spacing is larger than 20 keV and the branching ratio to both states are large enough.

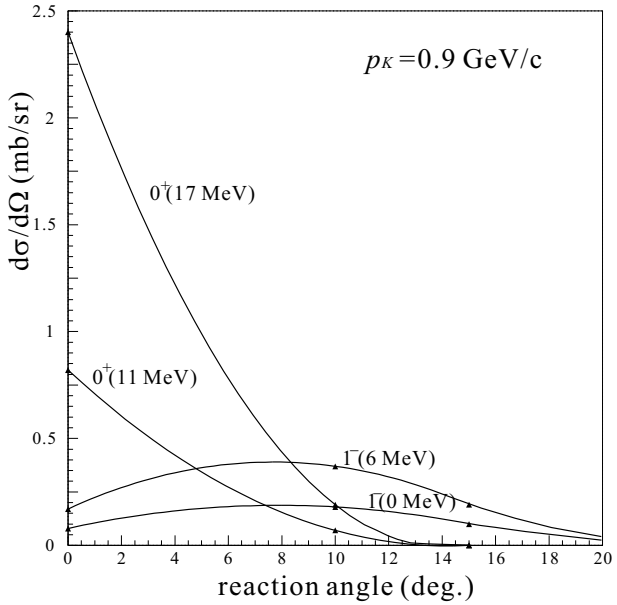

Figure 1.4: *Calculated cross section of the ${}^{16}O(K^-, \pi^-)$ ${}^{16}_{\Lambda}O$ reaction at 0.9 GeV/c by Motoba [26].*

[2]The binding energy of ${}^{15}_{\Lambda}$N was reported in old emulsion data [40]. However, one of the authors (Davis) has later argued this value is almost certainly wrong [28].

[3]Millener suggested the binding energy of ${}^{15}_{\Lambda}$N to be 12.3 MeV, by calculating it from well determined binding energy of ${}^{14}_{\Lambda}$N and relation between ${}^{13}_{\Lambda}$C and ${}^{12}_{\Lambda}$C, etc. [27]

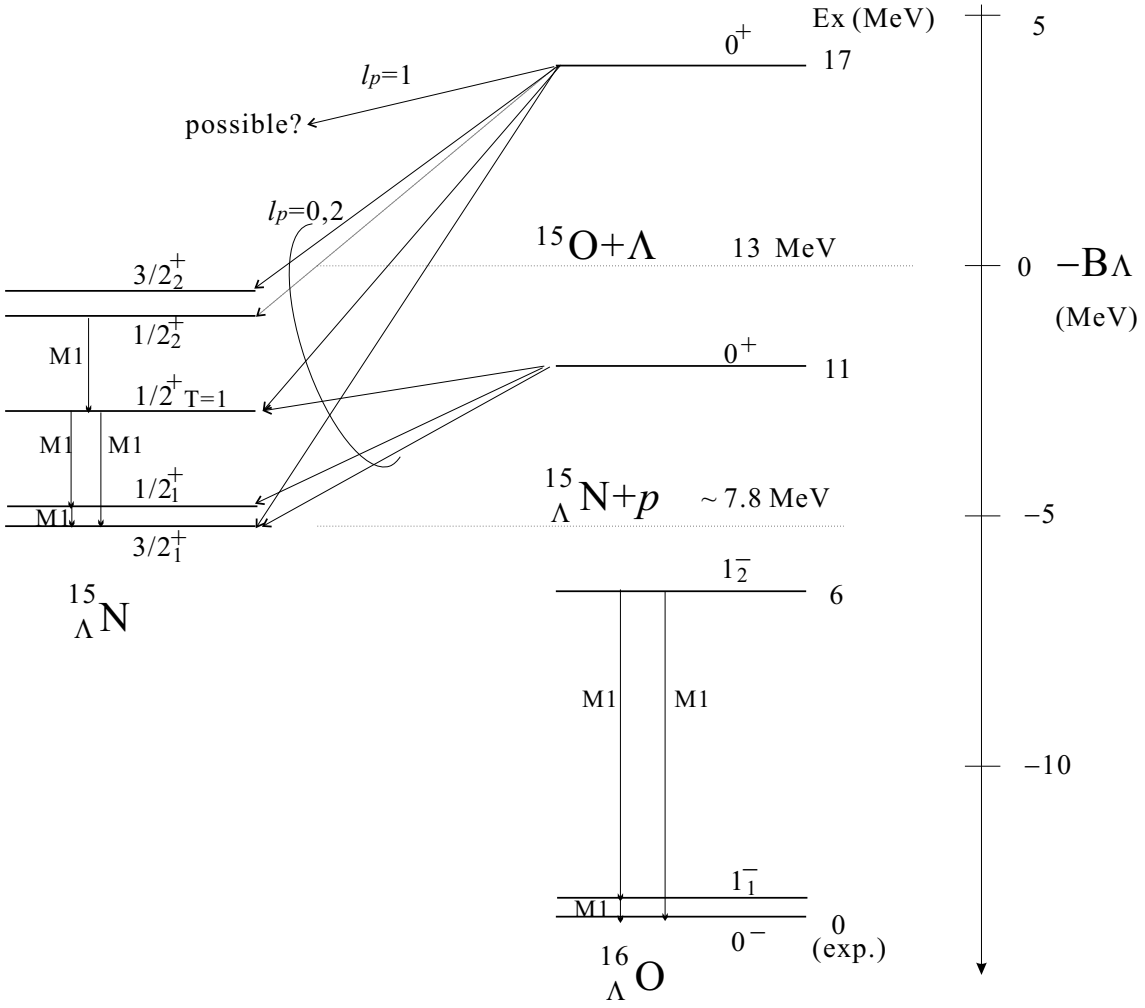

Figure 1.5: *Expected level schemes, γ-transitions and proton emissions of $^{16}_{\Lambda}O$ and $^{15}_{\Lambda}N$ produced by the $^{16}O(K^-,\pi^-)$ reaction. The 1^- and the 0^+ states of $^{16}_{\Lambda}O$ are directly produced by 0.9 GeV/c (K^-,π^-) reaction. The calculated cross section of each state is given in Fig 1.4. Although the binding energy of $^{15}_{\Lambda}N$ is not well determined, the 6 MeV excited state (1_2^-) is expected to be bellow the proton emission threshold.*

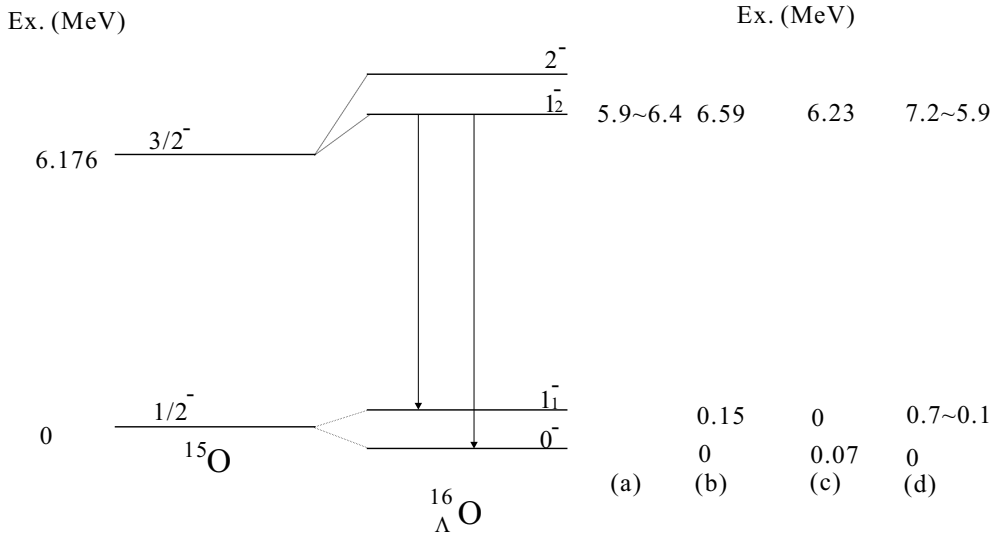

Figure 1.6: *Expected level scheme of* ${}^{16}_{\Lambda}O$ *with experimentally measured and theoretically calculated excitation energies. (a) Experiment by the* (K^-, π^-) *and the* (π^+, K^+) *reactions [19, 20, 21, 22], (b) calculation by Millener [8], (c) calculation by Itonaga et al. [23] and (d) calculation by Fujii et al. [24]*

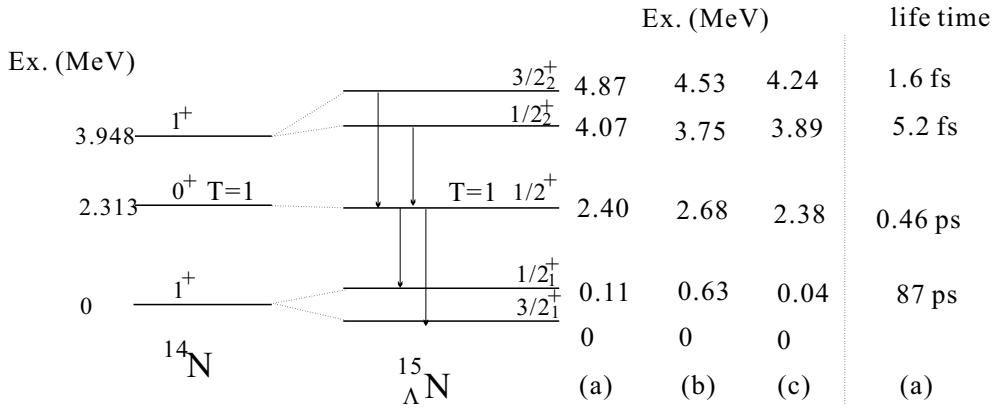

Figure 1.7: *Expected level scheme of* ${}^{15}_{\Lambda}N$ *with calculated excitation energies and lifetimes. (a) Calculation by Millener, (b) calculation by Itonaga et al. [23], and (c) calculation by Fetisov [17].*

1.5.2 The ^{10}B$(K^-, \pi^-\gamma)$ reaction

Motivation

The measurement of the ground-state doublet spacing of $^{10}_{\Lambda}$B is important as already mentioned. The spacing energy of the ground-state doublet is given by [8]

$$^{10}_{\Lambda}\mathrm{B}: \quad E(2^-) - E(1^-) = 0.578\Delta + 1.414S_\Lambda + 0.014S_N - 1.068T + \Lambda\Sigma,$$

where $\Lambda\Sigma$ is estimated to be -15 keV. We used the parameter set as,

$$\Delta = 0.46, \quad |S_\Lambda| < 0.03, \quad S_N = -0.43, \quad T = 0.02 \sim 0.06 \quad [\mathrm{MeV}],$$

and then the ground-state doublet spacing was estimated to be 140 to 260 keV. We expect to detect the spin-flip M1 transition ($2^- \rightarrow 1^-$) directly with Hyperball.

Production

The non-spin-flip 2^- state of the ground-state doublet, which can be populated by the (K^-, π^-) reaction, is expected to be above the spin-flip 1^- state. Therefore the spin-flip M1 γ ray from 2^- to 1^- is expected to be observed. Unfortunately, no other particle bound state is expected to be produced by the (K^-, π^-) reaction. Figure 1.8 shows the expected level scheme and baryonic decays of $^{10}_{\Lambda}$B by the ^{10}B (K^-, π^-) reaction.

Hyperfragment farm

It was suggested that the ^{10}B(K^-, π^-) reaction is suitable for the γ-ray spectroscopy of hyperfragments [29]. The ground state of $^{10}_{\Lambda}$B is bounded by 2 MeV below the proton emission threshold, and there are many particle emission channels decaying to hyperfragments from the highly excited region. Here, we focus on the decay processes of $^{10}_{\Lambda}$B $\rightarrow {}^{9}_{\Lambda}Be+p$ and $^{10}_{\Lambda}\mathrm{B} \rightarrow {}^{7}_{\Lambda}Li+$ ^{3}He as described in Fig. 1.8. Figure 1.8 shows the expected levels and baryonic decay scheme of $^{10}_{\Lambda}$B produced by the ^{10}B(K^-, π^-) reaction. In this Figure, only two decay processes of $^{10}_{\Lambda}\mathrm{B} \rightarrow {}^{9}_{\Lambda}Be+p$ and $^{10}_{\Lambda}\mathrm{B} \rightarrow {}^{7}_{\Lambda}Li+$ ^{3}He are drawn. However, many decay channels are energetically allowed for highly excited states. Some of the hyperfragments are expected to emit γ rays which have not been observed and identified yet. One of the merits of γ-ray spectroscopy via baryonic decays to hyperfragments is possible large population probabilities of hypernuclear states different from those produced by direct reactions.

For example, the $^{7}_{\Lambda}\mathrm{Li}(\frac{7}{2}^+)$ state which is one of the spin-flip states of $^{7}_{\Lambda}$Li can not be produced by the (π^+, K^+) reaction or the (K^-, π^-) reaction at 0.9 GeV/c, but may be produced as hyperfragments from highly excited states of $^{10}_{\Lambda}$B. Figure. 1.9 shows the level scheme of $^{7}_{\Lambda}$Li. If we can measure the level energy of $\frac{7}{2}^+$, the energy between the spin-weighted energies of the ground-state doublet and the upper doublet can be determined. Then, S_N can be determined precisely.

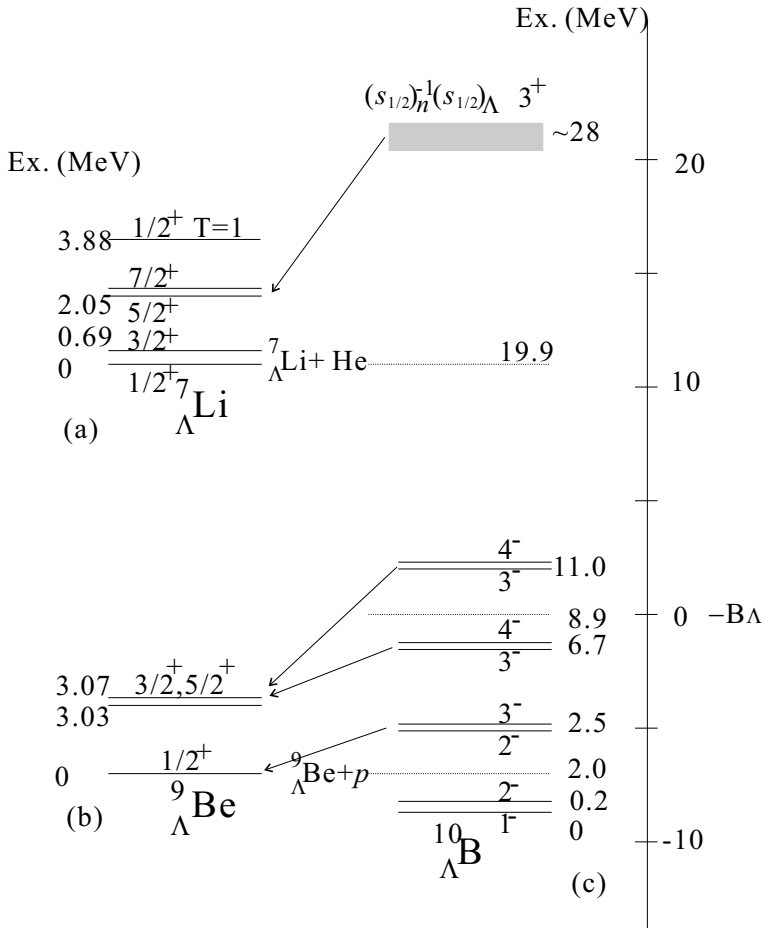

Figure 1.8: *Expected level scheme and baryonic decay of* $^{10}_{\Lambda}B$ *by the* ^{10}B (K^-, π^-) *reaction. (a): experimentally determined [9, 15], (b): experimentally determined [12], and (c): calculated by Millener [8].*

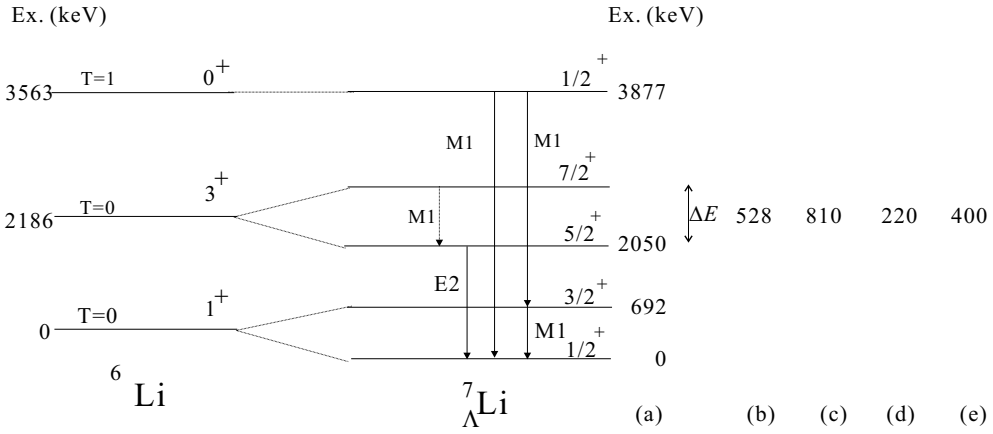

Figure 1.9: *Experimentally determined and expected level scheme of* $^7_\Lambda Li$. *(a) Experiment with Hyperball [9], (b) calculated by Millener et al. [8], (c) calculated by Fetisov et al. [30], (d) calculated by Hiyama et al.[31] and (e) calculated by Motoba et al. [32]*

Chapter 2

Experiment

2.1 Overview

The γ-ray spectroscopy experiment of p-shell hypernuclei with Hyperball, BNL-E930('01), was performed using the BNL-AGS D6 line. We used the (K^-, π^-) reaction employing a 0.93 GeV/c kaon beam. Incident kaons and outgoing pions were identified and momentum analyzed by the beamline spectrometers. The γ rays were detected with Hyperball which was installed around the target in coincidence with the (K^-, π^-) reaction .

2.2 BNL-AGS and D6 line

The Alternating Gradient Synchrotron at Brookhaven National Laboratory (BNL-AGS) accelerates protons and heavy ions up to 30 GeV/c per unit charge. In our experiment, we set the primary proton momentum of 21 GeV/c and the repetition rate of 4.61 s cycle to maximize the kaon flux because of a power supply problem. The accelerated protons of 30 $\times 10^{12}$ per cycle were distributed to the secondary beam lines. In every 20×10^{12} of protons hit the production target of 9 cm-thick platinum located upstream of the D6 line, and produced K^-'s of 2 $\times 10^5$ per cycle were delivered to the experimental area. The D6 line was built in 1990 for the purpose of investigating double strangeness nuclear system such as H dibaryon and $\Lambda\Lambda$ hypernuclei. This beam line has two-stage electrostatic separators and delivers high intensity and high purity kaon beams. Details of the beam line are described in Ref. [34]. The specifications of the D6 line are summarized in Table 2.1 and the experimental condition of the beam line are summarized in Table 2.2.

The quantity, "cross section $\times$ beam intensity", is connected to the yield. The higher momentum provides more beam intensity, and the cross section is maximal at $0.7 - 0.9$ GeV/c. The highest momentum of 1.8 GeV/c provides the largest yield. However the large momentum transfer ($\sim$ 300 MeV/c) causes serious Doppler shift of γ-ray energy. Therefore, we set a beam momentum at the upstream of all the detectors to be 0.93 GeV/c; taking into account the energy loss in the target and detector medium ($20 \sim 40$ MeV/c). The momentum transfer at 0.9 GeV/c is about 150 MeV/c, of which the Doppler-shifted γ-ray energy is expected to be corrected.

Table 2.1: *Specification of D6-line*

Maximum momentun	2.0 GeV/c
Production target	Pt
Target thickness	9 cm
Production angle	5 deg.
Beam line length	31.6 m
Momentum acceptance	6 %

Table 2.2: *Experimental condition*

Primary proton momentum	21 GeV/c
Repetition rate	4.61s /spill
Flat top time	1.45 s
proton intensity	20 $\times 10^{12}$/spill (Max.)
K^- momentum	0.93 GeV/c
K^- rate	200 k/spill (Max.)
K^-/π^- ratio	3/1

2.3 Spectrometer system

The beam spectrometer consisted of a dipole magnet (D3), quadrupole magnets, sextupole magnet, octupole magnet, scintillator hodoscopes (MT, MP and IT), drift chambers (ID1, ID2 and ID3) and aerogel Čerenkov counters (IC1 and IC2) as shown in Fig. 2.1. The outgoing particle spectrometer consisted of a dipole magnet (48D48), scintillator hodoscopes (FV and BT) an aerogel Čerenkov counter (FC), and drift chambers (FD1, FD2, FD3, BD1 and BD2). All the detectors for beam and outgoing particles are shown in Fig. 2.1, Fig. 2.2 and Fig. 2.3. In addition, to avoid multiple scattering, helium filled bags were installed between FD2 and FD3 and between FD3 and BD1.

2.3.1 Scintillator hodoscopes

We used five types of scintillator hodoscopes. All the hodoscopes are summarized in Table 2.3. MT, IT and BT were the timing counters to measure the time-of-flight (TOF), and all these TOF counters were read out by PMT's at both ends.

Table 2.3: *Characteristics of the scintillator hodoscopes*

hodoscope	orientation	deimention of one element $x \times y \times z$(cm^3)	segmentation	read out
MT	vertical	$1.5 \times 3.7 \times 0.6$	9	both ends
MP	vertical	$1.5 \times 0.7 \times 0.3$	72	single end
IT	vertical	$10.0 \times 4.0 \times 0.635$	1	both ends
FV	horizontal	$10.0 \times 6.0 \times 1.0$	1	single end
BT	horizontal	$200.0 \times 8.5 \times 5.0$	40	both ends

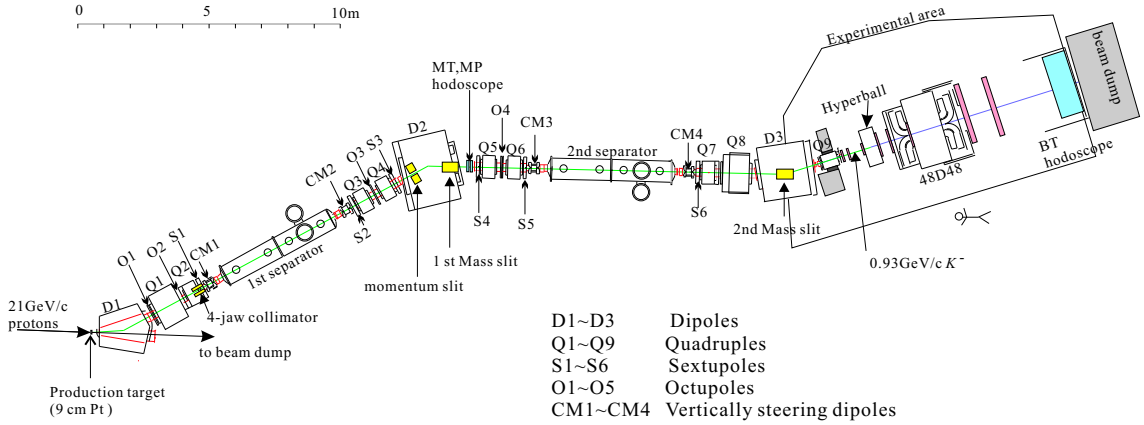

Figure 2.1: *Schematic layout of D6 line and experimental area (top view)[35]*

MT, MP

MP was a horizontal position detector located at the momentum dispersive point to determine the beam momentum. It was segmented horizontally and arranged in two lines. MT was used to measure the TOF timing to discriminate between K^- and π^-. MT was also segmented horizontally but it was arranged in one line. So, there was a small gap between two adjacent elements, which caused a lower efficiency of MT. The efficiency of the MT detector was 92 % and the efficiency of the MP detector was 97 %. The time resolution of MP was 1.3 ns (σ) for the worst one and 0.8 ns (σ) for a typical one, while the resolution of MT was 0.4 ns (σ). The flight length between MP and IT was 15 m. For the 0.93 GeV/c momentum, the TOF difference between kaon and pion is about 6 ns and the timing resolution of MP is enough to discriminate them. For that reason, MP was used as not only a position detector but also as a TOF counter in our analysis to increase the analysis efficiency.

IT

IT was used to measure the TOF between MP and itself and between BT and itself. IT provided a reference timing for all the detectors.

FV

FV was located at 0 degree between FD1 and FD2 and used to reject unscattered beam particles and very-forward scattered particles. A large number of kaons passed the target without reaction, in which event FC sometimes radiated Čerenkov light by δ-rays. The ratio of such events to the true triggered events was not small at all. On the other hand, when kaon and pion had a small reaction angle less than 2 degree, the reaction vertex point resolution was too bad to select target-reaction events. Thus we used FV in the trigger.

BT

BT was used to measure the TOF of scattered particles. A typical flight length was 7.9 m from the target. BT was vertically segmented into 40 elements and located downstream of all the detectors. BT was inclined by 15 degree, in which the flight lengths for particles having different scattered angles are kept to be almost the same.

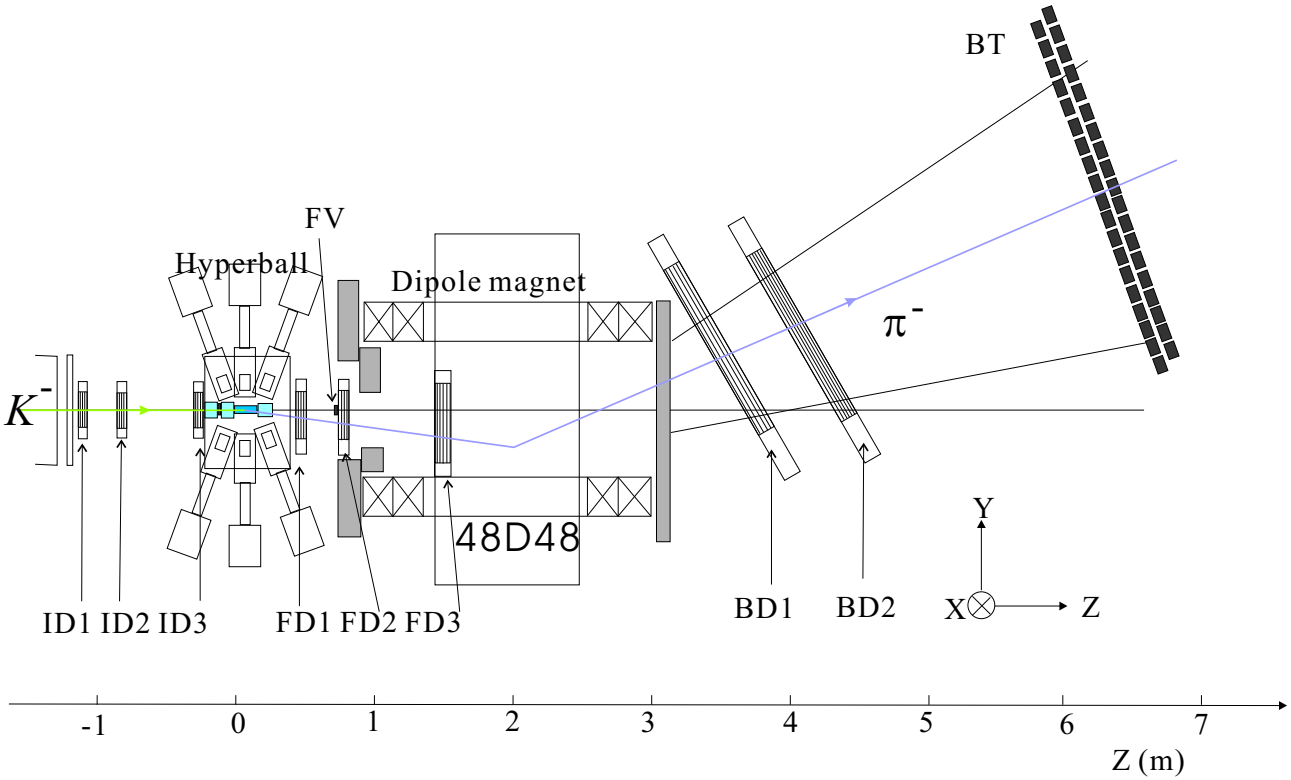

Figure 2.2: *Schematic layout of the experimental area (side view). The detectors around the target are not shown in this figure.*

BT was also used as a position detector in off-line analysis. It was not used in the tracking analysis but used to select multi-track events. The details of BT was described in Ref. [36].

2.3.2 Čerenkov counters

Aerogel Čerenkov counters (IC1, IC2 and FC) were set up to discriminate between kaon and pion for the purpose of identifying incident and scattered particles. IC2 and FC were located as close to the target as possible to minimize those events in which beam kaons decay in flight between IC2 and FC, because such events were misinterpreted as (K^-, π^-) reaction events. All the aerogel we used had a refractive index of 1.03, which corresponds to the threshold momenta of 0.56 GeV/c for kaons and 1.97 GeV/c for pions. We used all the Čerenkov counters for the trigger. The configuration of the Čerenkov counters is shown in Fig. 2.3. The PMTs we used for IC2 and FC were so-called fine-mesh type PMT (HAMAMATSU H5543). This type of PMT is fit to use in the magnetic field. Since IC2 and FC were installed close to the 48D48 magnet, they were affected by the fringing field. Characteristics of all the Čerenkov counters are summarize in Table 2.4

IC1, IC2

IC1 and IC2 were the detectors to identify the incident kaon in the trigger level. IC1 and IC2 were located downstream of the last beam chamber ID3, and IT was put between IC1 and IC2. The particle identification with the two-stage of aerogel Čerenkov counters provided an almost pure kaon trigger, but it caused suppression for kaon of 4 %.

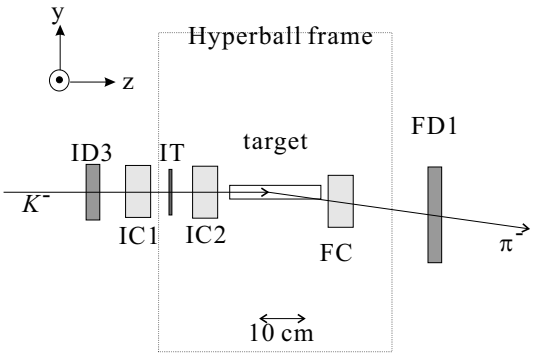

Figure 2.3: *Schematic layout around the target (side view), the germanium and the BGO counters of Hyperball are not shown in this figure.*

Table 2.4: *Characteristics of the Aerogel Čerenkov counters.*

Cherekcov counter	index	dimention of effective area $x \times y \times z(\mathrm{cm}^3)$	mean number of photoelectrons for 0.9 GeV/c π (counts)
IC1	1.03	$11.4 \times 3.5 \times 5.5$	3.87
IC2	1.03	$11.4 \times 11.4 \times 5.5$	3.31
FC	1.03	$11.4 \times 11.4 \times 5.5$	3.31

FC

FC was the detector to identify outgoing pions in the trigger level. FC was located just downstream of the target. The detection efficiency for pion was 98 %. The misidentification for kaon as pion was 1 %. Such misidentified kaons in outgoing particles were rejected with FV.

2.3.3 Drift chambers

The trajectories of incident and outgoing particles were measured with drift chambers. The incident particle trajectory which was measured with ID1, ID2 and ID3 and the outgoing particle trajectory which was measured with FD1 and FD2 were used to reconstruct a reaction vertex point. These chambers were developed to operate in the high-counting rate of 10^7 Hz with a small drift length of 0.1 inch and with a multi-hit TDC. The design parameters of all the chambers are summarized in Table 2.5. The gas mixture of 77 % argon, 20 % isobutane and 3 % methylal was used for all the drift chambers. All the TDC's for the chambers were of the multi-hit type, and we took leading and trading edges of the pulse to discriminate signals from noise pulses.

ID1, ID2 and ID3

ID1, ID2 and ID3 were identical chambers. Each chamber consisted of three pairs of planes. ID's were designed with the wire orientation of x(0°)-u(120°)-v(60°) to give a better horizontal (x) resolution.

Table 2.5: *Design parameters of the drift chambers*

	plane	orientation (wire)	spacing (mm)	channel	active area X×Y (cm^2)	resolution (σ, mm)
ID1	u-u'	120°	5.08	24×2	12.2 ×10.6	0.2
	v-v'	60°	5.08	24×2		
	x-x'	0°	5.08	24×2		
ID2	u-u'	120°	5.08	24×2	12.2 ×10.6	0.2
	v-v'	60°	5.08	24×2		
	x-x'	0°	5.08	24×2		
ID3	u-u'	120°	5.08	24×2	12.2 ×10.6	0.2
	v-v'	60°	5.08	24×2		
	x-x'	0°	5.08	24×2		
FD1	u-u'	210°	5.08	48×2	21.2 ×24.4	0.2
	v-v'	150°	5.08	48×2		
	x-x'	90°	5.08	48×2		
FD2	u-u'	210°	5.08	48×2	21.2 ×24.4	0.2
	v-v'	150°	5.08	48×2		
	x-x'	90°	5.08	48×2		
FD3	u	150°	12.7	64	45.7 × 81.3	0.3
	y	90°	12.7	64		
	y'	90°	12.7	64		
	v	30°	12.7	64		
BD1	y	90°	20.0	112	114.0 × 214.0	0.4
	u	120°	20.0	128		
	v	60°	20.0	128		
	y'	90°	20.0	112		
BD1	y	90°	20.0	112	114.0 × 214.0	0.4
	u	120°	20.0	128		
	v	60°	20.0	128		
	y'	90°	20.0	112		
	v'	60°	20.0	128		

FD1 and FD2

FD1 and FD2 were identical chambers. They had almost the same parameters as ID1-3 except for the size of effective area and the wire orientation. FD1 and FD2 were designed with the wire orientation of y(90°)-u(210°)-v(150°) to give a better vertical (y) resolution. The center of FD1 and FD2 were 5.8 cm vertically lower than the beam line center to maximize the acceptance for the scattered particle with a scattering angle of about 8 degree which corresponds to the $\Delta L = 1$ reaction.

FD3

FD3 was installed in the 48D48 magnet gap. FD3 helped to determine a better momentum.

BD1 and BD2

BD1 and BD2 chambers were installed downstream of the 48D48 magnet to measure the trajectory of outgoing particles after they were bent. BD1 and BD2 were inclined by 30 degree as shown in Fig. 2.2.

2.3.4 48D48

A dipole magnet with a large acceptance of about 60 msr was installed downstream of the target. The pole size was 48 inch wide and 48 inch deep, and the gap size was 80 cm. We set the central field at 0.8 Tesla during the experiment, which was optimized to the outgoing pion momentum of about 0.8 GeV/c. Since the direction of the magnetic filed was horizontal, the outgoing particles were bent vertically. The acceptance was limited by FD2. Since the field map of 48D48 was measured only for 1.4 T, the field map for 0.8 T we used was calculated by the TOSCA code [37].

2.4 Hyperball

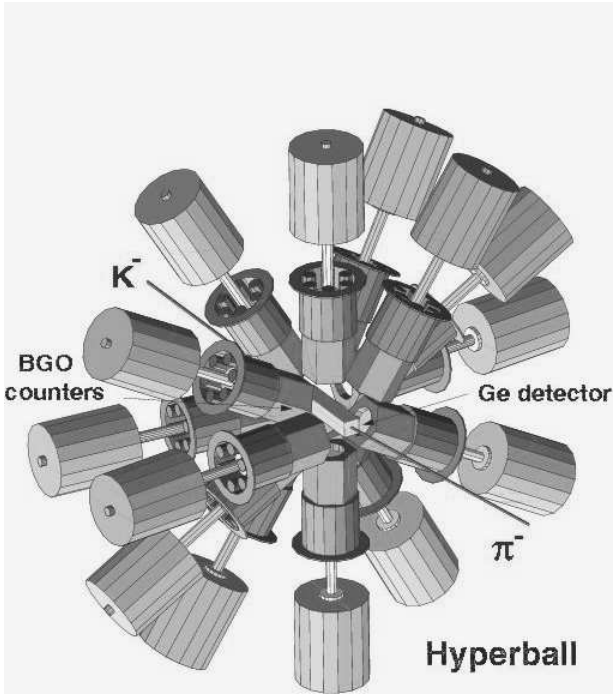

Figure 2.4: *Schematic view of the Hyperball*

Hyperball was built to be dedicated to the γ-ray spectroscopy of hypernuclei. Hyperball made its debut in spring of 1998 at the KEK-PS K6 line. Hyperball consisted of fourteen germanium detectors, each of which was surrounded by six BGO counters. The read-out electronics for the germanium detectors were suited to high counting rates. Figure 2.4 shows a schematic view of Hyperball. The end caps of all the germanium detectors facing the beam were located at a distance of 10 cm from the beam axis. This distance was optimized, considering the accuracy of the γ-ray emission direction which is necessary for Doppler shift correction, and maximizing the solid angle from the target. Figure 2.5 shows a typical configuration of the germanium and the BGO crystals.

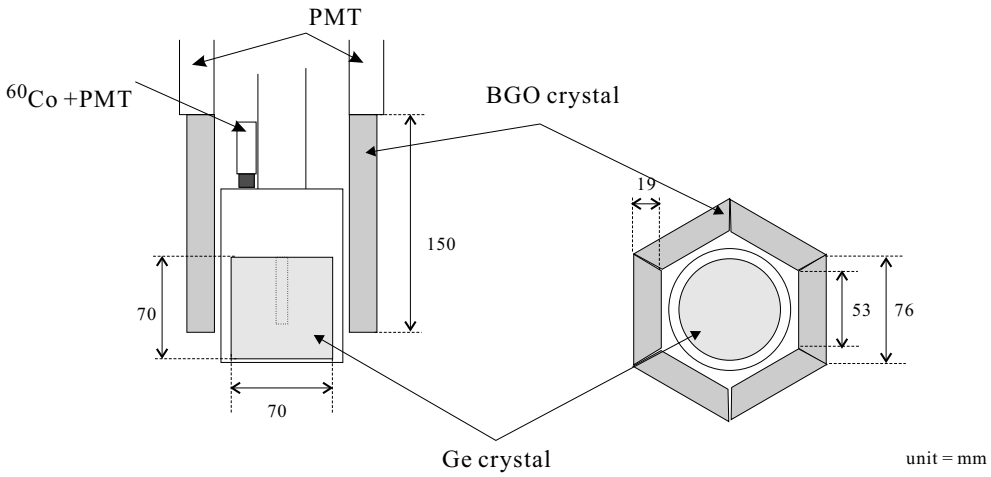

Figure 2.5: *A typical configuration and size of germanium crystal and BGO crystals*

2.4.1 Germanium detectors

Fourteen coaxial-type germanium detectors were used in Hyperball. Ten germanium detectors were the products of ORTEC company and the other four were the products of Eurisys Measures company. Each germanium detector had a high-purity, n-type crystal with a volume of 250 cc (7 cm $\times$ 7 cm ϕ). Their relative efficiencies[1] were 60 %. A typical energy resolution of the germanium detectors was 3.5 keV (FWHM) and a typical time resolution was 4 ns (FWHM) for ^{60}Co 1.33 MeV γ ray in our setup in the beam-off condition. The entrance windows of the germanium detector were made of 0.5 mm-thick beryllium for the ORTEC products and 2 mm-thick aluminum for the Eurisys products. We put a plastic plate of 2 mm thickness to protect the thin beryllium window for each germanium detectorof ORTEC.

Reset-type preamplifier

All the germanium detectors were equipped with transistor-reset type preamplifiers. They solved the difficulty of operation under the high energy-deposit environment. Figure 2.6 shows a conceptual illustration of reset-type preamplifier outputs. A feature of the reset-type preamplifier is the sawlike output signal (top of Fig.2.6). The output of the preamplifier is a step function, where one-step corresponds to one signal output. The output level is kept constant until a next input pulse comes or when the level reached the reset threshold level, when the preamplifier resets to the baseline by discharging the feedback capacitor. The dead time due to the reset is as short as 15 μs. The threshold level corresponds to 150 MeV input signal in our detectors, which is larger than the energy by a minimum ionizing particle penetrating the detector. If we use commonly used preamplifier, resister feed-back type, under the high energy-deposit rate, they stop working for a while when a high energy deposit occurs by penetration of a charged particle. It causes a serious dead time of detectors.

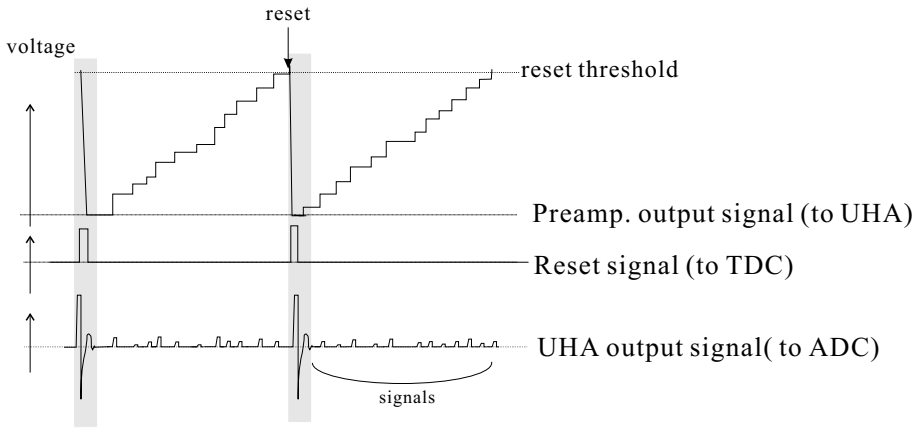

Figure 2.6: *Conceptual illustration of the reset-type preamplifier and response of signals. In the shadowed region, the base-line shifts in the UHA output. So, a hit within this region, typically 15 μs, is rejected in the off-line analysis.*

[1] The "relative efficiency" is defined as the efficiency at 1.33 MeV relative to the efficiency of a 3" $\phi\times$ 3" NaI scintillator at a 25 cm distance from a ^{60}Co source

2.4.2 Readout electronics

Figure 2.7 shows the block diagram of the electronics for the germanium detectors. Each germanium detector had three types of output signals as shown in the figure. The output of the preamplifier was divided into two signals, and one was sent to the main amplifier, ORTEC 973U (Ultra-High-rate Amp., UHA) and the other was sent to the timing filter amplifier, ORTEC 579 Fast-Filter Amp. (TFA) with fast rise time of 5 ns. The amplifier we used (UHA) was composed of a fast shaping amplifier and a gated integrator. It had a small dead time of 6 μs due to signal pileup. The gated integrator (GI) output signals of UHA were send to the ADC of the main DAQ system and of the monitoring system. The ADC in the main DAQ (ORTEC AD413a) has 8 k channels and can be readout via FERA bus. The other output signal of UHA was CRM (count rate meter) output and it was a logic signal synchronized with the GI output. The output of TFA was send to a constant fraction discriminator (CFD) and then to a multi-hit TDC (LeCroy 3377) which can be read out via FERA bus. The combination of TFA and CFD was fit to timing measurement. We used TDC data of TFA in the off-line analysis, and used CRM output in the trigger.

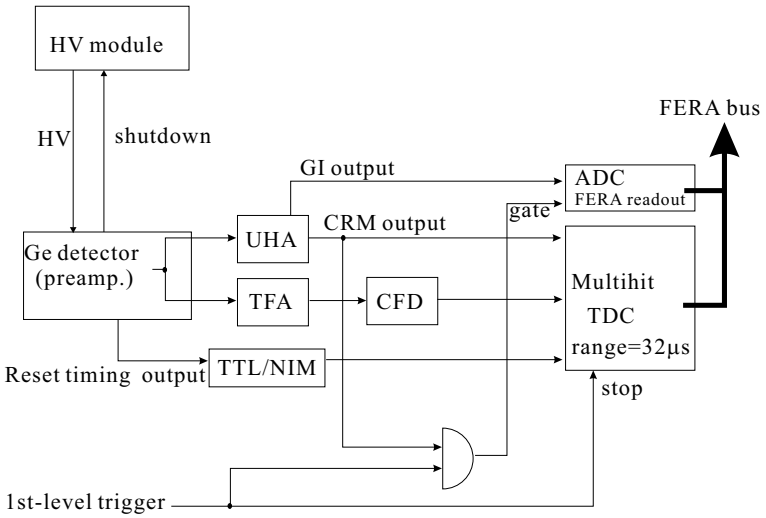

Figure 2.7: *Block diagram for the germanium detector read-out system for the main DAQ.*

2.4.3 BGO counters

We used bismuth germanate ($Bi_4Ge_3O_{12}$, BGO) scintillation counters. They were used to reject such events as Compton scattering γ rays escaping from the corresponding germanium detector and high-energy γ rays from π^0 decay. BGO was chosen for the benefit of its large effective atomic number of 75. However, the scintillation decay constant is as slow as 300 ns, and the relative light output is 1/10 of NaI crystal. So the BGO emits the scintillation photons sporadically within a few μs. We set the discriminator threshold at 25 mV for TDC input signals so as to discriminate even single-photon signals.

A typical timing resolution of the BGO counters was 4 ns for 1 MeV γ ray and a typical energy resolution was 27 % (FWHM) for 662 keV γ ray.

2.4.4 In-beam and off-beam performance

The relative efficiencies of the germanium detectors between in-beam and off-beam periods were measured by a CAMAC-based DAQ system (monitoring system). This system was independent of the main DAQ system. A 1 kBq ^{60}Co source was placed near the each germanium crystal. ^{60}Co sources were contained in plastic scintillators which were connected to PMTs. The ADC data for germanium detectors were taken when the scintillator detected a β-ray and a germanium detector detected a γ-ray in coincidence. The data were taken both in the in-beam and the off-beam periods. We could estimate the in-beam/off-beam relative efficiency with 1.33 MeV and 1.17 MeV photo-peak counts. We obtained the relative efficiency for all the germanium detectors of 90 $\pm$ 5 %.

2.5 Targets

We used a water target for ^{16}O and an enriched ^{10}B target. They were placed at the center of Hyperball. Water was filled in a plastic container. The capacity was 80 $\times$ 30 $\times$ 200 mm^3, corresponding to 20 g/cm^2 thickness for beam. The two faces of the container crossing the beam were made of mylar and all the other faces were made of plastic of 2 mm thickness.

The ^{10}B target was composed of small plates of hot-pressed ^{10}B powder with 1.42 g/cm^3 as shown in Fig. 2.8. The total thickness corresponded to 14.2 g/cm^2.

Figure 2.9 shows the beam profile at the target. A dotted line indicates the cross section of the water target and a solid line indicates the cross section of the ^{10}B target.

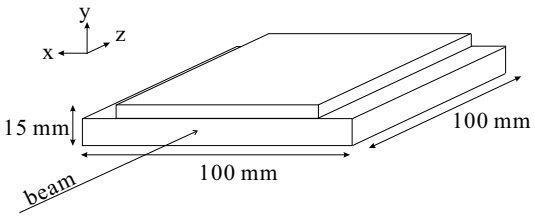

Figure 2.8: *Schematic view of the ^{10}B target*

2.6 Trigger and data acquisition system

2.6.1 Data acquisition system

All the ADC and the TDC data except for the ADC of the germanium detectors were collected via four FASTBUS crates to the Universal MEMory modules (UMEM [38]) in a VME crate. The ADC data for the germanium detectors were collected via FERA bus to another UMEM in the VME crate. The data were read out from the UMEM's to a personal computer (PC) via a VME-PCI interface once per synchrotron cycle during the off-spill period and were written on a DVD-RAM. Figure 2.10 shows a diagram of the data acquisition system and the data transfer. The DAQ dead time was 16 % for the water target run and 12 % for the ^{10}B target run with the 2nd level trigger described later.

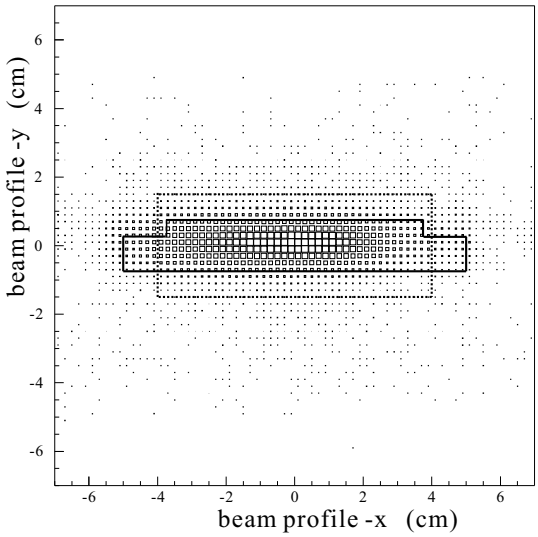

Figure 2.9: *Beam profile at the target. A dotted line indicates the cross section of the water target and a solid line indicates the cross section of the ^{10}B target.*

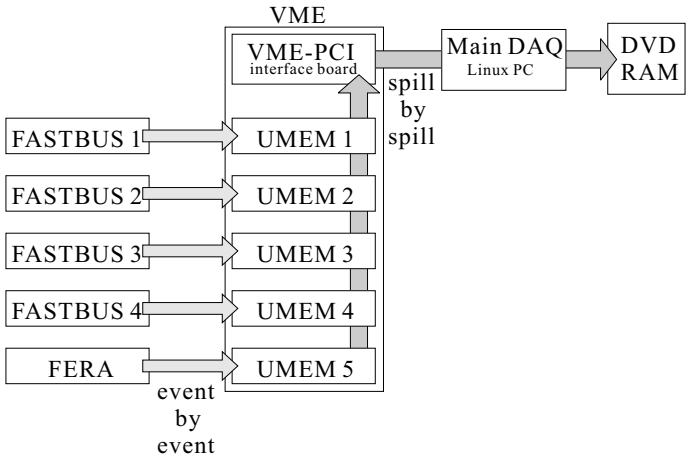

Figure 2.10: *Schematic diagram of the data acquisition system and the data transfer*

2.6.2 First level trigger

For the event trigger, incident kaons were selected as

$$\mathrm{Kin} = \overline{\mathrm{IC1}} \times \mathrm{IT} \times \overline{\mathrm{IC2}}.$$

Pion contamination in the beam was almost rejected by the two stages of IC veto. The outgoing pions were selected as

$$\mathrm{PIout} = \mathrm{FC} \times \Sigma\mathrm{BT}.$$

FC was used to reject scattered kaons. Thus, the main trigger for the (K^-, π^-) reaction, KPI, was defined by

$$\mathrm{KPI} = \mathrm{Kin} \times \mathrm{PIout} \times \overline{\mathrm{FV}}.$$

FV was used to reject unscattered beam and very forward-scattering particles.

Other triggers for calibration, (π^-, π^-), (K^-, K^-) and (K^-, π^-) without FV veto were defined as

$$\text{PIPI} = \text{IC1} \times \text{IT} \times \text{IC2} \times \text{PIout},$$

$$\text{KK} = \text{Kin} \times \overline{\text{FC}} \times \Sigma\text{BT},$$

$$\text{KPI}_{non-bias} = \text{Kin} \times \text{PIout}.$$

Some of these triggers data were taken after thinning out by a corresponding factor (prescale factors) so as not to increase the DAQ dead time. The rates of these triggers and the prescale factors are listed in Table 2.6.

Table 2.6: *Trigger rate summary*

trigger definition	IT	Kin	PIin	KPI	$\text{KPI}_{non-bias}$
counts/spill ($\times 10^3$)	280	200	70	1.1	2.4
prescale factor	10^5	8×10^4	4×10^4	1	80

2.6.3 Second-level trigger

The second-level trigger was used to reject those events in which there were no ADC data or only overflow data for the germanium detectors. It was important to reject such no-germanium-hit events in order to minimize the DAQ dead time. Figure 2.11 shows the second-level trigger diagram. When the second-level trigger was not accepted, a signal was delivered to all the FASTBUS crates to stop the process and flush the data. Two types of FASTBUS clear signal were defined as follows.

- No data event clear

  This clear signal was generated when there was no germanium detector hits within 1 μs time gate in coincidence with the first-level trigger.

- Overflow event clear

  When the ADC's for the germanium detectors had only overflow data, the FERA ADC module output the read-out-end signal within 7 μs, which was much earlier than the case of the normal ADC data. Since the FASTBUS ADC/TDC modules took more than 300 μs of conversion time, we could save most of this time by sending the FERA ADC overflow signal as the FASTBUS clear signal.

The trigger rate was reduced to 28 % with the second-level trigger.

2.6.4 Germanium detector self-trigger data

We also took germanium detector self-trigger data for the calibration of the germanium detectors. The germanium detector self-trigger data was taken in the in-beam and the off-beam periods.

- in-beam self trigger

  The conversion and read-out process for the FERA modules ended 400 μs earlier than that for FASTBUS. After the FERA read-out ended, the self-trigger data were taken for 360 μs before the FASTBUS read-out ended. Figure 2.12 shows the conceptual illustration of the germanium self trigger for the in-beam period.

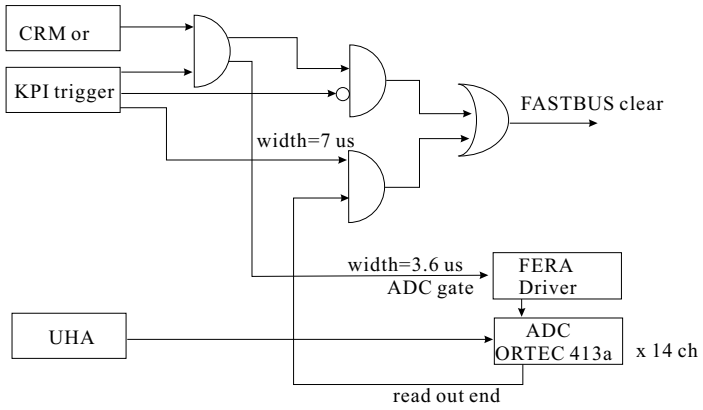

Figure 2.11: *Schematic diagram of the 2nd level trigger.*

- off-beam self trigger

  The germanium self trigger data were taken for 0.7 s before the data transportation from UMEM's to PC in the off-beam period in every cycle.

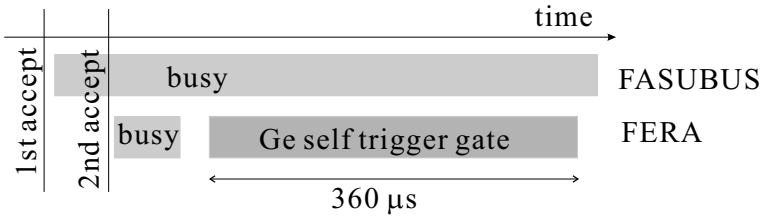

Figure 2.12: *Conceptual illustration of the germanium self trigger for the in-beam period.*

2.7 Data summary

The experiment was performed in the fall of 2001. The total beam time we used was about 60 days but the beam was delivered only for 560 hours. We irradiated 4.0 $\times 10^{10}$ kaons on the water target and 0.5 $\times 10^{10}$ kaons on the ^{10}B target for 48 hours in 5 days.

Chapter 3

Analysis - The (K^-, π^-) Reaction

The analysis procedure consists of two parts. I will describe in this chapter the analysis of the (K^-, π^-) reaction data and the event selection. In the next chapter I will describe the analysis of the γ ray data.

3.1 Procedure of analysis

The off-line analysis procedure for the (K^-, π^-) reaction with for the magnetic spectrometers data is as follows:

- K and π selection with the TOF counters,
- local tracking of the chambers,
- momentum reconstruction for incident K^-,
- momentum reconstruction for outgoing π^-,
- vertex and reaction angle reconstruction,
- calculation of missing mass,
- calculation of recoil velocity and direction of the recoiling hypernuclei.

The off-line analysis procedure for γ rays with the Hyperball data is as follows:

- selection of germanium detector hits with good timing,
- conversion of germanium detector ADC into γ-ray energy,
- veto with the BGO counter hit,
- rejection of the germanium detector pileup and pre-reset hits,
- reconstruction of γ-ray direction,
- Doppler shift correction of γ-ray energy.

The procedure of the analysis is summarized in Fig. 3.1

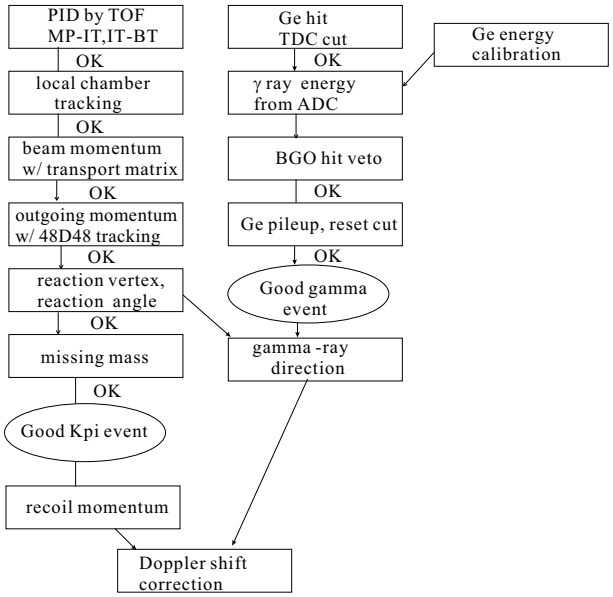

Figure 3.1: *Conceptual illustration of the analysis procedure*

3.2 K^- selection

The two-stage aerogel Čerenkov counters were working well and the misidentification of pion in kaon trigger was negligible. Figure 3.2 shows the time-of-flight distribution between MP and IT. The time-zero was adjusted to kaon timing. (a) is for the KPI trigger event with a single hit in MP, and (b) is for the PIPI trigger event with a single hit in MP. A particle determined as "Kin" is regarded as a real kaon. Since MP and MT were located upstream of the second mass separator and the second mass slit, their counting rates were so large. In addition, since the beam seemed to have a micro-bunch structure, the MP counters had a high multiplicity, and roughly a half of trigger events had multi-hits in MP within 20 ns gate. Figure 3.2 (c) is for the KPI trigger events with a high multiplicity in MP (≥ 3). For these high multiplicity events, beam structure appeared close to the kaon timing. For that reason, among multiple MP hits we select the MP hit with the closest timing to the kaon timing and we accepted events with the MP timing within the 8 ns gate as shown in Fig. 3.2 (a) and (c).

3.3 π^- selection

Figure 3.3 shows the time-of-flight between IT and BT. The π^-/K^- separation power was good enough without momentum reconstruction of the outgoing particles. We selected the outgoing π^- for 27 ns $< TOF_{IT-BT} <$ 31.5 ns as shown in the figure.

3.4 Incident kaon momentum reconstruction

The incident particle momentum was calculated with the x-position at MP obtained from the hit segment number in MP, the straight track between the Q9 magnet and the target reconstructed with the ID chambers, and the transport matrix. All events with the reconstructed ID track and the MP hit within the true timing were accepted. Figure 3.4 shows the momentum distribution of the incident kaons.

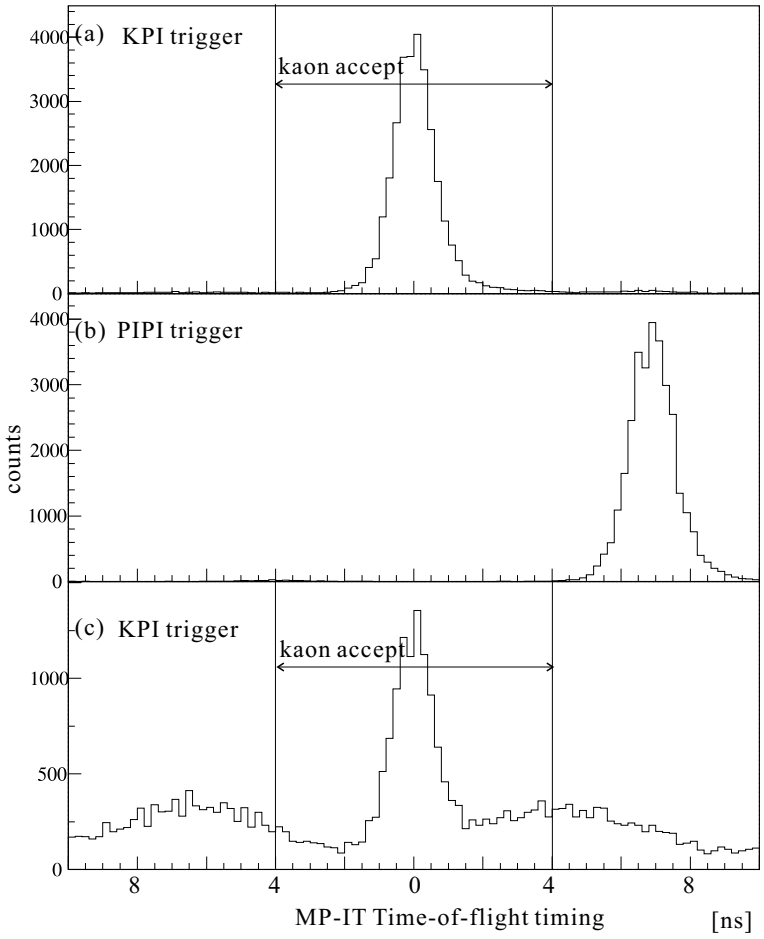

Figure 3.2: *Time-of-flight between MP and IT. (a) KPI trigger events with a single hit in MP, (b) PIPI trigger events with a single hit in MP and (c) KPI trigger events with a multi-hit ($\geq$ 3) in MP. The trigger definition is described in Sect. 2.6.2. The solid lines show the accepted region for kaons.*

3.5 Outgoing pion momentum reconstruction

First, the momentum of outgoing particle was roughly calculated with the local track reconstructed by FD1 and FD2, and the local track by BD1 and BD2, and with the transport matrix. Next, the momentum was calculated by Runge-Kutta method using the field map of the 48D48 magnet. The tracking result of the rough calculation was used as the initial value in the iteration, and information of FD3 hit in the magnetic field was provided for more precise tracking.

3.6 Reaction vertex point and reaction angle

The reaction angle and the reaction vertex point were obtained with the local track from ID1, ID2 and ID3 and the local track from FD1 and FD2. The fringing field from the 48D48 magnet around FD2 was not so large to affect the tracking. We obtained the z-vertex resolution of 1.5 cm in σ. Figure 3.5 shows the z-axis-projected reaction vertex distribution in the target region for the reaction angle over 2 degree. Figure 3.5 (a) is for the water target and (b) is for the ^{10}B target. We accepted the reaction angle

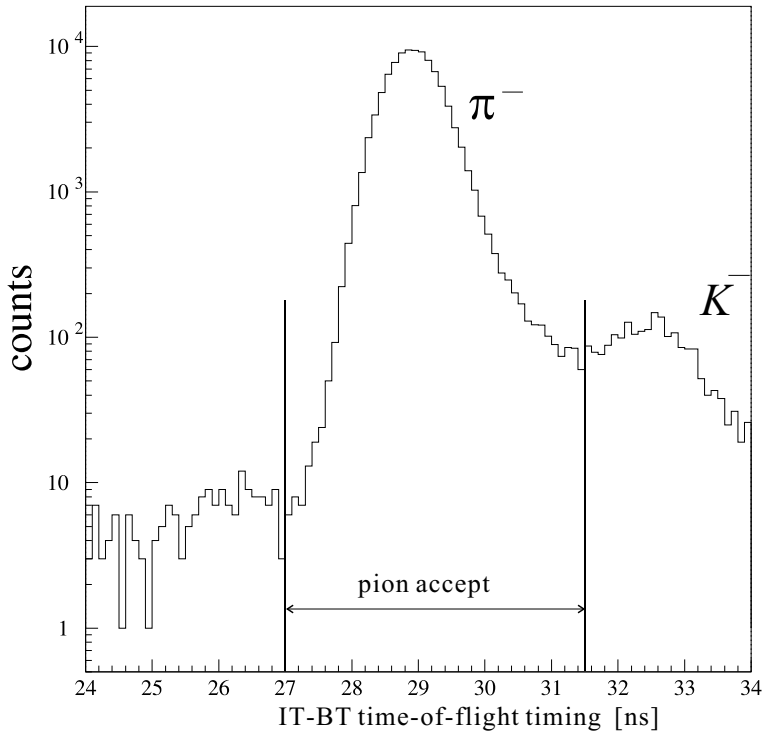

Figure 3.3: *Time-of-flight between IT and BT for the KPI trigger events. Solid lines show the accepted region for* π^-.

over 2 degree, and we accepted the z-vertex of -15 cm $<$ z $<$ 15 cm for the water target and of -8 cm $<$ z $<$ 8 cm for the ^{10}B target.

3.7 Missing mass reconstruction

The mass of the hypernucleus (M_{HY}) was calculated as the missing mass in the (K^-, π^-) reaction as follows,

$$M_{HY} = \sqrt{(E_K + M_{target} - E_\pi)^2 - 2(p_K^2 + p_\pi^2 - p_K p_\pi \cos\theta)} \tag{3.1}$$

where E_K (E_π) and p_K (p_π) are the energy and the momentum of K^- (π^-), M_{target} is the mass of ^{16}O or ^{10}B target nucleus, and θ is the reaction angle in laboratory frame.

3.7.1 Energy-loss correction in the target

In the momentum reconstruction, energy loss effect in the target and the detector medium was not taken into account. The target we used was so thick and the value of energy loss depended on the directions of the incident and the outgoing particles. We corrected the reconstructed momenta with their directions and their vertex point. The energy loss in each target was calculated by the Bethe-Bloch equation. The energy loss per 1 cm at 900 MeV/c in the water target is 2.19 MeV for K^- and 2.05 MeV for π^-, and in the ^{10}B target it is 1.97 MeV for K^- and 1.84 MeV for π^-.

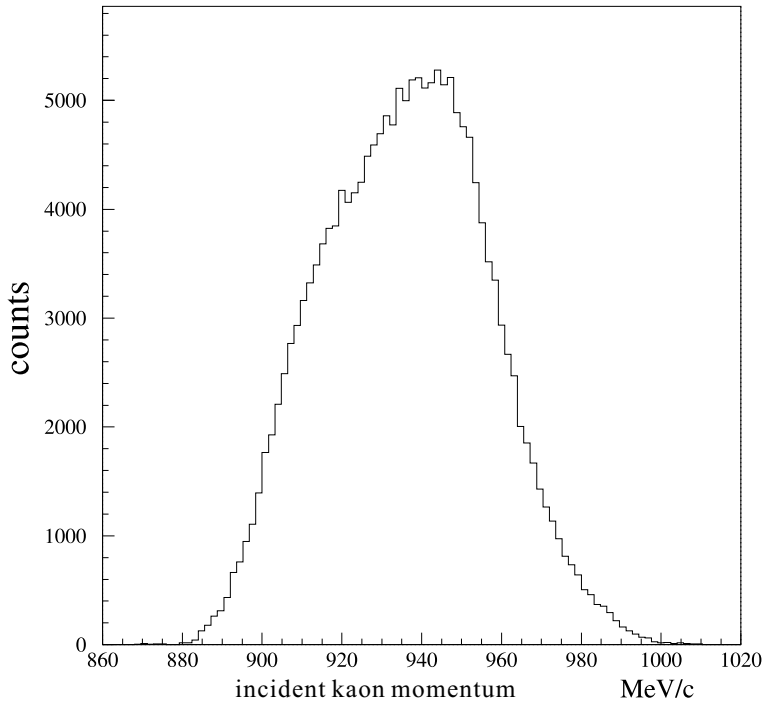

Figure 3.4: *Incident kaon momentum distribution*

3.7.2 Λ binding energy

The Λ binding energy in hypernucleus $B_\Lambda$is defined by

$$-B_\Lambda = M_{HY} - M_\Lambda - M_{core}, \tag{3.2}$$

where M_{core} is the mass of ^{15}O and ^{9}B. The Λ binding energies for $^{16}_{\Lambda}$O and $^{10}_{\Lambda}$B, which were experimentally determined, are summarized in Table 3.1 and 3.2. When we plotted the mass spectrum by selecting the $^{16}_{\Lambda}$O γ ray events, the 1^- state of $^{16}_{\Lambda}$O was enhanced as described later (see Fig. 5.3). We fitted the peak with a Gaussian function and obtained the width of 15 MeV(FWHM). Thus, in the present experiment, the mass resolution was found to be 15 MeV(FWHM). So, we set the mass gate width of 30 MeV to select the bound state region. Even we took into account the energy loss in the target and the detector medium, and the momentum off-set between incident and outgoing momentum, the mass of the 1^- state of $^{16}_{\Lambda}$O was slightly shifted from the values in Table 3.1. We added 5.4 MeV to adjust the mass of the 1^- state to $-B_\Lambda$=$-$7 MeV. When we changed the fitting region, the mean value shifted slightly, and we found that the corrected mass had a systematic error of 0.4 MeV. As summarized in Table 3.1, the mass of the 1^- state is suggested to be in the range of from 6.0 to 7.3 MeV. We added 0.5 MeV to the systematic error and we defined the systematic error of 0.9 MeV for the missing mass. In the present experiment, it does not so matter if the absolute value of the mass is not exactly correct. Figure 3.6 shows the adjusted mass of $^{16}_{\Lambda}$O in $-B_\Lambda$ scale plotted for those events with γ-rays energy within the range from 6.5 to 6.6 MeV corresponding to the $1^-\rightarrow 0^-$ and $1^-\rightarrow 1^-$ transitions. The solid line indicates the fitting result.

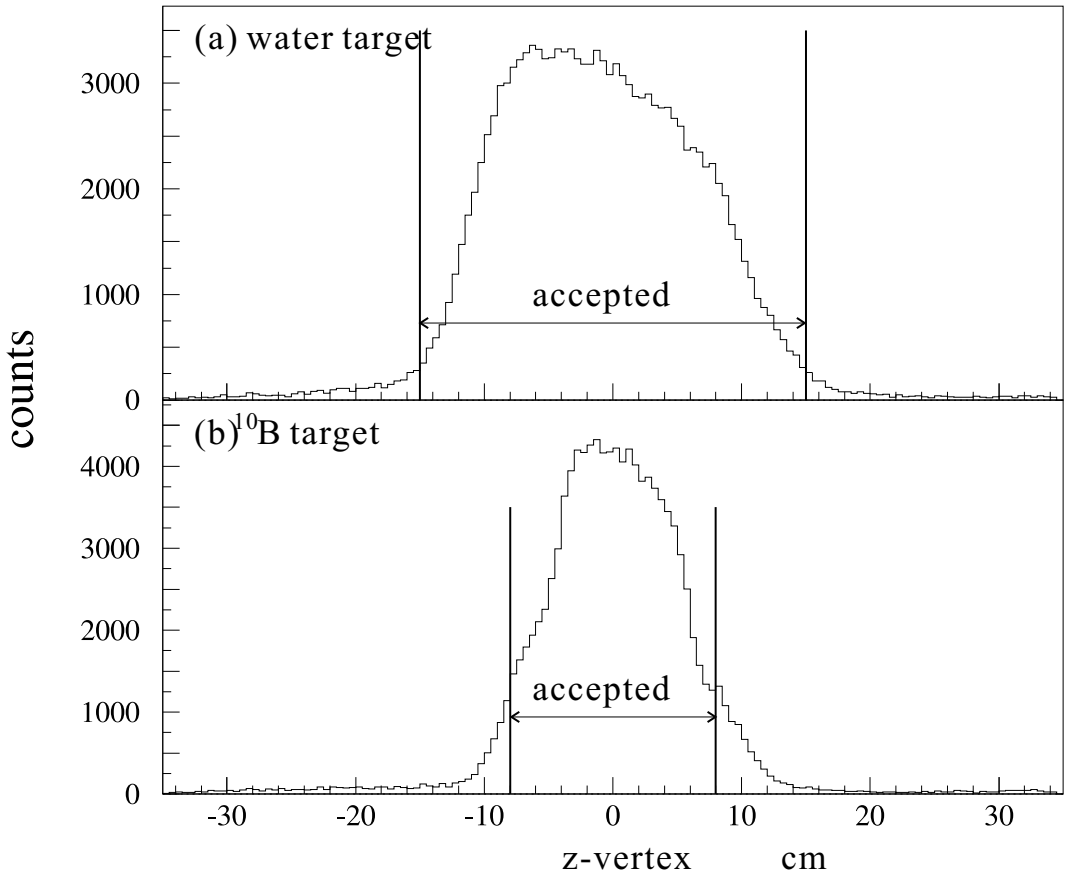

Figure 3.5: *Vertex distribution around the target. z=0 cm is adjusted at the target center. (a) is for the water target and (b) is for the ^{10}B target. Each solid line indicated the accepted region.*

Table 3.1: Λ *binding energy of* $^{16}_{\Lambda}O$ *[MeV]*

Dominant configuration	(π^+, K^+) KEK[19]	(π^+, K^+) BNL[20]	(K^-, π^-) CERN[21]	$(K^-_{stopped}, \pi^-)$ KEK[22]
$(p_{1/2})_n^{-1}(s_{1/2})_\Lambda$, 1^-	12.50 ± 0.1	12.50 ± 0.40	13.21 ± 0.26	12.90 ± 0.40
$(p_{3/2})_n^{-1}(s_{1/2})_\Lambda$, 1^-	6.04 ± 0.1	6.58 ± 0.20	7.26 ± 0.30	6.53 ± 0.18
$(p_{1/2})_n^{-1}(p_{3/2})_\Lambda$, 2^+	1.73 ± 0.1	2.74 ± 0.13	–	2.02 ± 0.18
$(p_{1/2})_n^{-1}(p_{1/2})_\Lambda$, 0^+	–	–	2.60 ± 0.09	
$(p_{3/2})_n^{-1}(p_{1/2,3/2})_\Lambda$, 2^+	-4.32 ± 0.1	-3.14 ± 0.11	–	-4.23 ± 0.09
$(p_{3/2})_n^{-1}(p_{1/2})_\Lambda$, 0^+	–	–	-3.93 ± 0.08	
$(s_{1/2})_n^{-1}(s_{1/2})_\Lambda$,$0^+$	–	–	~ -12	

Table 3.2: Λ *binding energy of* ${}^{10}_{\Lambda}B$ *[MeV]*

configration, spin	(π^+, K^+)[39] KEK	(K^-, π^-) [11] BNL	emulsion [40]
$(p_{3/2})_n^{-1}(s_{1/2})_\Lambda$,$2^-$	8.1 ± 0.2	~ 8	
$(p_{3/2})_n^{-1}(s_{1/2})\Lambda$ (ground state)			8.89 $\pm$0.12

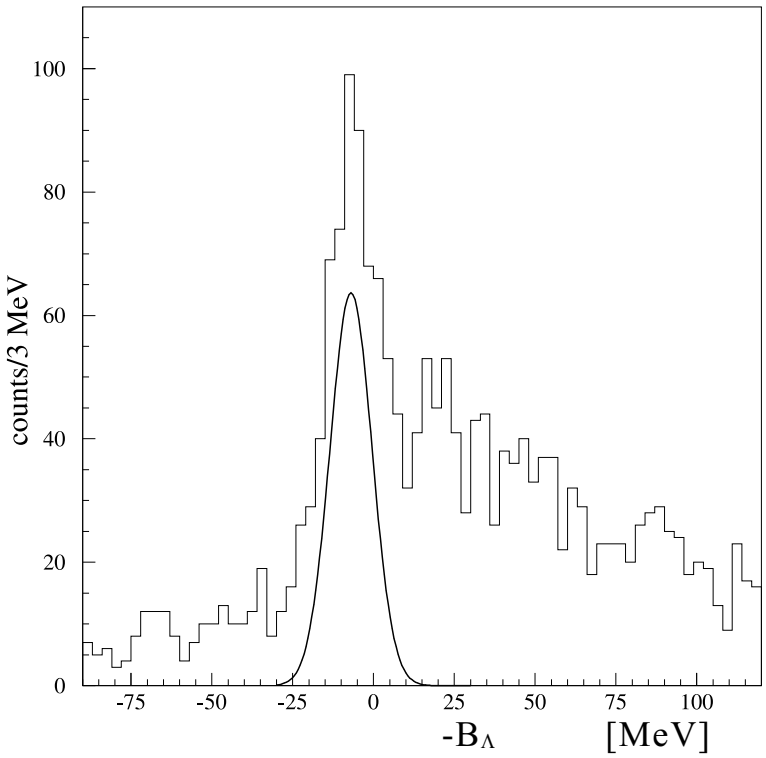

Figure 3.6: *Mass spectrum of* ${}^{16}_{\Lambda}O$ *with* γ*-energy gated for the* $1^- \rightarrow 0^-$ *and the* $1^- \rightarrow 1^-$ *transitions. Solid line shows the Gaussian peak of the fitting result.*

Chapter 4

Analysis -Gamma Rays

4.1 Event selection

We selected "good γ ray" events in the Hyperball data analysis. The "good γ ray" event has a germanium detector hit in the proper TDC timing without hits in the surrounding BGO counter in the same timing.

4.1.1 Germanium detector

TDC cut

Figure 4.1 shows a plot of TDC of a typical germanium detector for various ADC ranges, (a) for a TDC of CRM output and (b) for a TDC of TFA output. As shown in the figure, the time resolution of TFA was much better. We set a gate in TFA TDC. Figure 4.2 shows the TDC gate width as a function of the γ-ray ADC.

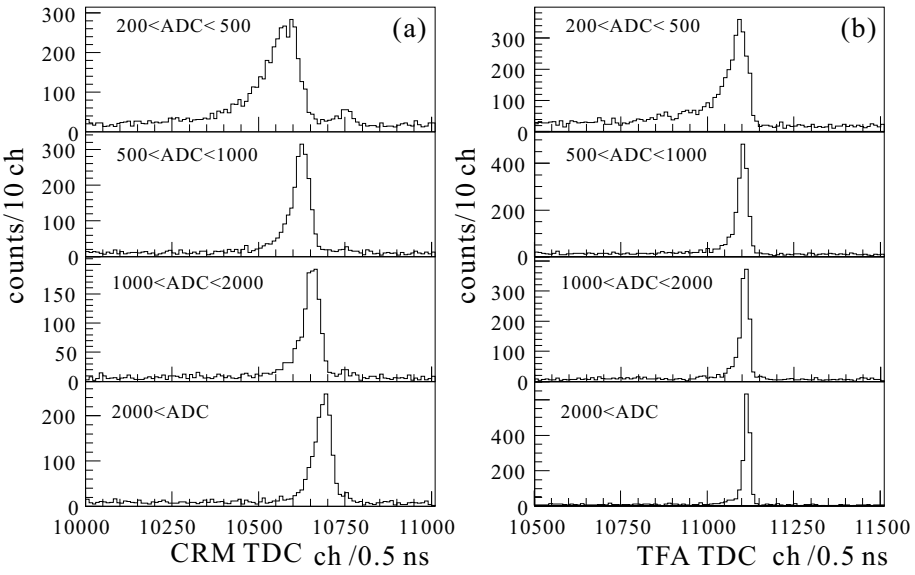

Figure 4.1: *TDC of a typical germanium detector for various ADC ranges. TDC was in the common stop mode. (a) is for the CRM output and (b) is for the TFA output. One channel of ADC corresponds to an energy of 0.9 keV.*

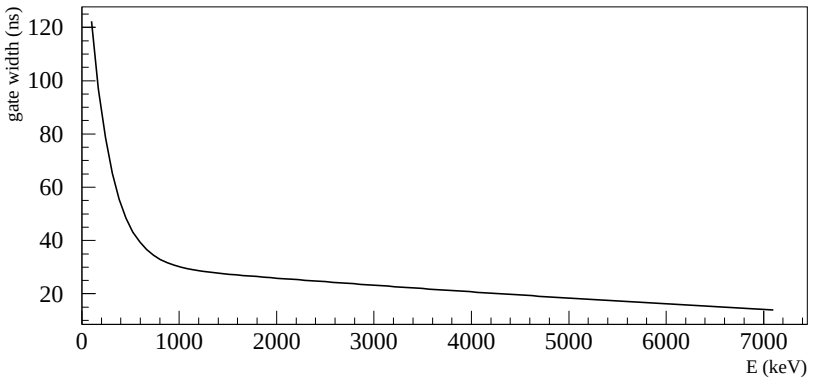

Figure 4.2: *Germanium detector TDC gate width as a function of γ energy*

TDC prompt cut

We prepared another TDC cut condition, "prompt cut", to eliminate background γ rays from (n,n'γ) reaction. Figure 4.3 shows the TFA timing of a typical germanium detector, and "A" indicates the "prompt timing" and "B" indicates the "non-prompt timing". A neutron reached the detector medium a few ns after γ rays from the target. Although the time resolution of the germanium detector for TFA output is typically 12 ns (FWHM) for the γ-ray energy over 2 MeV, such prompt γ rays and neutron-induced γ rays could be partly discriminated. Figure 4.4 shows the γ-ray spectrum plotted for these cut conditions. (a) is for the prompt timing and (b) is for the non-prompt timing. γ rays originated from the target nucleus (such as ^{14}N) survive in A but are slightly suppressed in B, while γ rays from (n,n') reaction by surrounding material (such as ^{27}Al, ^{56}Fe, ^{74}Ge, etc) survive in B but are clearly suppressed in A. Since neutrons are slow, we can eliminate the γ rays from (n,n' γ) reaction by the prompt timing cut. Thus we used these cut conditions to identify γ-ray origins.

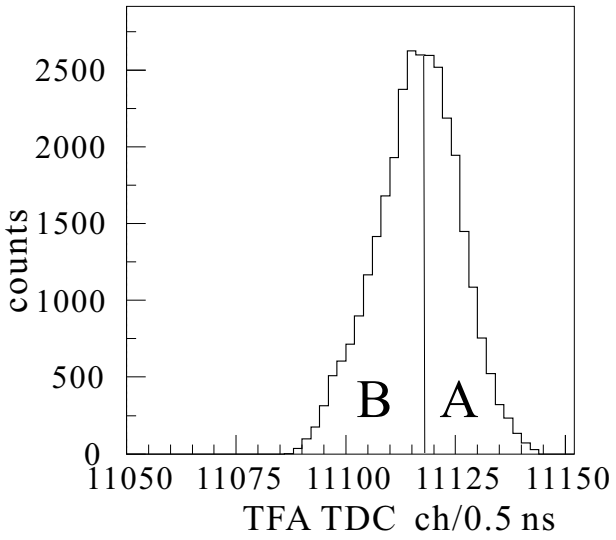

Figure 4.3: *A typical TDC spectrum of a germanium detector TFA signal. TDC was in the common stop mode. "A" indicates the prompt timing, and "B" indicates the non-prompt timing.*

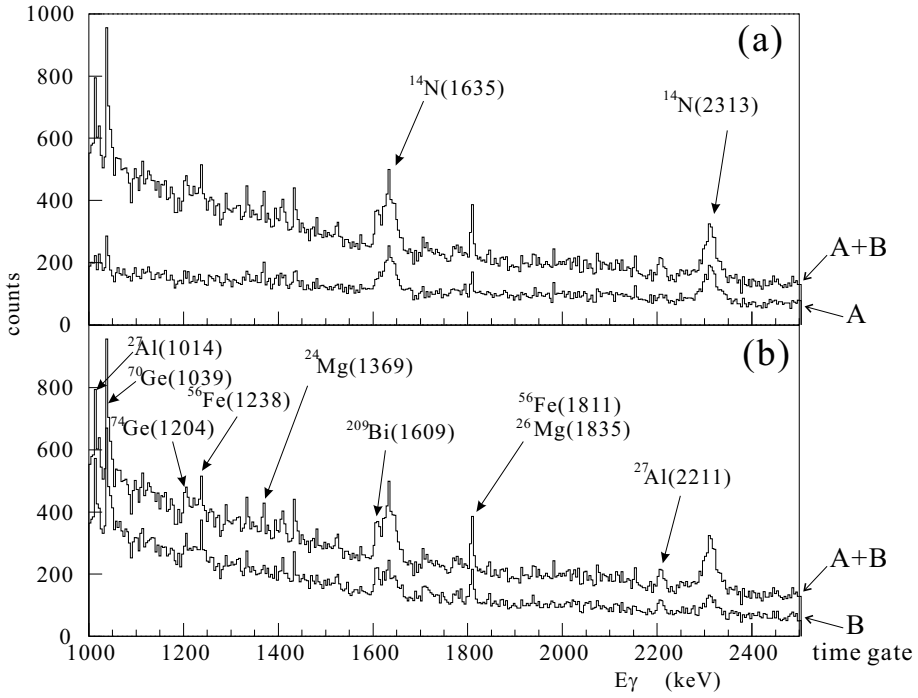

Figure 4.4: *γ-ray spectrum with "prompt cut" in beam coincidence. (a) is plotted for the normal TDC cut (A+B) and the prompt cut (A), and (b) is plotted for the normal TDC cut (A+B) and the non-prompt cut (B). The timing gate of A and B are defined in Fig.4.3*

Pileup rejection

With a multi-hit within about 3 μs in the same germanium detector, the γ-ray spectrum was distorted by the signal pileup. Figure 4.5 shows the illustration of the output signals of UHA for a pileup event. The relation between γ-ray energy spectrum around 511 keV (e^+e^-, annihi.) peak and CRM timing is shown in Fig.4.6. The true hit timing, not plotted in the figure, is adjusted to 0 μs. In this figure, the 511 keV peak are distorted in the time region from 3.6 μs to -3.0μs. Therefore, a germanium detector hit with another hit in the same detector within this time region was rejected.

Pre-reset rejection

A germanium detector hit within 20 μs after the preamplifier reset should be also rejected. Pre-reset causes the γ-ray peak broadened by base-line shift and also make a fake peak at a particular energy in the γ-ray spectrum by a reflected pulse in UHA.

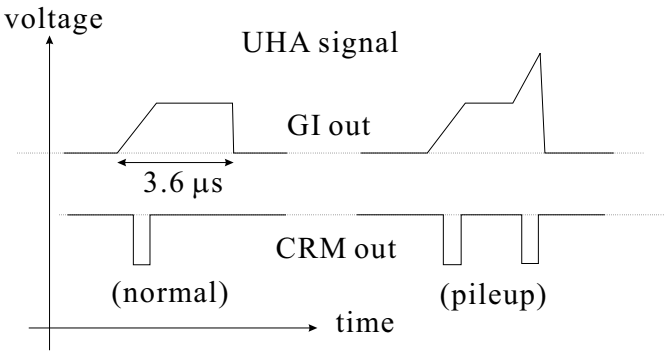

Figure 4.5: *Conceptual illustration of output signals of a UHA for pileup event*

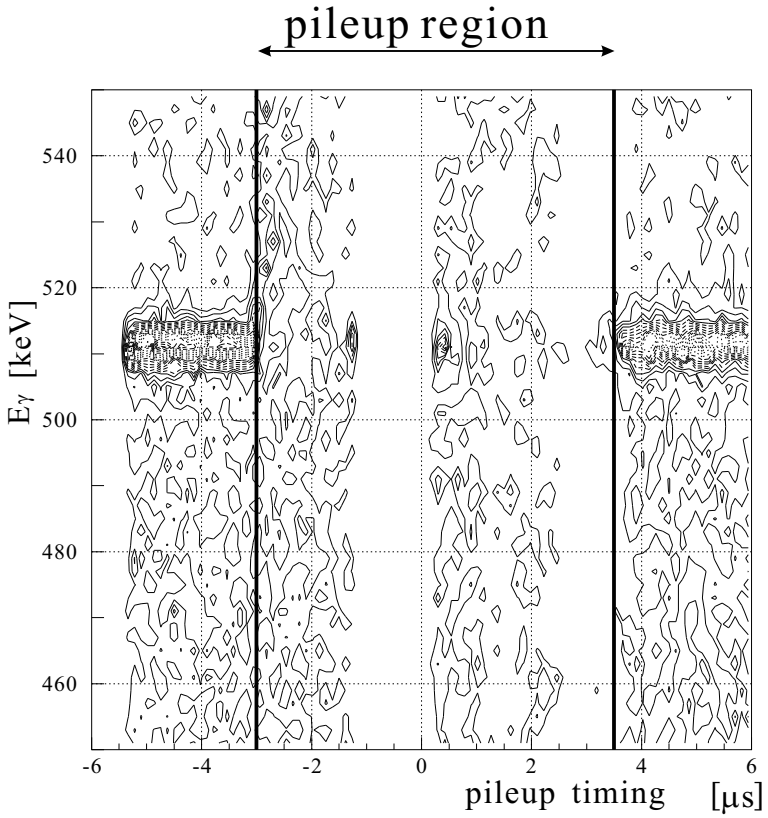

Figure 4.6: *Relation between pileup time and γ-ray energy for pileup events The pileup time is defined as CRM (pileup) -CRM (true). Plus sign means pre-pileup and minus sign means post-pileup.*

4.1.2 BGO counter

Pedestal correction

Since the ADC gate width for the BGO detectors was as large as 1 μs, the collected charge of BGO signals was suffered from electrical pick-up noise. As shown in Fig. 4.7 (b), a pedestal of BGO ADC was broadened for 200 ch. We used a "noise monitor" ADC to correct broadened pedestals. Figure 4.7 (a) shows ADC pedestal fluctuation between a BGO ADC and the noise monitor channel ADC. The noise monitor channel is nothing but a channel without any input signal in the same ADC module.

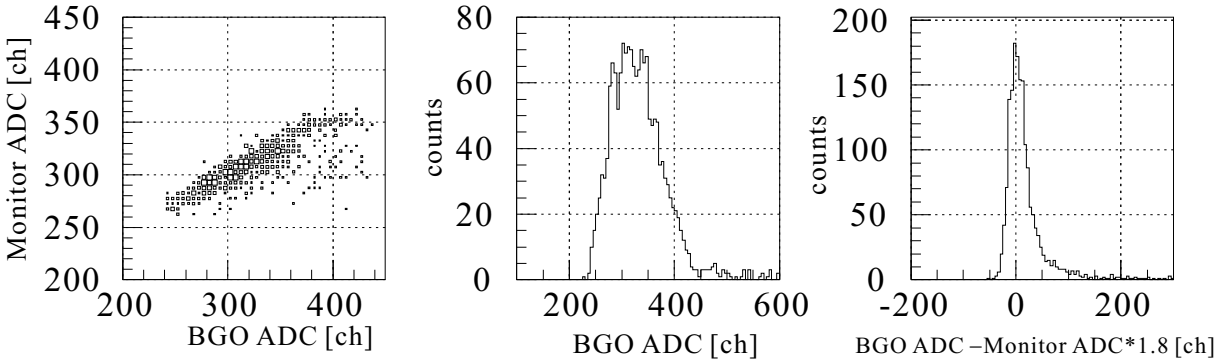

Figure 4.7: *"Noise monitor" ADC and BGO ADC pedestals for a typical BGO counter (a) Correlation between noise monitor channel and a BGO channel, (b) raw BGO ADC pedestal, and (c) corrected BGO ADC pedestal.*

TDC cut

We set the time gate width of the BGO detectors at 50 ns and the pedestal ADC threshold of the corrected BGO ADC at 25 ch. It was determined by means of signal-to-noise ratio (S^2/N and S/N). When one or more BGO counter TDC's have hits in this timing gate with ADCs larger than the pedestal threshold, a hit in the corresponding germanium detector is rejected. Figure 4.8 shows the spectrum of the timing and corrected ADC for BGO detector of one crystal, and the solid lines show the rejected region.

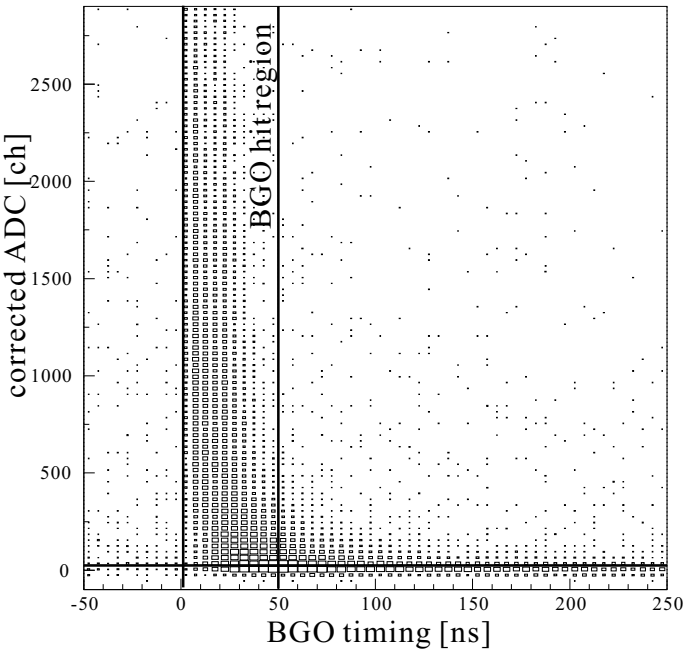

Figure 4.8: *A typical spectrum of the timing versus the corrected ADC for a BGO counter. Solid lines indicate cut region for the background suppression for the corresponding germanium detector.*

4.2 Calibration of germanium detectors

4.2.1 Energy calibration

Calibration curve

For the energy calibration of the germanium detectors, we used two types of γ-rays, γ-rays from sources and delayed γ rays originated from the beam. The γ rays in use for the calibration are summarized in Table 4.1.

The expected energies of γ rays from ${}^{16}_{\Lambda}$O are higher than 6.2 MeV. The γ-ray sources were not available for this region; the highest energy we could use was 6129 keV from ^{244}Cm+^{13}C (^{13}C+$\alpha \rightarrow {}^{16}$O+$\gamma$(6129)+$n$) source. From the off-beam calibration data, we found five γ-ray peaks in the region from 5 MeV to 7 MeV as described in Table 4.1. Figure 4.9 shows the γ-ray spectrum of off-beam data and those γ-ray peaks were found in this figure.

Table 4.1: *γ-rays in use for the energy calibration*

parent	$\tau_{1/2}$	energy [keV]		from
annihi.		511.0		
^{60}Co		1173.2		γ-ray source
		1332.5		
^{152}Eu		344.3		γ-ray source
		778.9		
		964.0		
		1528.7		
^{16}N	7.14 s	6128.6		delayed γ^*
		5617.6	SE6129	
		5106.6	DE6129	
		7115.2 #		delayed γ^*
		6604.2	SE7115	
^{14}O	1.18 m	2312.6		
^{75}Ge$_m$	48.3 s	139.8		delayed γ
^{24}Na	15.0 h	2754.1		delayed γ

*weak intensity, found in the histogram summed up for all runs.

#not observed in nine out of the fourteen germanium detectors due to out of range.

SE and DE mean single-escape peak energy and double-escape peak energy, respectively.

Due to the wide energy range, a function to convert the ADC channel to the energy was required to have high order terms of polynomials. Even for a cubic function, residuals between the real γ-ray energies and the measured and calibrated energies were larger than 2 keV for the largest one. So we prepared three calibration curves for each germanium detector. They correspond to the ranges from 0.1 to 1.3 MeV , 1 to 6 MeV and 5.5 MeV to 7 MeV which are a quadratic function, a cubic function and a liner function, respectively. Figure 4.10 shows the residuals of calibrated energy from real energy for the calibration points for a typical germanium detector, (a) for the range

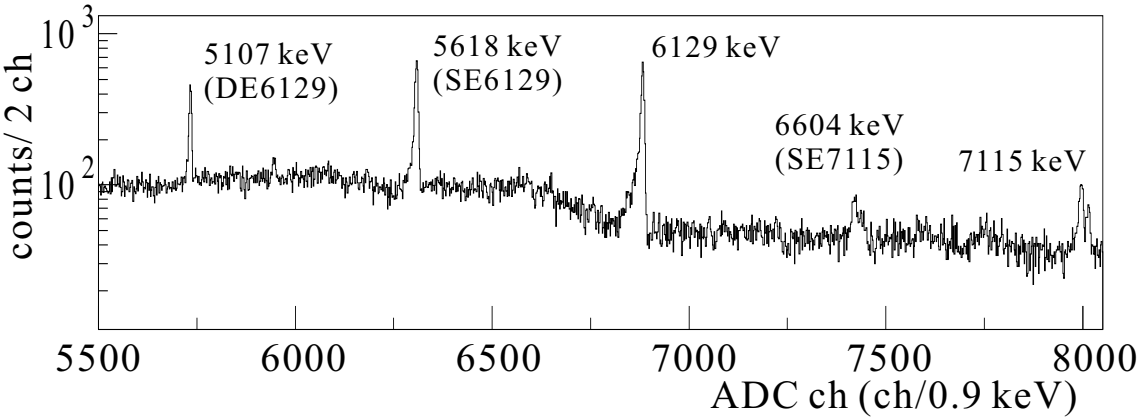

Figure 4.9: *Delayed γ-ray peaks found in off-beam germanium detector data. All of those peaks were from the $^{16}N \rightarrow {}^{16}O^{*} + \beta^{-}$ process.*

from 0.1 to 1.3 MeV, (b) for from 1 to 6 MeV and (c) for from 5.5 MeV to 7 MeV. The largest residual for the worst detector was 1.5 keV.

Peak shift

As described in Chapter 2.6.4, the calibration data of the germanium detectors were continuously taken during the beam time for the in-beam and the off-beam periods by the main DAQ system. We checked (1) the peak shift between the in-beam and the off-beam periods and (2) the long-time drift for the peaks of 511 keV and 1.33 MeV.

- Peak shift between the in-beam and the off-beam period

  We checked the peak position shift for the same γ-ray peak between the in-beam and the off-beam periods. Figure 4.11 shows the peak shift in ADC channel for a typical germanium detector between the in-beam and the off-beam periods. (a) is the peak shift for the 511 keV peak and (b) is for the 1.33 MeV peak. The peak shift was almost constant between different runs and between different energies. The averaged shifts were different for detector by detector, and the smallest one was 0.15 ch and the largest one was 2.1 ch, corresponding to 0.14 keV and 1.9 keV, respectively.

- Peak shift between runs

  We checked the long-time drift of the peak position. Figure 4.12 shows the peak position versus the run number. (a) is for the 511 keV peak and (b) is for the 1.33 MeV peak. The peak position drifted within about 2 ch (corresponding to 1.8 keV). We also checked the ADC spacing between different energies, namely, ADC channel for the 1.33 MeV peak minus that for the 511 keV peak, as shown in Fig. 4.13. The ADC drift was found to be almost constant independently of the energy.

From these results, we assumed that the peak shift for each detector was constant independent of energy, and the peak drift depends on run number.

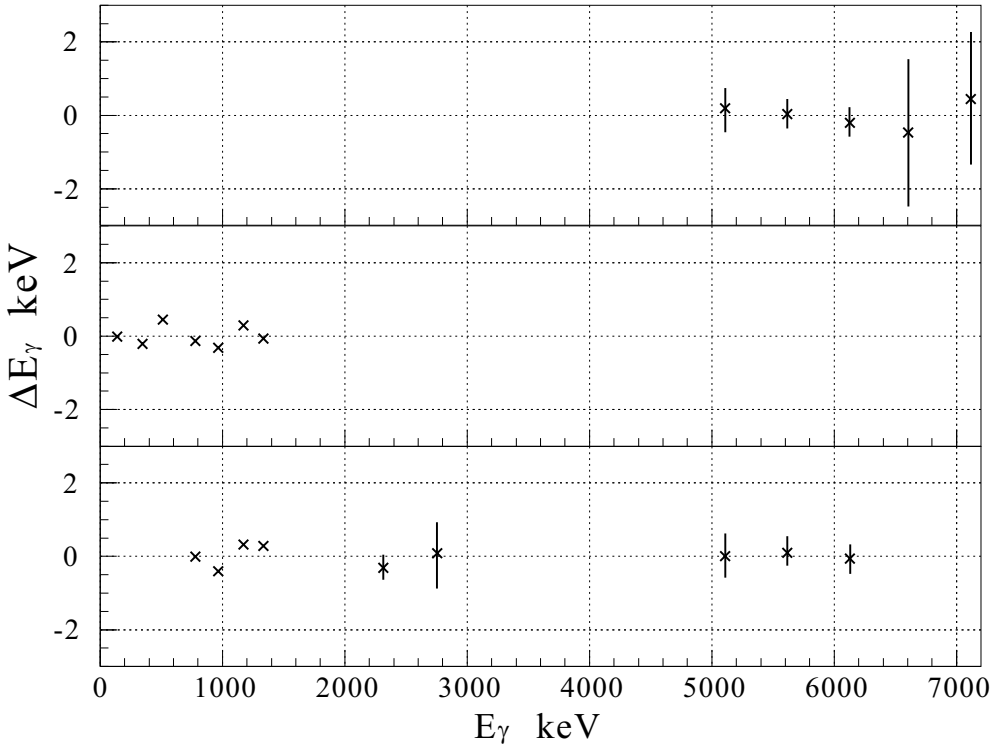

Figure 4.10: *Residuals of γ-ray energy between the calibrated energy and the real energy for a typical germanium detector. (a): from 0.1 to 1.3 MeV, (b): from 1 to 6 MeV, and (c): for from 5.5 meV to 7 MeV.*

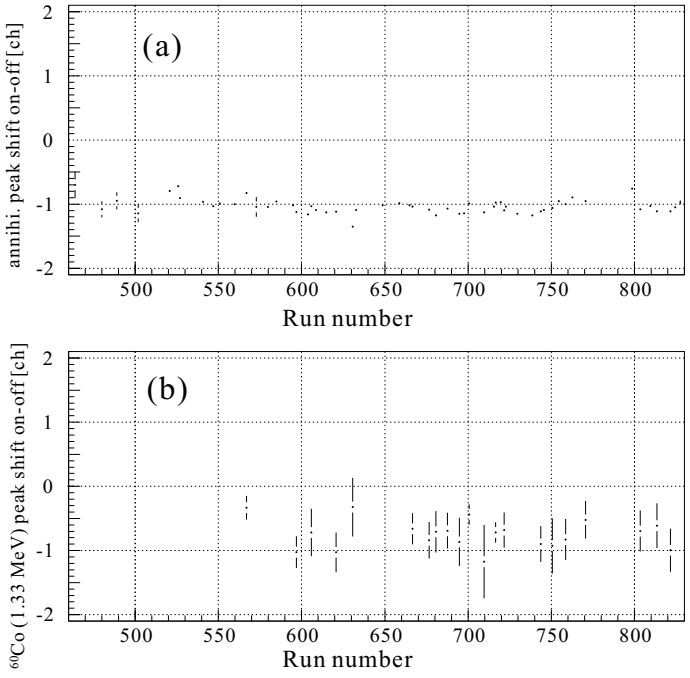

Figure 4.11: *Peak shift of ADC channel for a typical germanium detector between on-beam and off-beam period in the same run. The γ rays were measured in the main DAQ calibration system. One channel corresponds to 0.9 keV. (a) shows the peak shift of annihilation γ ray (511 keV), and (b) the peak shift of ^{60}Co γ ray(1.33 MeV).*

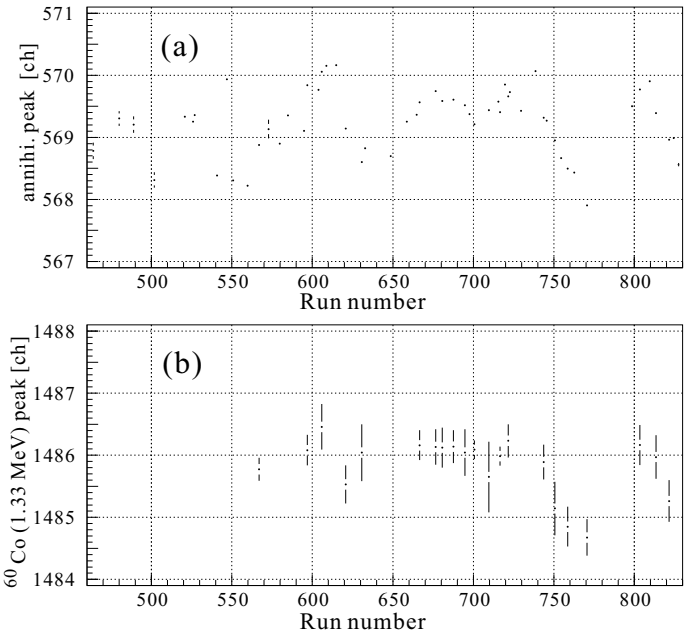

Figure 4.12: *Long-term drift of γ ray peak position in ADC channel for a typical germanium detector. The γ rays were measured in the main DAQ calibration system. (a) Peak position of annihilation γ ray (511 keV) and (b) peak position of ^{60}Co γ ray (1.33 MeV).*

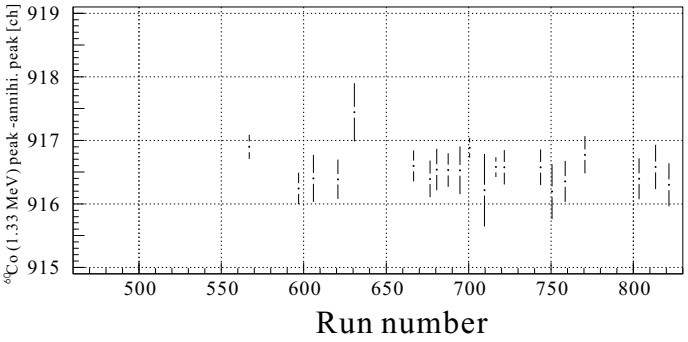

Figure 4.13: *Long-term drift of γ ray peak position plotted for ADC difference between 511 keV (annihi.) and 1.33 MeV (^{60}Co).*

4.2.2 Photo-peak efficiency

The coincidence efficiency for a particular energy was measured by γ-γ coincidence method. When a germanium detector detected a γ_1 we measured the summed up detection efficiency for γ_2 of other 13 detectors, where γ_1 and γ_2 were γ transitions of the same nuclei. We used two cascade decays described in Fig. 4.14 which were originated from the target and detected in the beam coincidence. In the figure, γ_1 corresponds to γ(1022 keV) and γ(1635 keV) and γ_2 corresponds to γ(718 keV) and γ(2313 keV), respectively. And the total efficiency was estimated to be 14/13 times as much as the measured coincidence efficiency. Thus we obtained the coincidence efficiencies of 1.42 ± 0.29 % at 2313 keV and 3.94 ± 0.90 % at 718 keV for the water target. These efficiencies included the analysis efficiencies.

The efficiency as a function of energy was simulated by GEANT with all materials of Hyperball between the target and the germanium crystals. The simulated efficiency did not include electronics the dead time of the germanium detector and the analysis efficiencies. We plotted the simulated efficiency curve in Fig. 4.15 which was normalized by the measured coincidence efficiencies. The shadowed region in the figure is the simulated efficiency with normalization.

Some of the germanium detectors were in trouble during the beam time, and the net working rate of the germanium detectors was 95 % for the water target run period and 100 % for the ^{10}B target run period. Thus we defined the efficiency for the ^{10}B target to be $\varepsilon_\gamma^{water} \times 1.05$

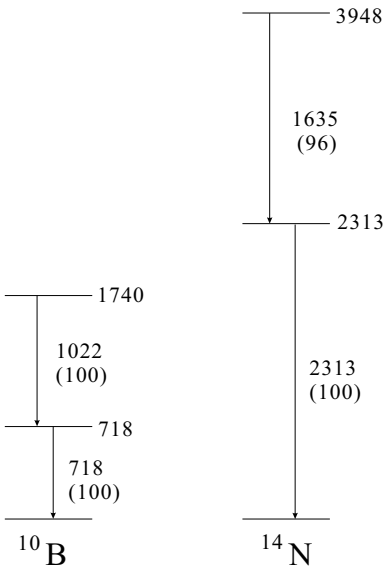

Figure 4.14: *Schematic diagram of cascade decays used for efficiency estimation*

4.2.3 Summed up response function and energy resolution

We checked the response function of γ-ray peak. Figure 4.16 shows the γ-ray spectrum in beam coincidence with the water target. In the spectrum, two γ-ray peaks exist, which are assigned as ^{16}O(6129) and ^{15}O(6175) from the peak energies. We fitted the spectrum with two Gaussian functions and a linear background. It is fitted well with χ^2/DOF of 1.1. Accordingly, we assumed the response function of the germanium detector in beam coincidence as a Gaussian function.

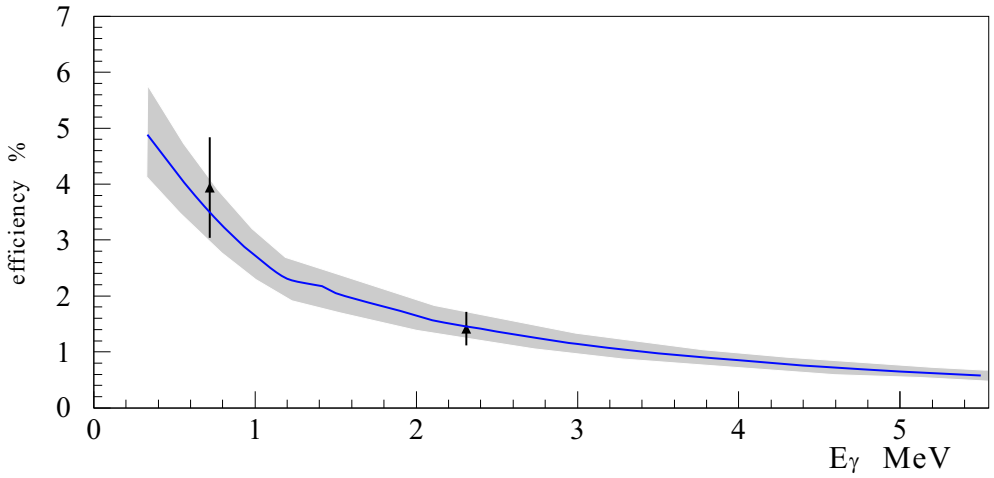

Figure 4.15: *Total photo-peak efficiency of Hyperball for the water target run. The solid line shows the result of simulation. The shadowed region shows the expected efficiency. For the ^{10}B target the efficiency is larger by a factor of 1.05 than that of the water target (see the text).*

We also checked the energy resolution as a function of energy. We fitted four prominent γ-ray peaks which have lifetimes larger than 5 ps. These results are summarized in Table 4.2. We assumed the squared energy resolution to be a linear function of energy;

$$\delta E_{total} = \sqrt{A \cdot E_\gamma + \delta E_{etc}^2}$$

where A and δE_{etc}^2 are parameters and obtained by fitting the measured energy resolution. Figure 4.17 shows the obtained energy resolution in σ, where the solid line shows the fitting result. We obtained $A = 1.70 \times 10^{-3}$ keV and $\delta E_{etc}^2 = 2.35$ keV^2 .

Table 4.2: *γ-ray peaks used for the resolution estimation*

nuclei	energy [keV]	resolution (σ) [keV]	lifetime [ps]
^{10}B	718	1.87±0.23	707
$^{7}_{\Lambda}$Li	2050	2.42±0.42	5.8
^{13}C	3853	3.18±0.56	8.6
^{16}O	6129	3.54±0.34	18

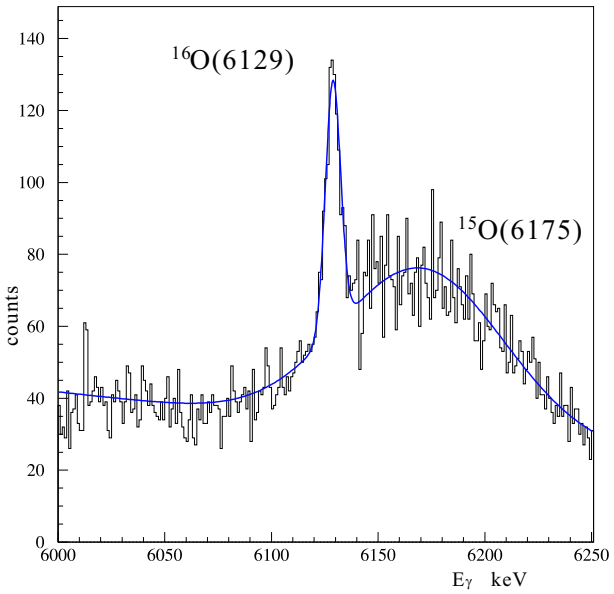

Figure 4.16: *γ ray spectrum fitted with Gaussian function.*

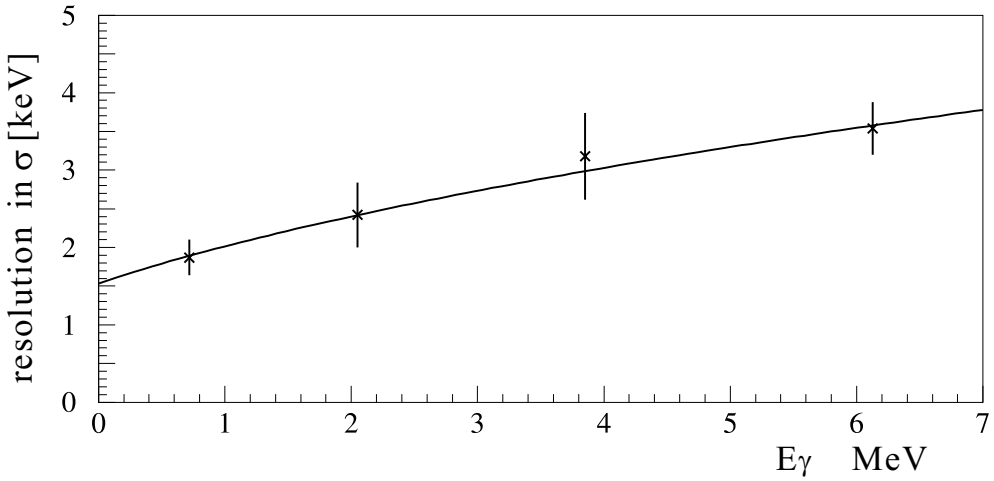

Figure 4.17: *Energy resolution of γ-ray spectrum summed up for all the germanium detectors. Solid line shows the expected energy resolution.*

4.3 Doppler shift of γ rays

4.3.1 Doppler-shift correction

When the γ-ray energy is larger than a few hundred keV, the M1 transition γ-ray is expected to have a much shorter life time than the stopping time of recoiling hypernucleus in the target medium. The E2 transition γ rays of ${}^{9}_{\Lambda}$Be also have a shorter life time than stopping time. The M1 transition probability is estimated by the Weisskopf formula, $w = 3.12 \times 10^{13} \times E_{\gamma}^{3}$ sec^{-1}. Figure 4.18 shows the life time for M1 γ-ray emission for the single particle estimation. The γ-ray energy should be broadened due to the Doppler-shift effect. While we know the velocity and the direction of the recoiling hypernucleus and the direction of the γ ray, the measured energy of γ ray can be corrected by the formula,

$$E_{\gamma}^{corrected} = \frac{1}{\sqrt{1-\beta^2}} \cdot (1 - \beta \cos\phi) \cdot E_{\gamma}^{measured}, \tag{4.1}$$

where $E_{\gamma}^{corrected}$ and $E_{\gamma}^{measured}$ are the Doppler-shift corrected energy of the γ ray and the measured energy of the γ ray, β is the recoil velocity of hypernuclei and ϕ is the angle between the γ ray and the hypernucleus in the laboratory frame. The recoil velocity and the direction of the hypernucleus are obtained from the measured kaon and pion momenta and trajectories. The γ-ray vector is calculated by the reaction vertex point and the position of the germanium crystal with hit. The γ-ray energy can be corrected event-by-event.

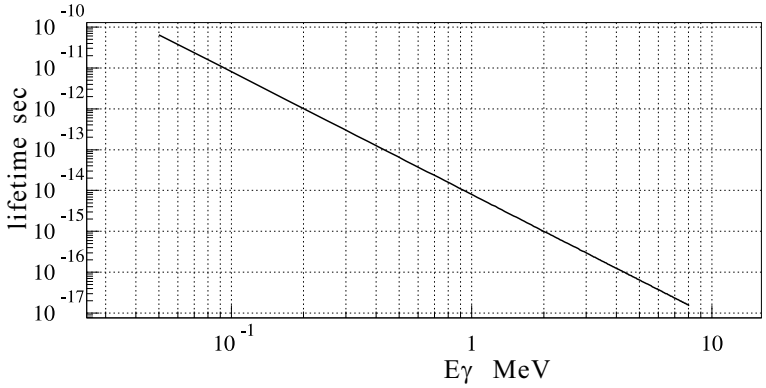

Figure 4.18: *Life time for M1 γ-ray transition with single particle estimation*

4.3.2 Expected peak shape of γ-ray spectrum

We simulated the peak shape broadened by Doppler shift and the peak shape after the Doppler-shift correction by Monte-Carlo method. We took account of the following points in the simulation.

- Intrinsic response function of the germanium detectors.

  We assumed the original response function as a Gaussian function.

- Ambiguity of the γ-ray direction resulted from the germanium crystal size and the vertex resolution.

When we corrected the γ-ray energy, we assumed that the γ-ray is emitted at the measured vertex point and absorbed at center of the germanium crystal. In reality, the germanium crystal has a finite size and the measured vertex resolution. In the simulation we assumed that the γ ray hits a spherical crystal of 3.5 cm in radius and the vertex point distributes in a Gaussian of 1.5 cm in σ.

γ rays from directly populated states

Figure 4.19 shows the simulated peak shape of a Doppler-broadened γ ray before and after the Doppler-shift correction in the case of ${}^{16}_{\Lambda}$O. Since the emitted γ ray and the outgoing π^- have an angular correlation, we also took account of it. However, it did not affect the peak shape.

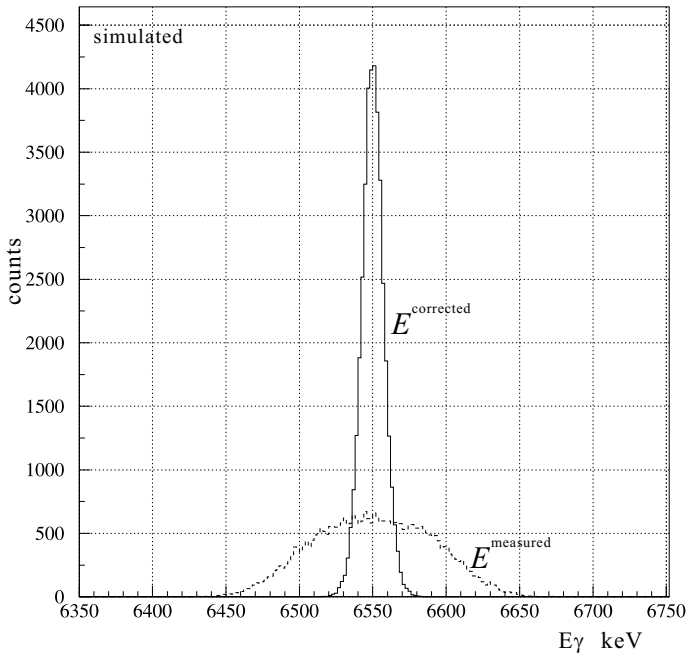

Figure 4.19: *Simulated peak shape of ${}^{16}_{\Lambda}O$ γ ray (assumed to be at 6550 keV). Dashed line shows the Doppler-broadened peak shape and sold line shows the Doppler-shift corrected peak shape.*

γ rays from hypernuclei produced as fragments

Some excited states of ${}^{15}_{\Lambda}$N and ${}^{9}_{\Lambda}$Be are produced as fragments following proton emission of high excited states of ${}^{16}_{\Lambda}$O and ${}^{10}_{\Lambda}$B. Their recoil direction and velocity are changed from those of the parent's and we have no idea to know them. We simulated the Doppler-shift corrected peak shape of a γ ray from hyperfragment, ${}^{A-1}_{\Lambda}$Z-1, with the recoil velocity and direction of the parent hypernucleus, ${}^{A}_{\Lambda}$Z. In this simulation we assumed that (1) the parent nucleus,${}^{16}_{\Lambda}$O(${}^{10}_{\Lambda}$B) was excited to E^{par}_{ex}= 17 MeV (11 MeV), and that (2) the daughter ${}^{15}_{\Lambda}$N(${}^{9}_{\Lambda}$Be) was excited to E^{dau}_{ex}= 4.5 MeV(3.0 MeV). Here we assumed that there were no angular correlation between the daughter nucleus and the parents nucleus.

Figure 4.20 and 4.21 are the simulated peak shape. When we change E^{par}_{ex} or E^{dau}_{ex}, the peak shape may slightly change.

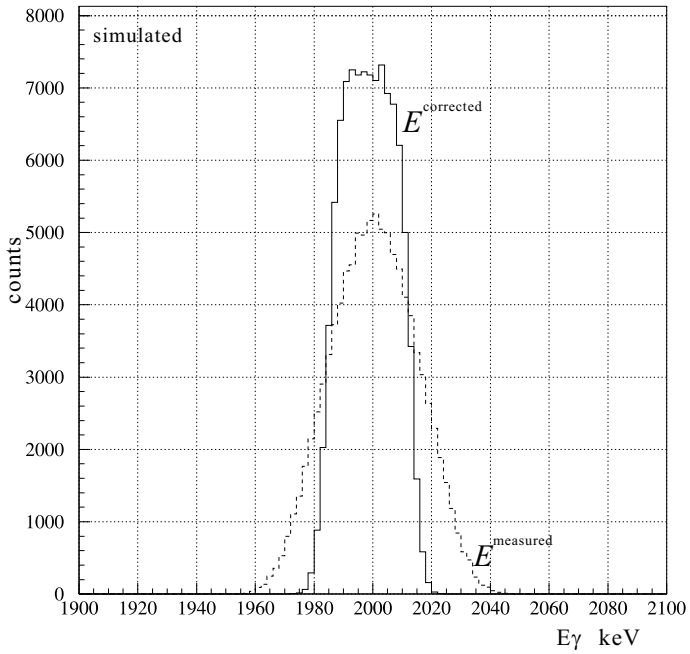

Figure 4.20: *Simulated γ-ray peak shape of ${}^{15}_{\Lambda}N$ (assumed to be at 2000 keV) Dashed line shows the Doppler-broadened peak shape and sold line shows the Doppler-shift corrected peak shape.*

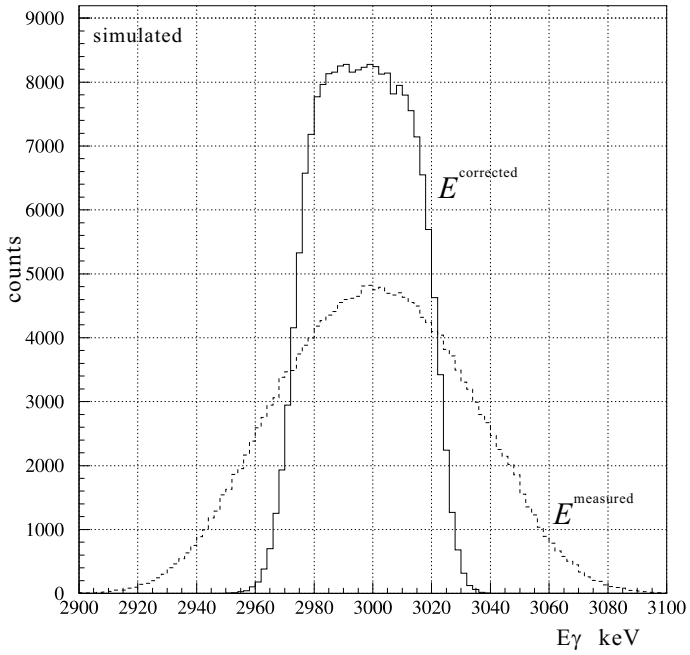

Figure 4.21: *Simulated γ-ray peak shape of ${}^{9}_{\Lambda}Be$ γ ray (assumed to be at 3000 keV) Dashed line shows the Doppler-broadened peak shape and sold line shows the Doppler-corrected peak shape.*

4.4 Background function

We will discuss background of the γ-ray spectrum. The background is fitted well with a parabolic function, when there is no γ-ray peak. With a narrow fitting region, the background might be fitted with a linear function. When we fit the γ-ray peak with a background, the continuum γ rays from multi-Compton scattering have to be taken into account, because the energy of γ ray escaping from the germanium detector was not only via a single Compton scattering but also via multi-Compton scattering in which the deposit energy to the detector ranged from the energy of the Compton edge to the energy of the full-energy peak. As a result, the background curve becomes discontinuous at the photo-peak energy. The effect of multi-Compton scattering on the background is more pronounced for a higher γ-ray energy. We restricted the fitting region and assumed a linear background. Then we added the multi-Compton continuum, if necessary. We prepared the following background function and used them for the fitting.

- Fig. 4.22 (a) linear function

  We used it up to 3 MeV. We assumed that for this region the γ-ray energy is absorbed by the photoelectric effect directly without other processes. This approximation seems well for this region.

- Fig. 4.22 (b) linear + peak combined linear function

  We used it for the energy over 3 MeV. We draw the linear background so that it connects the background levels just below and over the peak. We assumed that the multi-Compton scattering background has a response function, $1/(1 - \exp(E_\gamma - E_0)/\sigma)$, where E_0 is the peak energy. When the response function for a discrete γ ray is a Gaussian, σ is the same as the Gaussian's σ. For this region, γ-ray spectrum seems to be fitted better with this combined background than with a linear background.

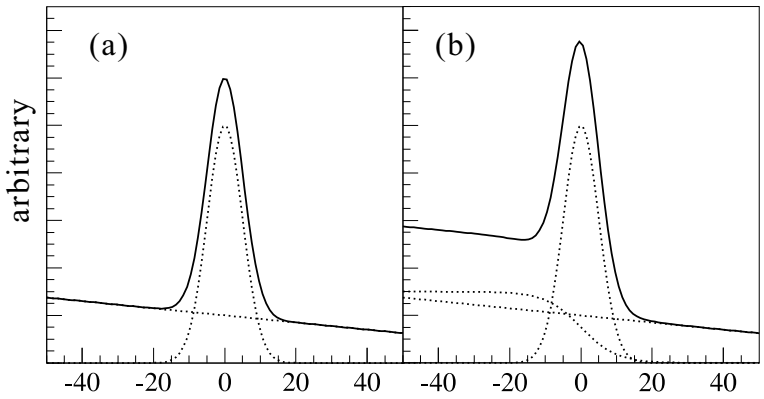

Figure 4.22: *Shapes of associated γ-ray background: (a) is a peak with a linear background, (b) is a peak with linear + peak combined linear background. Each definition is described in the text.*

4.5 Overall systematic error of γ-ray energy

We took account of the systematic errors in the following points,

- Calibration error

  We take a systematic error of 1.0 keV bellow 2 MeV and 1.5 keV over 2 MeV from the residuals of calibrated energies (see Fig. 4.10).

- Uncertainty of Doppler-shift correction

  Ambiguity of the center position of the z-vertex distribution was expected to be less than 5 mm. It included the uncertainty of the coordinate system of the Hyperball and chambers. We simulated the energy shift in the case that the vertex was shifted 5 mm, and we obtained the energy shift value of 0.9 keV.

These systematic errors have some effect on the each peak energy but does not have effect the spacing energy in the case of a small spacing.

Chapter 5

Results from the ^{16}O$(K^-, \pi^-\gamma)$ Experiment

5.1 M1 γ rays of $^{16}_{\Lambda}$O

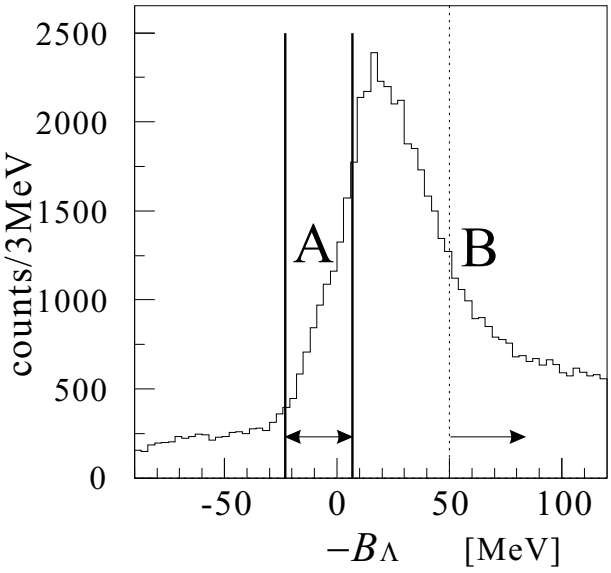

Figure 5.1: *Missing mass spectrum of $^{16}_{\Lambda}O$ plotted against $-B_\Lambda$ for those events which accompany γ rays over 5 MeV. "A" indicates the region for the 6 MeV excited state of $^{16}_{\Lambda}O$ ($-22 < -B_\Lambda < 8$ MeV), and "B" indicates the region for highly unbound region ($-B_\Lambda > 50$ MeV)*

Figure 5.1 shows the mass spectrum of $^{16}_{\Lambda}$O plotted against $-B_\Lambda$ scale. Figure 5.1 is plotted for those events which accompany γ-rays over 5 MeV. In Fig. 5.1, "A" indicates the 6 MeV excited 1^- state region of $^{16}_{\Lambda}$O ($-22 < -B_\Lambda < 8$ MeV), and "B" indicates the highly unbound region ($-B_\Lambda > 50$ MeV). The mass gate width of 30 MeV was determined from the mass resolution of 15 MeV(FWHM), and the mass of the 1^- state was calibrated to be $-B_\Lambda = -7$ MeV as described in Sect. 3.7.2. So we set the mass gate for the 1^- state to be the range of $-7-15$ to $-7+15$ MeV.

Figure 5.2 shows the γ-ray spectra plotted in the range from 5.5 MeV to 7 MeV

with the mass selection of A and B. (a) is for the bound region "A" with Doppler-shift correction, (b) is for the bound region "A" without Doppler-shift correction, and (c) is for the unbound region "B" without Doppler-shift correction. Some prominent peaks appear in this energy region in the Doppler uncorrected spectra, and they are assigned as the γ rays from the water target, ^{16}O(6129 keV), its single escape peak (5618 keV), and ^{15}O(6175 keV). The 6175 keV peak is broadened by Doppler shift.

A broad structure was observed around 6.55 MeV only for the bound region (see Fig. 5.2 (b)) and it displays narrow peaks after Doppler-shift correction (see Fig. 5.2 (a)). Thus the peaks are assigned as γ rays of $^{16}_{\Lambda}$O. We also found a similar peak structure at 511 keV below these $^{16}_{\Lambda}$O γ peaks. They are assigned as the single escape peaks of the $^{16}_{\Lambda}$O γ rays around 6.55 MeV. Figure 5.3 (a) shows the γ-ray spectrum with Doppler-shift correction plotted for all $-B_{\Lambda}$. For Doppler-shift corrected γ-ray energies within the peak region indicated in Fig.5.3 (a), we plotted the mass spectrum as shown in Fig.5.3 (b). The peak at -7 MeV corresponding to the $^{16}_{\Lambda}$O 1^- state is clearly enhanced. As already mentioned, we used this peak for the calibration of the mass.

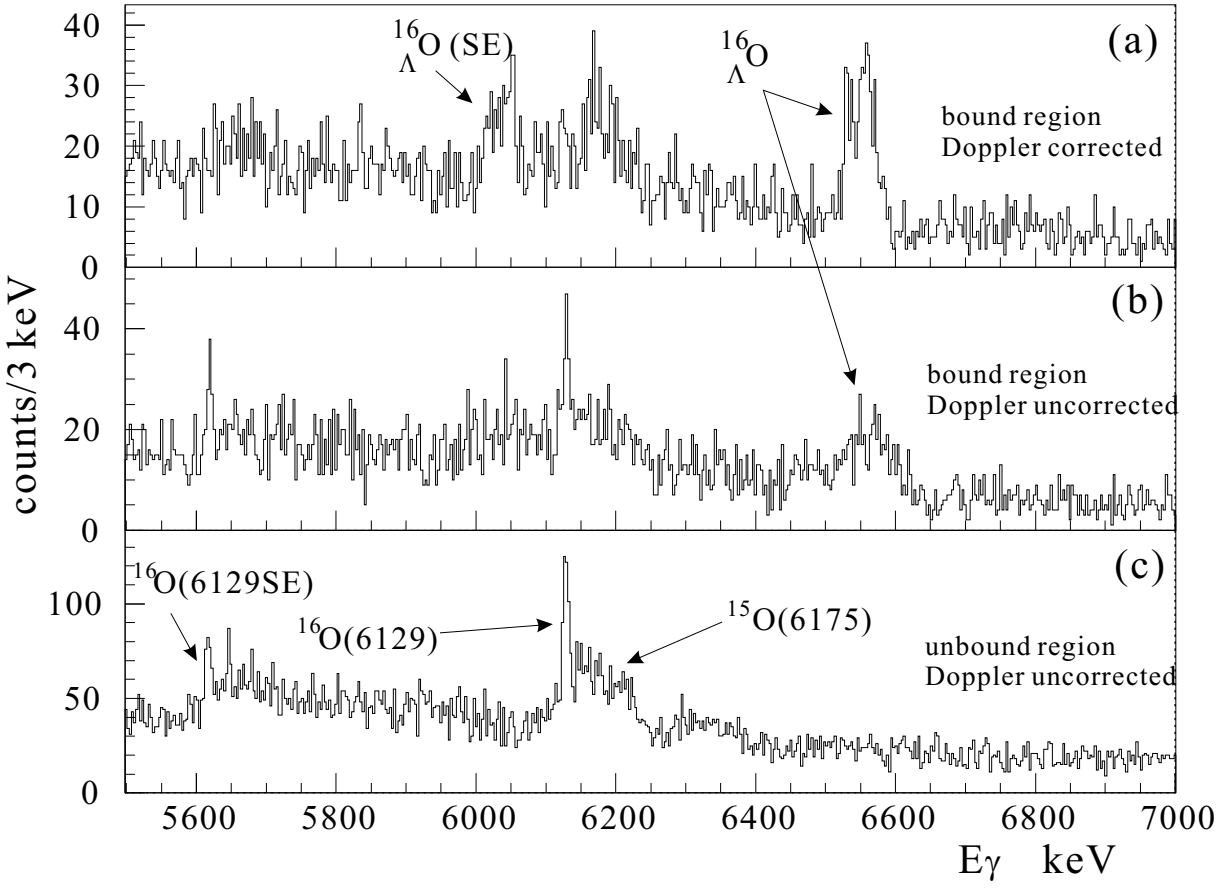

Figure 5.2: *Mass-gated γ-ray spectra over 5 MeV in the $^{16}O(K^-, \pi^-\gamma)$ reaction. (a) is for the bound region "A" and Doppler-shift correction was applied, (b) is for the bound region "A"and (c) is for the unbound region "B". The region "A" and "B" are defined in Fig. 5.1 and text.*

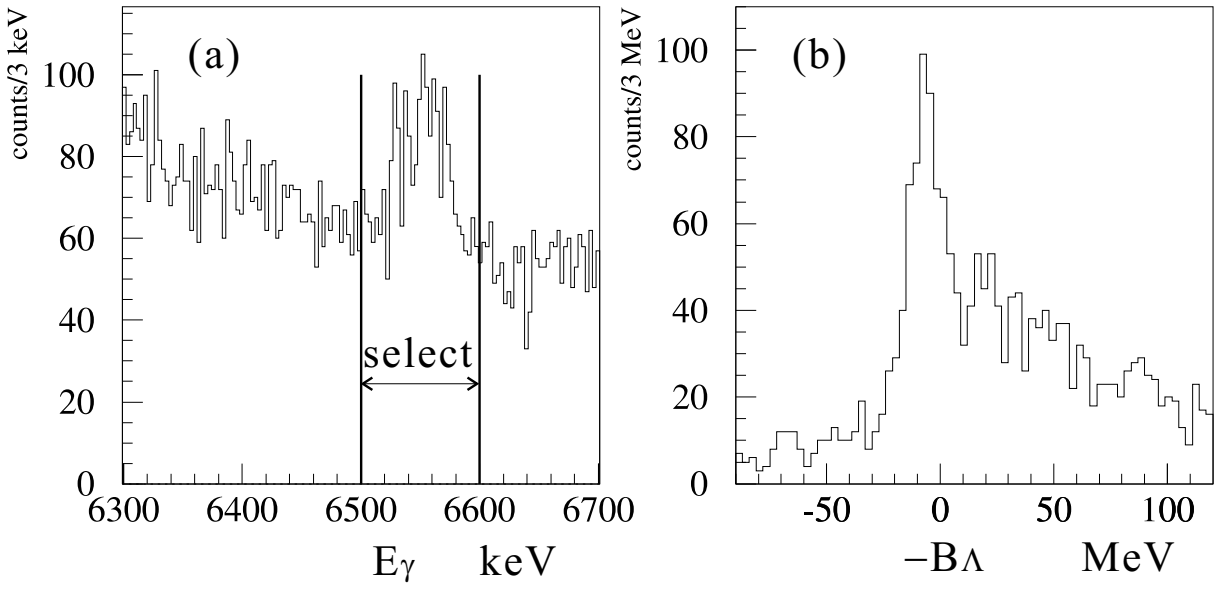

Figure 5.3: *(a) Inclusive γ-ray spectrum with Doppler-shift correction, (b) mass spectrum plotted for the Doppler-shift corrected γ-ray energy from 6500 keV to 6600 keV. The mass is calibrated in which the mean value of the peak in (b) to be $-B_\Lambda = -7$ MeV.*

5.1.1 The γ-ray energy and the yield ratio

In the ^{16}O(K^-,π^-) $^{16}_{\Lambda}$O reaction, only the 6 MeV 1^- state is populated among $^{16}_{\Lambda}$O bound states, except for the 1^- state in the ground-state doublet. In addition, since these γ-ray peaks were fully broadened by the Doppler effect as described later, the lifetime of the state was determined to be much less than 1 ps, the stopping time of the recoiling hypernucleus in the target medium. This result agrees with the fact that the lifetime of M1 transition of 6 MeV is estimated to be less than 0.1 fs. Although E1 or E2 transition would be consistent with the lifetime, in the weak-coupling limit the lifetime in $^{16}_{\Lambda}$O should be the same as that for the $\frac{3}{2}^- \rightarrow \frac{1}{2}^-$ M1 transition in ^{15}O. In addition, only the two 1^- states are strongly populated in the (K^-,π^-) reaction with 0.93 GeV/c kaon momentum. Thus, the observed 6.55 MeV γ rays are assigned as the M1 transitions from the 1^- state to the ground-state doublet.

We made a fit with a simulated peak shape (see Fig. 4.19) to obtain the energies of the transitions with some types of associated background which were discussed in Section 4.4. We made a fit for a two-peak structure and for a single-peak structure. Figure 5.4 shows the results. In Fig. 5.4, the background was assumed as "linear + peak combined linear" function. In those fittings, we obtained χ^2/DOF of 1.56 for the two-peak structure and of χ^2/DOF of 2.34 for the single-peak structure. This fitting result rejects interpretation to the single-peak structure. Fitting for the two-peak structure, we obtained the peak energies of $6534.1 \pm 1.5 \pm 1.7$ and $6560.2 \pm 1.3 \pm 1.7$ keV, yields of $136 \pm 16 \pm 5$ and $210 \pm 30 \pm 5$ counts, and a ratio of 0.64 ± 0.12 for N(6434)/N(6460). The difference of the energies of $26.1 \pm 2.0 \pm 0.2$ keV corresponds to the ground-state doublet spacing. The results of the fitting for the two-peak structure are summarized in Table 5.1. The variation in the fitting results with different background functions were included in the systematic errors.

We checked whether those fitting results reproduce the single-escape peaks in the Doppler-shift corrected spectrum. Figure 5.5 shows the "single-escape Doppler-shift

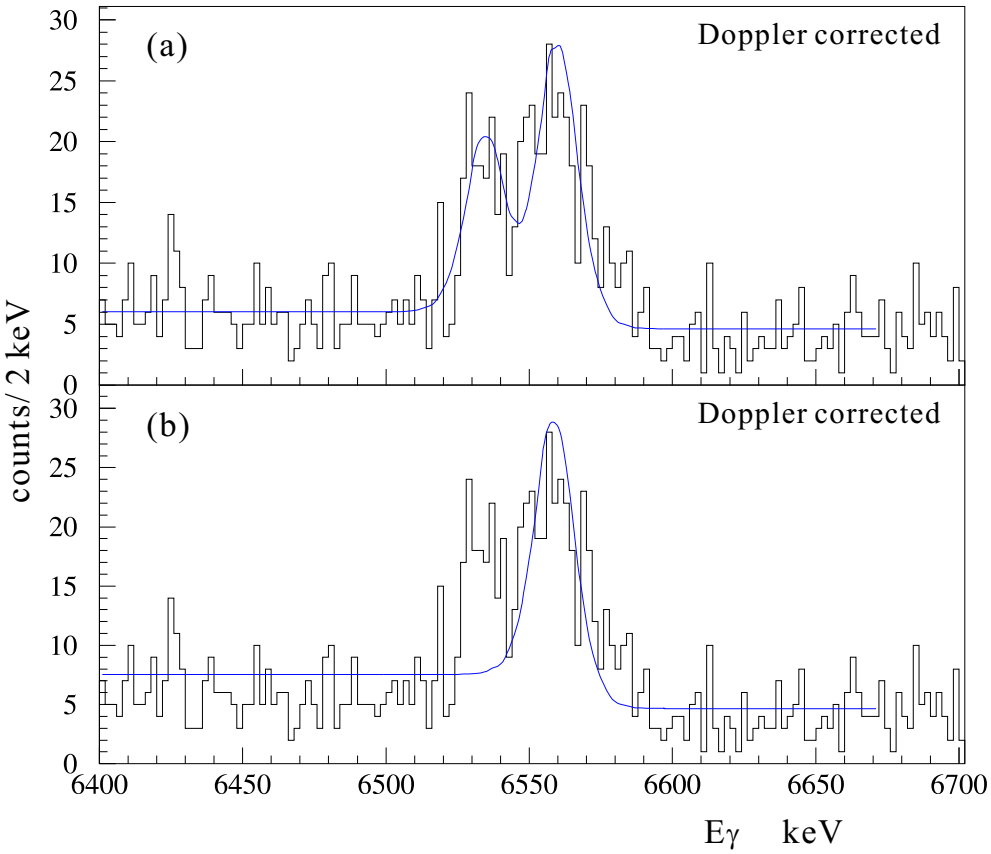

Figure 5.4: *Doppler-shift corrected γ-ray spectrum around the 6.55 MeV peak of ${}^{16}_{\Lambda}O$ with fitting result. (a) Fitting for the two-peak structure, (b) fitting for the single-peak structure. Simulated peak shape (see Sect.4.3) was used for the fitting. We used the "linear + peak combined linear " background function (see Fig .4.22).*

correction" spectrum with the expected peak shape in which we used the peak energies and count ratio of the fitting results but the total counts and the background were free parameters (two linear functions). "Single-escape Doppler-shift correction" was defined as,

$$E_\gamma^{SEcorrected} = \frac{1}{\sqrt{1-\beta^2}} \cdot (1 - \beta\cos\phi) \cdot (E_\gamma^{measured} + 511\mathrm{keV}).$$

As a result, these fitting results reproduce the single escape peak structures. And these results confirmed the two-peak structure.

5.1.2 Level assignment

We will assign spins of the levels from the γ-ray intensity ratio. First, the branching ratio R_{I_γ} between these two transitions is expected to be as follows,

$$R_{I_\gamma} = \frac{I_\gamma(1^- \to 1^-)}{I_\gamma(1^- \to 0^-)} = \begin{cases} 0.5 & \text{(weak coupling)} \\ 0.41 & \text{(level mixing)}, \end{cases} \tag{5.1}$$

where 0.5 is estimated in the limit of weak coupling between the core and Λ, and 0.41 is estimated with the level mixing taken into account [8]. Second, we have to consider the

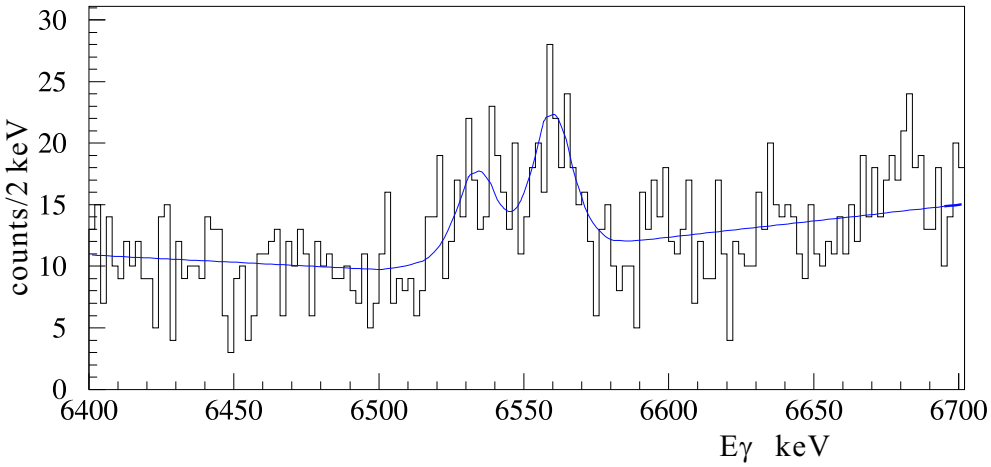

Figure 5.5: *"Single-escape peak" Doppler-shift corrected γ-ray spectrum*

difference of effective germanium efficiency between these transitions. In this reaction of ^{16}O $(K^-, \pi^-)^{16}_{\Lambda}$O with $\Delta L = 1, \Delta S = 0$, the emitted π^- and M1 γ ray have angular correlations as follows [41],

$$W(\theta_{\pi\gamma}) = \begin{cases} 1 + \cos\theta^2_{\pi\gamma} & (1^- \to 1^-) \\ 1 - \cos\theta^2_{\pi\gamma} & (1^- \to 0^-). \end{cases} \tag{5.2}$$

We performed a simulation using Eq.5.2 and the germanium detector crystal geometry, and obtained the relative effective germanium detector efficiency R_ε between these transitions as

$$R_\varepsilon = \frac{\varepsilon(1^- \to 1^-)}{\varepsilon(1^- \to 0^-)} = 0.80 \pm 0.02. \tag{5.3}$$

The systematic error comes from ambiguity of the real volume and the shape of the germanium crystals. Then we obtained the expected yield ratio of

$$\frac{Y(1^- \to 1^-)}{Y(1^- \to 0^-)} = R_{I_\gamma} \cdot R_\varepsilon = \begin{cases} 0.40 \pm 0.01 & \text{(weak coupling)} \\ 0.33 \pm 0.01 & \text{(level mixing).} \end{cases} \tag{5.4}$$

Comparing them with the experimental yield ratio of 0.64, we find that the upper level of the ground-state doublet is 1^- and the lower is 0^-. These results are summarized in Table 5.1 and Fig. 5.6.

Table 5.1: *Summary of $^{16}_{\Lambda}O$ γ rays*

transition	M1($1^- \to 1^-$)	M1($1^- \to 0^-$)
peak energy [keV]	6534.1 ± 1.5 ± 1.7	6560.2 ± 1.3 ± 1.7
$\Delta E_{g.s.}$ [keV]	26.1 ±2.0 ± 0.2	
yield [counts]	137 ± 18 ± 5	210 ± 30 ± 5
yield ratio $\frac{1^- \to 1^-}{1^- \to 0^-}$	0.64 ± 0.12	

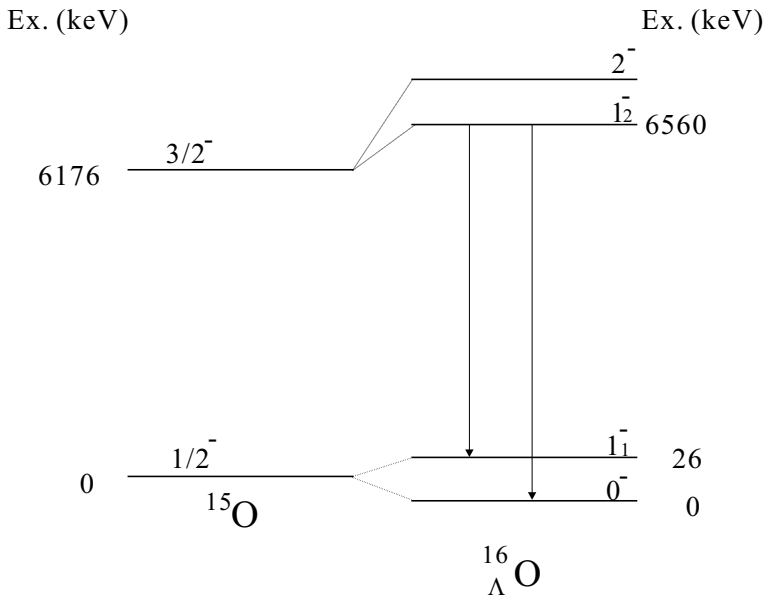

Figure 5.6: *Experimentally determined level scheme and excitation energies of* $^{16}_{\Lambda}O$

5.2 γ rays of $^{15}_{\Lambda}$N via proton emission

5.2.1 γ-ray energy and identification

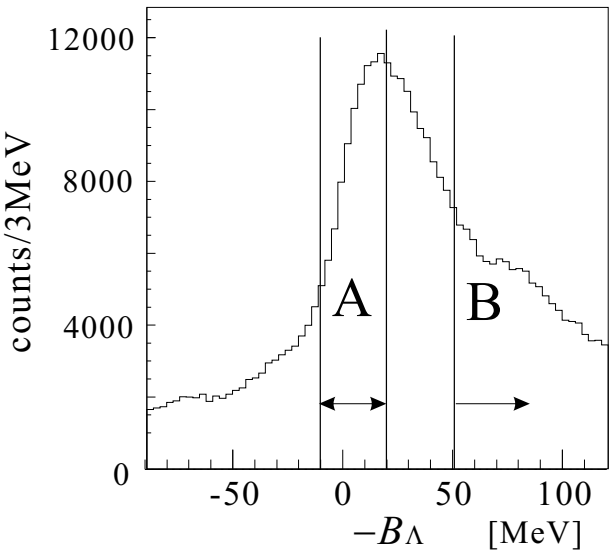

Figure 5.7: *Missing mass spectrum of $^{16}_{\Lambda}O$. The region "A"($-11 < -B_\Lambda < 19$ MeV) corresponds to the 17 MeV excited ($-B_\Lambda = 4$ MeV) substitutional state of $^{16}_{\Lambda}O$ and "B" ($-B_\Lambda > 50$ MeV) corresponds to the highly unbound region*

Figure 5.7 shows the mass spectrum of $^{16}_{\Lambda}$O plotted against $-B_\Lambda$ scale for those events which accompany γ rays from 1 to 5 MeV. The region "A" indicates the 17 MeV excited 0^+ state (+4 MeV in $-B_\Lambda$ scale) region of $^{16}_{\Lambda}$O (-11 $< -B_\Lambda <$ 19 MeV) and "B" ($-B_\Lambda >$ 50 MeV) corresponds to the highly unbound region. Figure 5.8 shows the mass-gated γ-ray energy spectra. (a) is for the 0^+ region ("A") without Doppler-shift correction, (b) is for the 0^+ region ("A") with Doppler-shift correction, and (c) is for the highly unbound region ("B") without Doppler-shift correction.

A narrow peak at 2270 keV, and two broad peaks at 1940 and 2460 keV which become narrow peaks after Doppler-shift correction, were observed when we selected the 0^+ region. There are no γ-ray transitions of non-strange A $\leq$ 16 nuclei corresponding to these energies and no excited states of $^{16}_{\Lambda}$O exist which emit γ rays around 2 MeV. Thus they are attributed to γ rays from hypernuclei. We assumed that they are γ rays of $^{15}_{\Lambda}$N. The assignment procedure will be discussed in the next section. We fitted the γ-ray peak at 2270 keV with a Gaussian function. From the fit, we obtained the peak energy of 2268.0 $\pm$ 0.5 $\pm$ 1.5 keV, a yield of 772 $\pm$ 39 counts and a fitting χ^2/DOF of 1.5. We also fitted the γ-ray peaks of 1960 keV and 2440 keV with the simulated Doppler-shift-corrected peak shape (see Fig. 4.20). Figure 5.9 shows the mass-gated γ-ray spectra around the peaks of $^{15}_{\Lambda}$N with the fitting results.

We obtain the energy of 1959.7 $\pm$ 1.6 $\pm$ 1.7 keV, a yield of 229 $\pm$ 41 counts and χ^2/DOF of 1.1 for the 1960 keV peak, For the 2442 keV peak, we obtained 2442.2 $\pm$ 1.4 $\pm$ 1.7 keV, 353 $\pm$ 35 and χ^2/DOF of 0.89 for 2442 keV peak. These results are summarized in Table 5.4

In Fig. 5.8 (a), a narrow γ-ray peak was observed at 2215 keV near the ^{27}Al$(n, n'\gamma)$ energy of 2211 keV. This peak appears to be narrow, while the γ-ray peak of ^{27}Al(2211 keV) for the highly unbound region in Fig 5.8 (c) is broadened. The peak in (a) seems

to be a different γ transition from the ^{27}Al γ ray, because the peak width and the peak center energy are different. We applied the prompt TDC cut (see Section4.4). Figure 5.10 shows the γ-ray spectra with the prompt (a) and the non-prompt cut (b). Comparing (a) with (b), the γ-ray at 2268 keV has almost the same yield in (a) and (b), while the γ-ray at about 2215 keV is clearly suppressed in the prompt spectrum (a). As a result, we attribute the 2215 keV peak to part of the broadened peak of the 2211 keV γ ray from ^{27}Al.

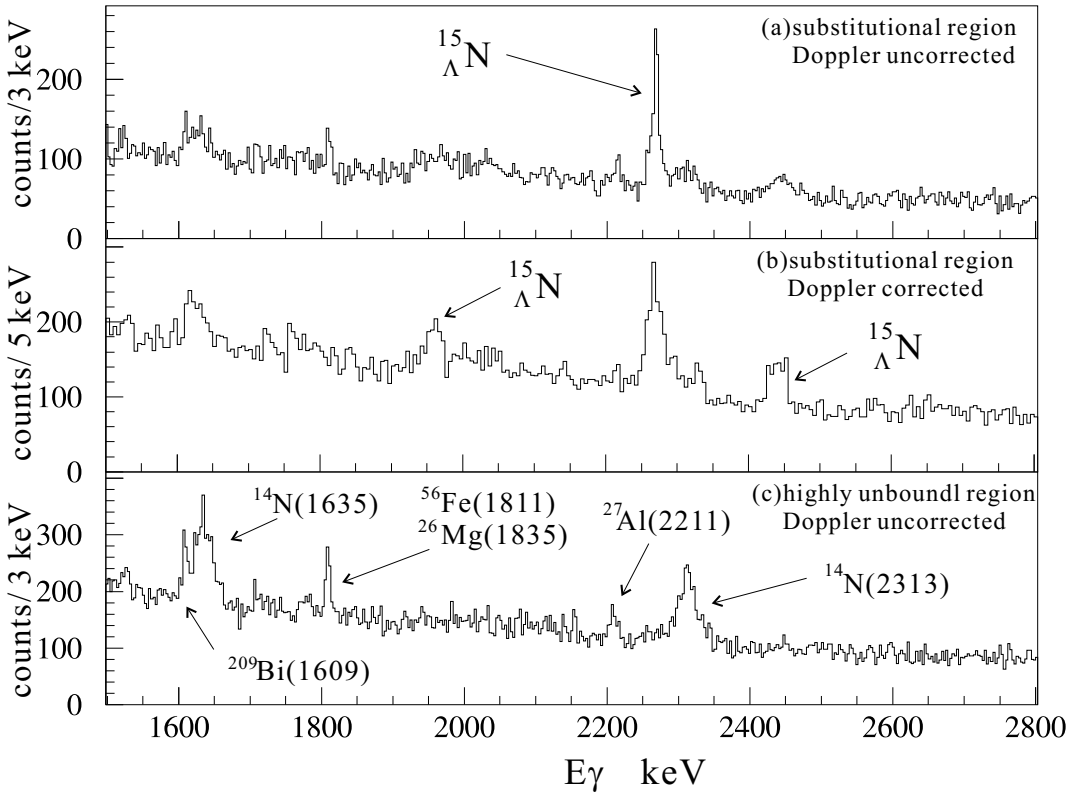

Figure 5.8: *Mass-gated γ-ray spectra around 2 MeV in the $^{16}O(K^-,\pi^-)$ reaction (a) is plotted for the 0^+ region ($-11 < -B_\Lambda < 19$ MeV) without Doppler correction, (b) is for the 0^+ region ($-11 < -B_\Lambda < 19$ MeV) with Doppler correction and (c) is for the highly unbound region ($-B_\Lambda > 50$ MeV) without Doppler correction,*

5.2.2 The excitation energy of $^{16}_{\Lambda}$O for decays into $^{15}_{\Lambda}$N

Figure 5.12 A-1, B-1 and C-1 show the γ-energy-gated mass distributions. The gated γ-ray energies are 2268 $\pm$ 16 keV for A-1, 2440 $\pm$ 16 keV for B and 1960 $\pm$ 16 keV for C. The γ-ray-energy gates are shown in Fig 5.11. We fitted the spectra for $-B_\Lambda >$ 40 MeV with the inclusive mass spectrum shape corresponding to Fig. 5.7. Solid lines in this figure are the fitting results and the dashed lines show the extrapolation from the fitting region. We plotted the difference between the γ- ray-gated spectra and the fitted inclusive spectra in Fig. 5.12 A-2, B-2 and C-2. We fitted the difference spectra with a Gaussian and obtained the mass of 5.2 ± 0.7, 6.1 ± 2.1 and 6.0 ± 1.3 MeV, and the peak width of 21.4 ± 1.7, 19.3 ± 5.9 and 17.6 ± 3.0 MeV (FWHM) for γ-ray gates on the the 2268 keV, the 1940 keV and the 2260 keV peaks, respectively. These results are summarized in Table 5.2 Thus we find that the dominant state which decays into

the excited state of ${}^{15}_{\Lambda}$N is the 17 MeV excited p-substitutional state of ${}^{16}_{\Lambda}$O. Even with consideration of the systematic error of 0.9 MeV, the peak mass seems slightly higher than the 17 MeV state ($-B_{\Lambda}$= 4 MeV), and the peak width which is larger than the resolution of 15 MeV suggests that more than one state may be decaying into ${}^{15}_{\Lambda}$N. We could not determine which other states contribute to the proton-emission channel due to our limited mass resolution.

To confirm that these γ-ray transitions are from ${}^{15}_{\Lambda}$N, we checked a possibility of other baryonic decay channels. The baryonic decay thresholds of ${}^{16}_{\Lambda}$O are summarized in Table 5.3 in the $-B_{\Lambda}$ scale. The three γ-ray transitions dominantly come from 17 MeV excited state of ${}^{16}_{\Lambda}$O, from which only ${}^{15}_{\Lambda}$N+p and ^{15}O+Λ channels are energetically possible when a daughter (hyper-)nuclei is excited over 2 MeV. There are no γ-ray transitions in ^{15}O at these observed energies. Therefore, these transitions are determined to be from ${}^{15}_{\Lambda}$N uniquely.

Table 5.2: *Fitting results of γ-energy-gated mass*

gated γ energy [keV]	peak mean energy ($-B_{\Lambda}$) [MeV]	peak width(FWHM) [MeV]	Figure
2268 ±16	5.2 ± 0.7	21.4 ± 1.7	A-2
1940 ±16	6.1 ± 2.1	19.3 ± 5.9	B-2
2260 ±16	6.0 ± 1.3	17.6 ± 3.0	C-2

Table 5.3: *Baryonic decay threshold of ${}^{16}_{\Lambda}O$*

decay channenl	threshold mass in $-B_{\Lambda}$ of ${}^{16}_{\Lambda}$O [MeV]	1st excitation energy of hyperfragment [MeV]
${}^{15}_{\Lambda}$N+p	-5	2.4 [8]
^{15}O+Λ	0	–
${}^{12}_{\Lambda}$C+α	2.3	2.4 [39]
${}^{13}_{\Lambda}$C+^{3}He	3.2	4.8 [16]

Table 5.4: *Summary of ${}^{15}_{\Lambda}N$ γ rays*

transition	M1($\frac{1}{2}^+$;T=1$\rightarrow \frac{3}{2}^+_1$)	M1(lower $\rightarrow \frac{1}{2}^+$;T=1)	M1(upper $\rightarrow \frac{1}{2}^+$;T=1)
energy	2268.0±0.5±1.5	1959.7± 1.6±1.7	2442.2±1.4±1.7
counts	772± 39	229 ± 41	353 ± 35

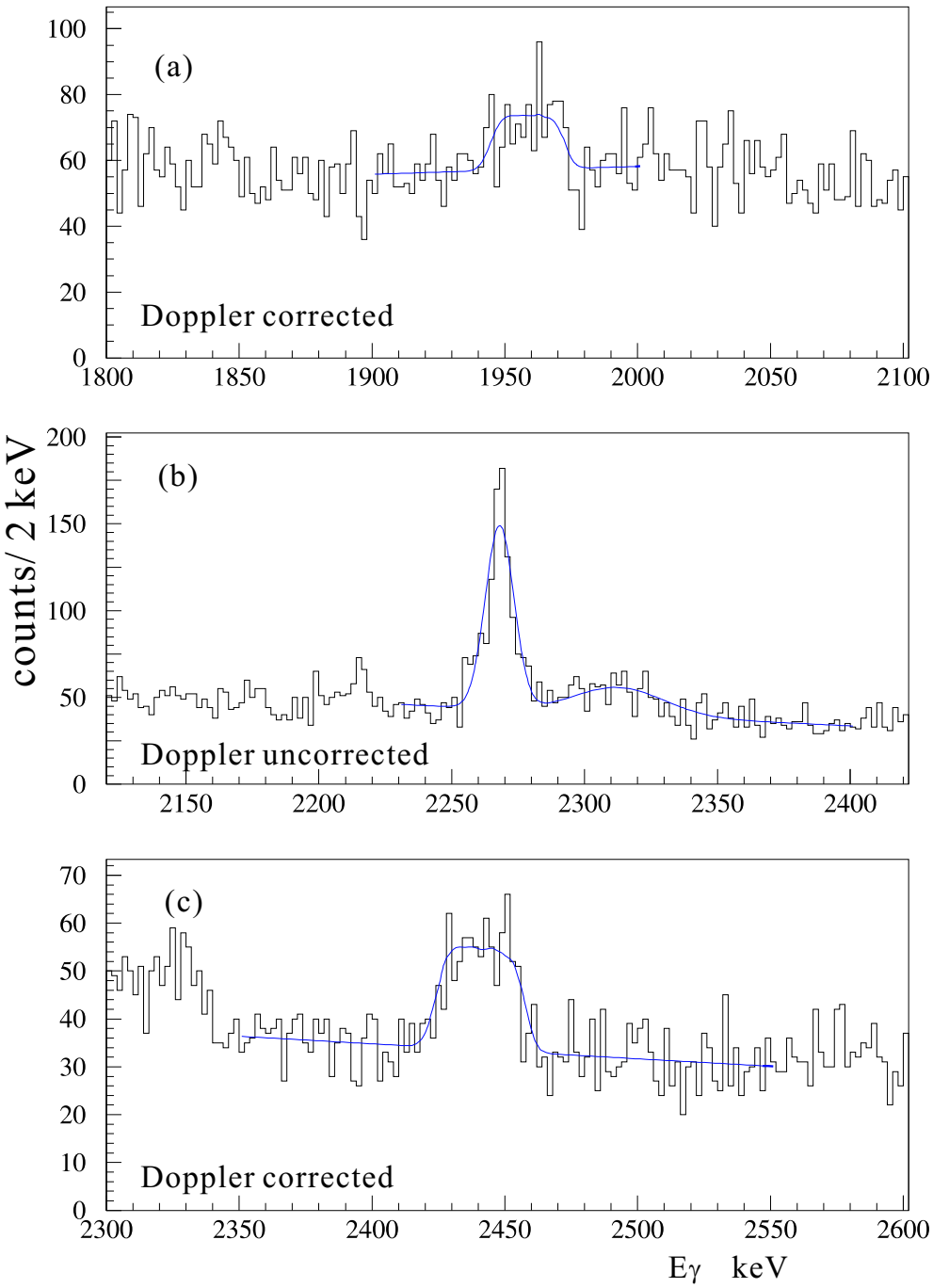

Figure 5.9: *Mass-gated γ-ray spectra around the peaks of ${}^{15}_{\Lambda}N$ with fitting results. All the spectra are plotted for the 0^+ region ("A"). (a) is with Doppler correction, (b) is without Doppler correction, and (c) is with Doppler correction. Fitting function for (a) and (c) are the simulated Doppler corrected peak shape and for (b) is a Gaussian function.*

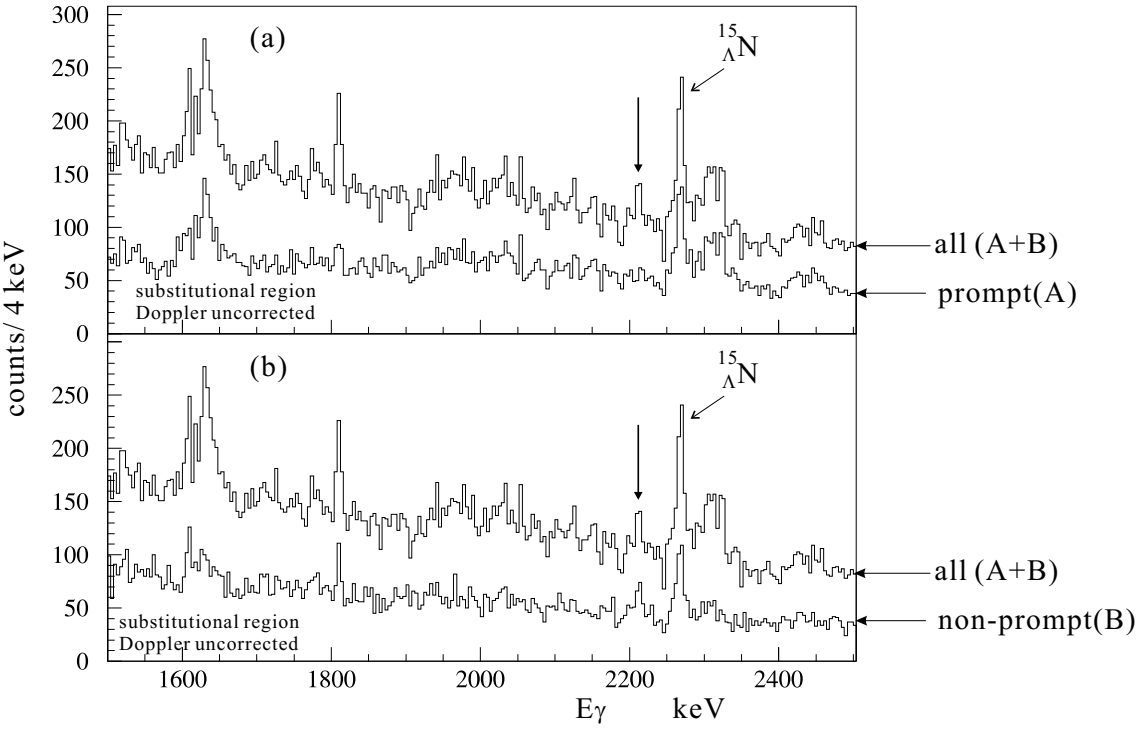

Figure 5.10: *Mass gated γ-ray spectra with the prompt and the non-prompt cut without Doppler-shift correction. The gated mass for (a) and (b) is the region of $-11 < -B_\Lambda <$ 19 MeV corresponding to the substitutional state of $^{16}_{\Lambda}O$. A and B are the TDC cut region defined in Section 4.4 (see Fig. 4.3).*

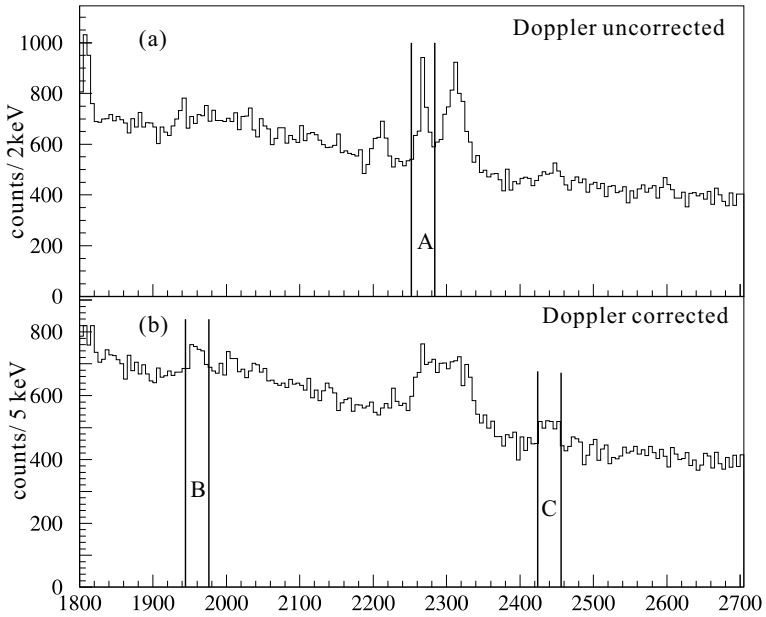

Figure 5.11: *Inclusive γ-ray spectra and γ energy gate. (a) is without Doppler-shift correction and (b) is with Doppler-shift correction.*

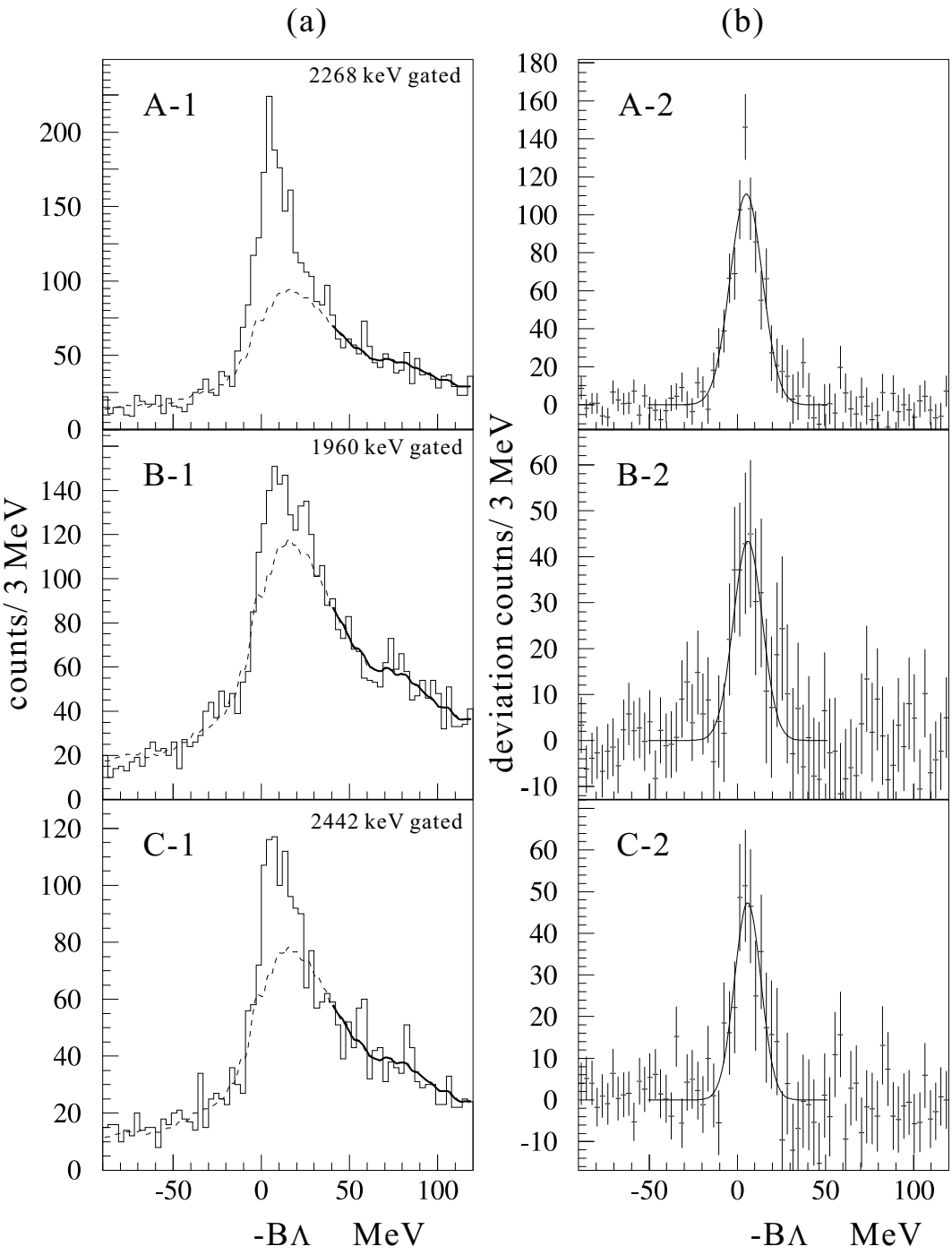

Figure 5.12: *(a) γ-energy-gated mass spectra.(b) The difference of the mass spectra of (a) from the background . "A", "B" and "C" correspond to the γ-energy gates in Fig.5.11. In (a), solid and dotted lines are contribution of the background, which was obtained by fitting the inclusive mass spectrum shape in the $-B_\Lambda > 40$ MeV region (shown by the solid line).*

5.2.3 Level assignment

First, we consider the assignment of γ-ray transitions based on their peak shape. As shown in Fig. 5.8 (a), the 2268 keV γ ray line is partly Doppler broadened. This means that the lifetime of the emitting state is of the same order as the stopping time in the target medium. The stopping time of ${}^{15}_{\Lambda}$N was calculated to be about 1 ps. Millener has suggested that because the ^{14}N ($0^+ \rightarrow 1^+$) M1 core transition is very weak (2.6×10^{-2} W.u., 68 fs), a small $1^+_2 \times s_\Lambda$ admixture in the wavefunctions of the members of the ground-state doublet can have a drastic effect on the strengths of the hypernuclear M1 transitions. He calculated a lifetime of 0.46 ps for the $\frac{1}{2}^+$;T=1 state (as shown in Fig. 1.7) and a branching ratio is expected to be 92:8 for $\frac{1}{2}^+$;T=1 $\rightarrow$ $\frac{3}{2_1}^+$ to $\frac{1}{2}^+$;T=1 $\rightarrow$ $\frac{1}{2_1}^+$. In the weak coupling limit, the branching ratio is expected to be 2:1 and the state is expected to have a lifetime of the same order as the core lifetime. The facts that the 2268 keV γ ray has a narrow peak structure and no other narrow peak corresponding to the partner transition is observed is consistent with the Millener's calculated result. The lifetimes of the other excited states of positive parity ${}^{15}_{\Lambda}$N states are expected to be less than 0.1 ps. Thus, the γ ray of 2268 keV is assigned as the M1 transition $\frac{1}{2}^+$;T=1$\rightarrow$ $\frac{3}{2_1}^+$.

Next, we consider the assignment of the 1960 keV and 2242 keV γ rays. They have Doppler broadened peak structures. The low-lying level energies of ${}^{15}_{\Lambda}$N are expected to be close to the excitation energies of ^{14}N, and in the weak coupling limit, the γ transitions of ${}^{15}_{\Lambda}$N are basically the same as those of ^{14}N. Figure 5.13 shows the low-lying levels and the relative intensities of γ transitions of ^{14}N. The most likely source of about 2 MeV γ rays are those related to from the 1^+, 3.95 MeV to 0^+;T=1,2.31 MeV core transition. The only other plausible source of γ rays with energies in the range from 2 MeV to 3 MeV is from the states based on the negative-parity levels of ^{14}N near 5 MeV to the $\frac{1}{2}^+$;T=1 state. We dismiss the latter possibility for the following reasons. If a ${}^{16}_{\Lambda}$O(0^+) decays to the negative parity state of ${}^{15}_{\Lambda}$N, ^{14}N(4.9 MeV 0^-)$\otimes s_\Lambda$, by p-wave proton emission, the γ rays of about 4.9 MeV corresponding to the transitions of $0^- \rightarrow 1^+$ are expected. However, a γ-ray energy of about 2.6 MeV corresponding to the transition of $0^- \rightarrow 0^+$ is strictly forbidden. If a ${}^{16}_{\Lambda}$O decays to the negative-parity state of ${}^{15}_{\Lambda}$N, ^{14}N(5.1 MeV 2^-)$\otimes s_\Lambda$, by p-wave proton emission, the γ ray of about 5.1 MeV, corresponding to the transition of $2^- \rightarrow 1^+$, and the γ ray of about 2.8 MeV, corresponding to the transition of $2^- \rightarrow 0^+$, are expected. However, the γ rays corresponding to these transitions would lead to narrow peaks because of the long lifetime (6.3 ps) of the 2^- core state.

Thus, these γ rays of about 2 MeV are not from the negative parity states, and therefore these γ rays are assigned to the M1 transitions from the upper-doublet states ($\frac{3}{2_2}^+$, $\frac{1}{2_2}^+$) to the $\frac{1}{2}^+$;T=1 state. It was suggested that the upper state of the upper doublet is expected to be $\frac{3}{2}^+$. Because the doublet spacing has a large contribution from the spin-spin force, the upper level is expected that core spin and Λ spin become parallel. At present we cannot assign the spin order of the upper doublet. The experimentally determined level scheme and the excitation energies of ${}^{15}_{\Lambda}$N are summarized in Fig. 5.14.

The s-wave and the d-wave proton emission processes are necessary to produce both of the upper doublet states from the p-substitutional state (0^+). If we take into account only penetrability of the Coulomb barrier in the transition rates, the d-wave emission is suppressed by the order of 10^3 from the s-wave emission. However, Gal pointed out that in the case in which the Λ is recoupled from p to s orbit, an angular momentum recoupling factor should be taken into account to the transition rates [42]. In that

paper, he calculated the transition rates from the 11 MeV excited state of ${}^{16}_{\Lambda}\mathrm{O}(0^+)$ to both ground-state doublet members of ${}^{15}_{\Lambda}\mathrm{N}(\frac{1}{2}^+_1, \frac{3}{2}^+_1)$ and suggested that the d-wave emission is dominant.

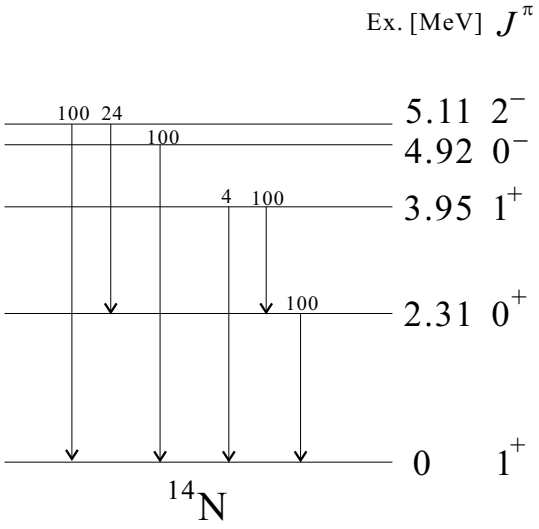

Figure 5.13: *Low-lying level scheme and relative γ-transition intensities of ^{14}N.*

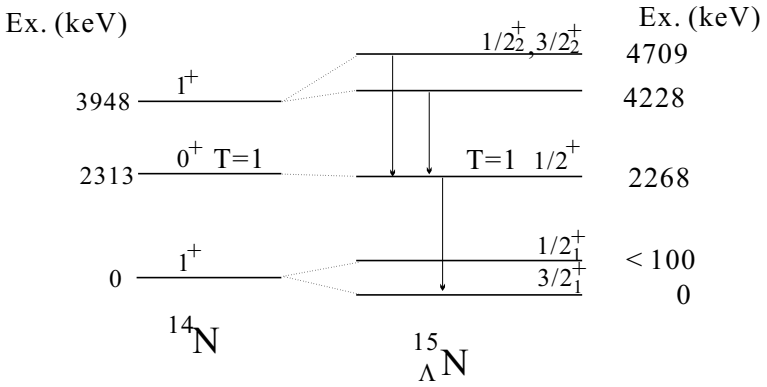

Figure 5.14: *Experimentally determined level scheme and excitation energies of ${}^{15}_{\Lambda}N$*

5.2.4 A search for the ground-state M1 transition

We could not measure the ground-state doublet spacing, because we did not observed the two M1 transitions from $\frac{1}{2}^+$;T=1 to both of the ground-state doublet members due to a possible small branching ratio of $\frac{1}{2}^+$;T=1 $\rightarrow \frac{1}{2}^+_1$. The ground-state doublet spacing $(E(\frac{1}{2}^+_1) - E(\frac{3}{2}^+_1))$ is expected to be -150 to 300 keV as discussed in Section 1.5.1 and the spin-flip M1 transition between the doublet members may be observed. Figure 5.15 shows the mass-gated γ-ray spectra without Doppler-shift correction. (a) is plotted for the 0^+ region ($-11 < -B_\Lambda < 19$ MeV) and (b) is for the highly unbound region ($-B_\Lambda > 50$ MeV). We searched for a peak in the region from 100 keV to 400 keV, but we could not find a prominent peak. The $\frac{1}{2}^+_1$ state is expected to be fed directly by proton emission, $I(\rightarrow \frac{1}{2}^+_1)/I(\rightarrow \frac{3}{2}^+_1) = 2/20$ from the 11 MeV excited 0^+ state and $I(\rightarrow \frac{1}{2}^+_1)/I(\rightarrow \frac{3}{2}^+_1) = 0/1$ from the 17 MeV excited 0^+ state [29]. We consider

the expected yield of the spin-flip M1 transition if $\frac{1}{2}^+_1$ could not be directly populated. The efficiency ratio is estimated to be roughly $\varepsilon_\gamma(100\ \mathrm{keV})/\varepsilon(2270\ \mathrm{keV}) \sim 4$ and $\varepsilon_\gamma(300\ \mathrm{keV})/\varepsilon(2270\ \mathrm{keV}) \sim 3$. When the upper level of the ground-stated doublet is $\frac{3}{2}^+$ and the spacing is 100 keV (300 keV), the expected γ-ray yield is $770 \times 4(3)$ counts, where 770 counts is the 2268 keV ${}^{15}_{\Lambda}\mathrm{N}(\frac{1}{2}^+;\mathrm{T}{=}1 \rightarrow \frac{3}{2}^+_1)$ γ-ray yield. When the upper level is $\frac{1}{2}^+$ and the spacing is 100 keV (300 keV), the expected γ-ray yield is $770 \times 8/92 \times 4(3) = 267(200)$ counts, where 8/92 is the expected branching ratio. Since the lifetime of the state is expected to be much longer than the stopping time, the γ-ray peak width is expected to be the same as the energy resolution of 3.5 keV(FWHM). A peak around 120 keV seems to be consistent, the γ-ray peak is not yet assigned but it is enhanced gating for s-substitutional region ($\sim$ 15 MeV). Therefore, it cannot be attributed to be a γ ray of ${}^{15}_{\Lambda}\mathrm{N}$. We did not find a corresponding γ-ray peak in the range from 100 keV to 400 keV. Hyperball is sensitive to the γ-ray energy down to 100 keV. Therefore, we obtained the upper limit on the energy spacing of 100 keV.

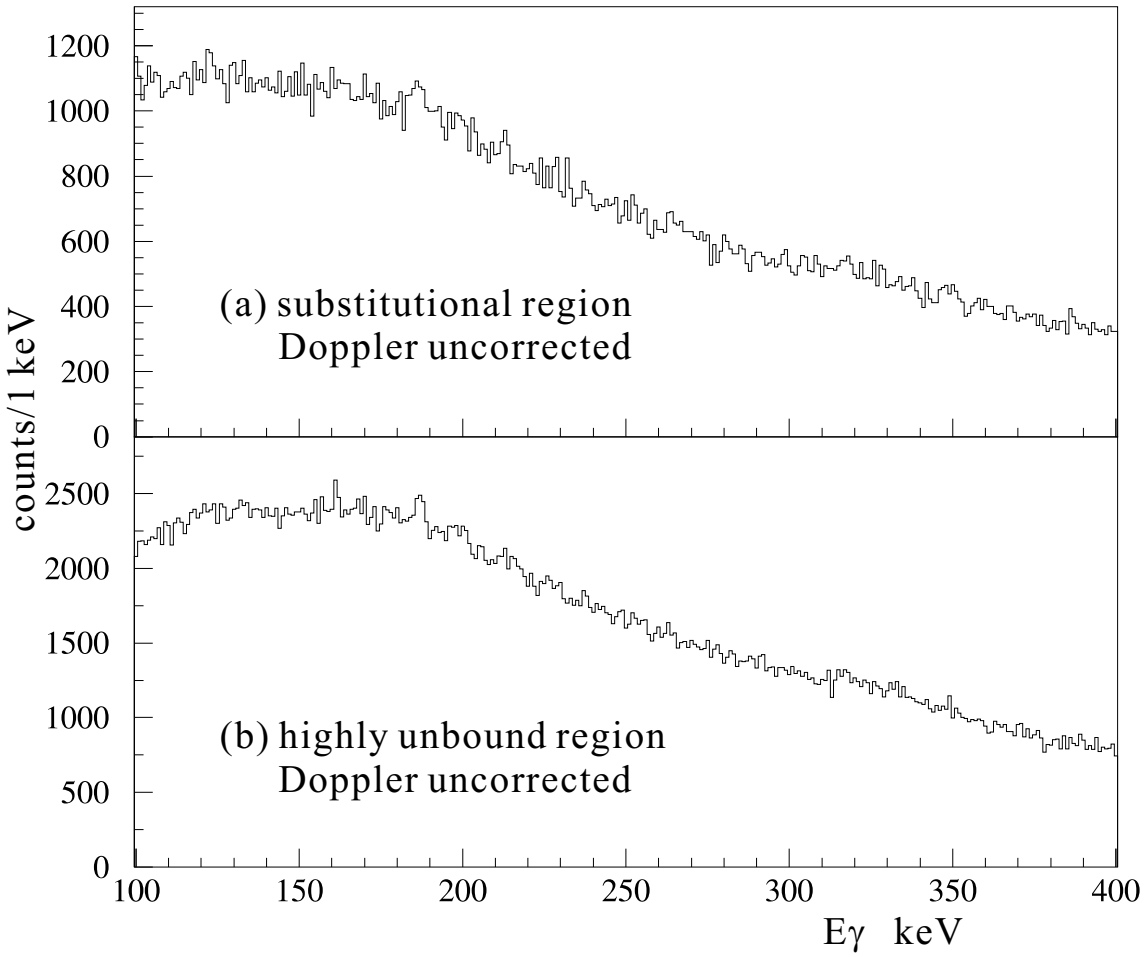

Figure 5.15: *Mass-gated γ-ray spectra around 200 keV in the ${}^{16}O(K^-,\pi^-)$ reaction without Doppler-shift correction. (a) is plotted for the 0^+ region ($-11 < -B_\Lambda < 19$ MeV) and (b) is for the highly unbound region ($-B_\Lambda > 50$ MeV).*

Chapter 6

Results from the ^{10}B$(K^-, \pi^-\gamma)$ Experiment

6.1 Search for the spin-flip M1 γ ray of $^{10}_{\Lambda}$B

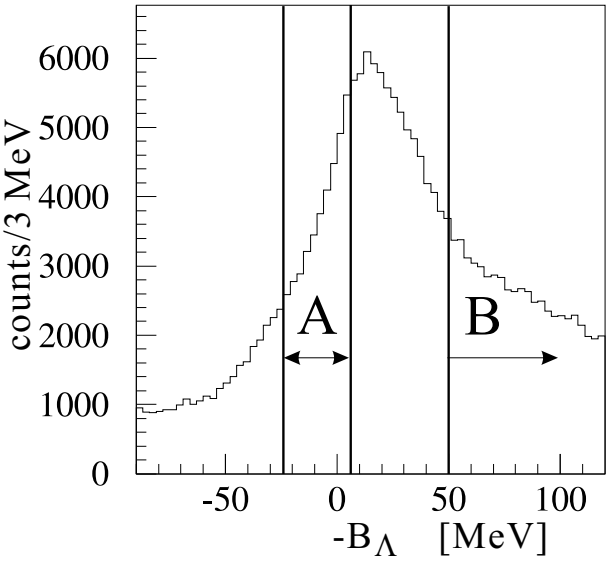

Figure 6.1: *Missing mass spectrum of $^{10}_{\Lambda}$B. "A" indicates the ground state region ($-23 < -B_\Lambda < 7$ MeV) and "B" indicates the highly unbound region ($-B_\Lambda > 50$ MeV).*

Figure 6.1 shows the mass spectrum of $^{10}_{\Lambda}$B plotted against $-B_\Lambda$. Figure 6.1 is plotted for those events which accompany γ-rays below 1 MeV. In this reaction, only the 2^- state of the ground-state doublet members can be produced. As shown in Table 3.2, the measured mass of the ground state of $^{10}_{\Lambda}$B corresponds to -8 MeV on the $-B_\Lambda$ scale. In Fig. 6.1, the region "A" ($-23 < -B_\Lambda < 7$ MeV) corresponds to the ground-state region of $^{10}_{\Lambda}$B, and "B" ($-B_\Lambda > 50$ MeV) corresponds to the highly unbound region. Figure 6.2 shows the mass-gated γ-ray spectra. (a) is plotted for the ground-state region ("A") without Doppler-shift correction, (b) is for the ground-state region with Doppler-shift correction and (c) is for the highly unbound region ("B") without Doppler-shift correction.

When the energy spacing of the spin-doublet states is $E(2^-) - E(1^-) = \Delta E$ [MeV], the spin-flip M1 transition rate[1] of the 2^- state is estimated to be

$$\Gamma_\gamma(2^- \to 1^-, \Delta E) = 1.68 \times \Delta E^3 \times 10^{13} \quad \mathrm{sec}^{-1}$$

in zero-order approximation[2]. On the other hand, the stopping time of ${}^{10}_{\Lambda}$B is expected to be about 1 ps. If the spacing is larger than 0.5 MeV, the γ-ray energy is Doppler broadened. We searched for both Doppler-shift uncorrected and Doppler-shift corrected γ-ray spectra in the range from 100 keV to 600 keV, but we could not find any γ-ray peaks corresponding to the ${}^{10}_{\Lambda}$B ($2^- \to 1^-$) M1 transition. As described later (Section 6.4), the detector sensitivity to the γ ray is expected to be large enough to see it if the energy is greater than 100 keV. Consequently, we concluded that the upper limit to the doublet spacing is 100 keV. The result is consistent with the result of a past experiment with germanium detectors [11]. Figure 6.3 shows the experimentally determined level scheme of ${}^{10}_{\Lambda}$B.

[1]When both initial and final hypernuclear state are the members of the spin-doublet states (J_i, J_f) having a spacing of ΔE, the spin-flip M1 rate is expressed by [43]

$$\Gamma_\gamma(J_i \to J_f, \Delta E) = \alpha_1(\Delta E)(2J_f + 1) \left\{ \begin{array}{ccc} J_i & J_f & 1 \\ \frac{1}{2} & \frac{1}{2} & J_N \end{array} \right\}^2 (\mathrm{g}_N - \mathrm{g}_\Lambda)^2,$$

where g_N and g_Λ are the effective g-factor of core nucleus and Λ, respectively, J_N is spin of core nucleus and $\alpha_1 = 4.2 \times 10^{12}$ sec^{-1} MeV^{-3}.

[2]g-factor of the core nucleus and Λ, g_N and g_Λ are taken from the magnetic moments for the core nuclear state and for the free Λ. In this case $\mathrm{g}_N = 1.99$ for ^{9}B (calculated value)[43], and $\mathrm{g}_\Lambda = -1.226$ for Λ are used.

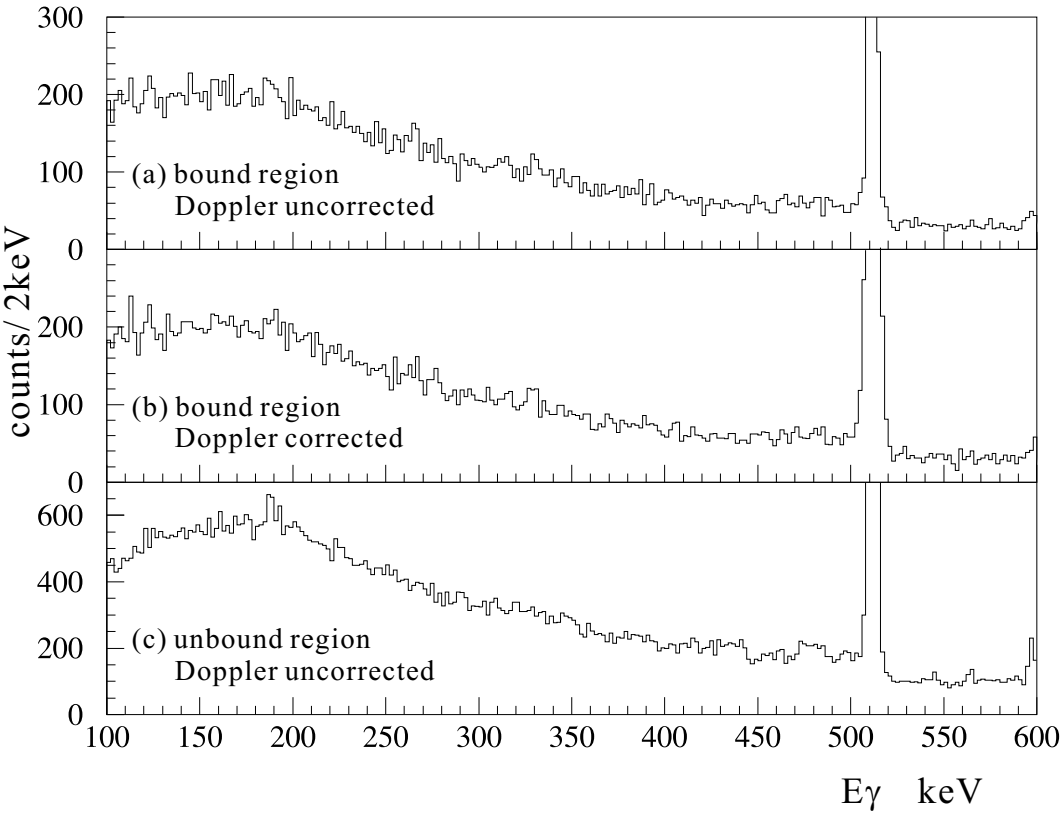

Figure 6.2: *Mass-gated γ-ray spectra around 200 keV in the ^{10}B $(K^-, \pi^-\gamma)$ reaction. (a) is plotted for the ground-state region without Doppler-shift correction, (b) is for the ground-state region with Doppler-shift correction and (c) is for the unbound region without Doppler-shift correction.*

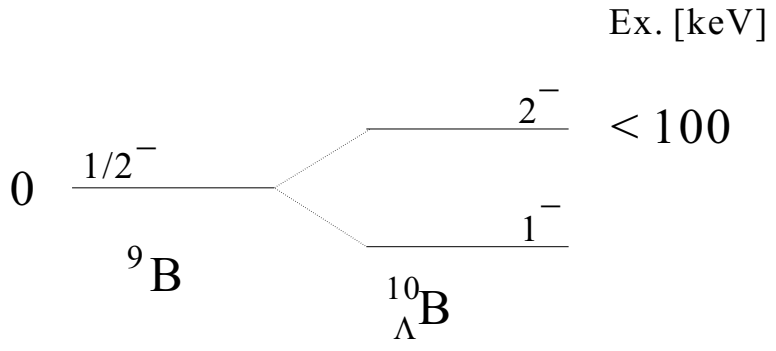

Figure 6.3: *Experimentally determined level scheme of $^{10}_{\Lambda}B$*

6.2 The observed γ ray of ${}^{9}_{\Lambda}$Be via proton emission

6.2.1 The E2 transition

The ${}^{9}_{\Lambda}$Be E2 transitions from the excited-doublet states ($\frac{3}{2}^{+}, \frac{5}{2}^{+}$) to the ground state ($\frac{1}{2}^{+}$) were observed in the old experiment using NaI counters[14] and the previous Hyperball experiment (E930('98))[12] via the (K^{-}, π^{-}) reaction. We observed γ-ray peaks at around 3050 keV in the Doppler-shift corrected spectrum when we selected the mass of ${}^{10}_{\Lambda}$B around $-B_{\Lambda}\sim$ 10 MeV. These γ-ray energies agree with the energies of 3024 $\pm$ 4 keV and 3067 $\pm$ 4 keV for the E2 transitions of ${}^{9}_{\Lambda}$Be in E930('98). In that experiment, the order of the levels ($\frac{5}{2}^{+}, \frac{3}{2}^{+}$) of the doublet was not determined.

We plotted the γ-ray-energy-gated mass spectrum in Fig. 6.4 for the Doppler-shift-corrected γ-ray energy from 3010 keV to 3100 keV and we find that the mass region of $-18 < -B_{\Lambda} < 28$ MeV is enhanced. The mass distribution suggests the existence of a number of states which decay into the excited states of ${}^{9}_{\Lambda}$Be. The mass of the lowest state is expected to correspond to about $-B_{\Lambda} = -3$ MeV because the mass distribution is rising at -18 MeV and the mass resolution is 15 MeV (FWHM). The mass of about -3 MeV corresponds to the 3^{-} and 4^{-} states at $-B_{\Lambda} = -2.3$ MeV and -1 MeV in Fig 1.8. The masses of the highest states are expected to be about +9 MeV. This energy is consistent with those expected for the p-substitutional states.

Figure 6.5 shows the mass-gated γ-ray spectra; (a) is the spectrum plotted for $-18 < -B_{\Lambda} < 28$ MeV without Doppler-shift correction, (b) is for $-18 < -B_{\Lambda} < 28$ MeV with Doppler-shift correction and (c) is for $-B_{\Lambda} > 50$ MeV without Doppler-shift correction. The previous experiment (E930('98)) also reported that these excited states of ${}^{9}_{\Lambda}$Be ($\frac{3}{2}^{+}$ and $\frac{5}{2}^{+}$) have lifetimes less than 0.1 ps. The γ-ray of ${}^{9}_{\Lambda}$Be following proton emission from ${}^{10}_{\Lambda}$B is expected to make a broad peak which becomes narrower or two peaks after Doppler-shift correction. Thus we fitted the Doppler-shift corrected spectrum with the simulated peak shape. Here, the peak energies were fixed at 3024 keV and 3067 keV. We used the three types of background, as discussed in Sect. 4.4. Figure 6.6 shows the fitting results, in which the fitted counts varied with the different background shapes. (a) shows the fitting with a linear background, (corresponding to Fig. 4.22 (a)), (b) shows the fitting with a liner and a combined-linear background (Fig. 4.22 (b)). In addition a γ ray peak of 3004 keV from ^{27}Al exists below those peaks, but it was not included for the background. The peaks are fitted with simulated peak shape (see Fig. 4.21) and the peak energies are fixed at 3024 keV and 3067 keV. As a result, we obtained the yield of 127 $\pm$ 18 $^{+15}_{-3}$ counts for 3067 keV and 34 $\pm$ 19 $^{+10}_{-13}$ counts for 3024 keV, which corresponds to the ratio of 0.27 $\pm$ 0.13 $^{+0.08}_{-0.10}$ for N(3024)/N(3067), and χ^2/DOF of 1.30 for (a), 1.31 for (b), and 1.33 for (c). The larger yield of the higher energy γ ray indicates that upper level of the ($\frac{5}{2}^{+}, \frac{3}{2}^{+}$) spin-doublet states is favored by proton emission from ${}^{10}_{\Lambda}$B.

These results are summarized in Table. 6.2.

6.2.2 Spin assignment

We can assign the spins of the levels in the excited-state doublet of ${}^{9}_{\Lambda}$Be from the γ-ray intensity ratio. Millener used a shell-model calculation to calculate the proton emission from states of ${}^{10}_{\Lambda}$B formed via the (K^{-}, π^{-}) reaction to states of the core-excited doublet of ${}^{9}_{\Lambda}$Be. Table. 6.1 shows the results of his calculation. The result of the calculation

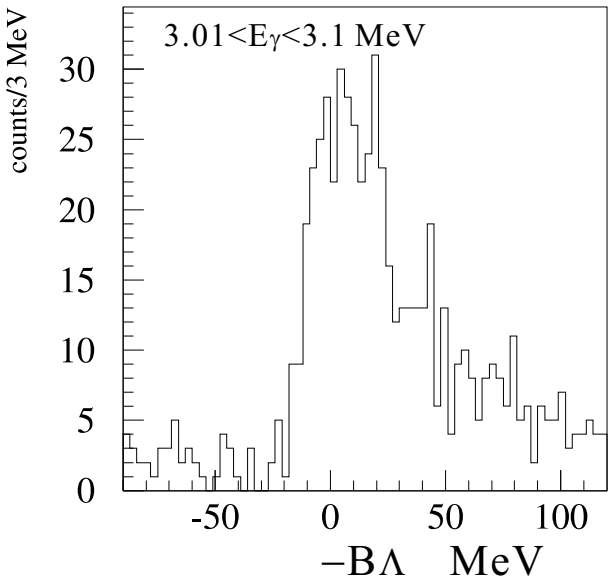

Figure 6.4: *γ-energy-gated mass spectrum of ${}^{10}_{\Lambda}B$, plotted for the Doppler-shift corrected γ-ray energy in the range from 3010 keV to 3100 keV.*

suggested that the $\frac{3}{2}^+$ state of ${}^{9}_{\Lambda}$Be is more strongly favored by proton emission than the $\frac{5}{2}^+$ state of ${}^{9}_{\Lambda}$Be; the calculated production ratio ($\frac{3}{2}^+/\frac{5}{2}^+$) is 1 : 0.29. However, he did not take into account the contribution of the $p_n^{-1}p_\Lambda$ states at $-B_\Lambda \sim 9$ MeV. We fitted the γ-ray spectrum plotted for $-18 < -B_\Lambda < 0$ MeV in which the states with $-B_\Lambda = -2 \sim 2$ MeV are dominantly included. And we obtained the ratio of 0.20 ± 0.09 for N(3067)/N(3024) for those states region. For those states, the Millener's calculation gives the ratio of 0.29. Comparing it with the experimental yield ratio of $0.27 \pm 0.13^{+0.08}_{-0.10}$ for $-18 < -B_\Lambda < 28$ MeV and 0.20 ± 0.09 for $-18 < -B_\Lambda < 0$ MeV, we concluded that the $\frac{3}{2}^+$ state is the upper state of the doublet. As described after in Section 7.3, this spin order confirmed a negative value of S_Λ the same sign as the ${}^{13}_{\Lambda}$C data ($\frac{1}{2}^-, \frac{3}{2}^-$) reported[47].

Table 6.1: *Decay properties of ${}^{10}_{\Lambda}B$ excited states into ${}^{9}_{\Lambda}Be + p$ calculated by Millener [8, 27]*

${}^{10}_{\Lambda}$B state	mass in $-B_\Lambda$ [MeV] (expected)	core state	formation strength	$\rightarrow {}^{9}_{\Lambda}Be(3/2^+)$	$\rightarrow {}^{9}_{\Lambda}Be(5/2^+)$
2^-	-8.7	$3/2^-$	0.292	0.	0.
3^-	-2.4	$7/2^-$	0.099	0.091	0.009
4^-	-2.2	$7/2^-$	0.061	0.	0.061
3^-	-1.7	$5/2^-$	0.020	0.	0.020
3^-	0.9	$7/2^-$	0.530	0.485	0.045
4^-	2.2	$7/2^-$	0.031	0.	0.031
overall				0.576	0.166

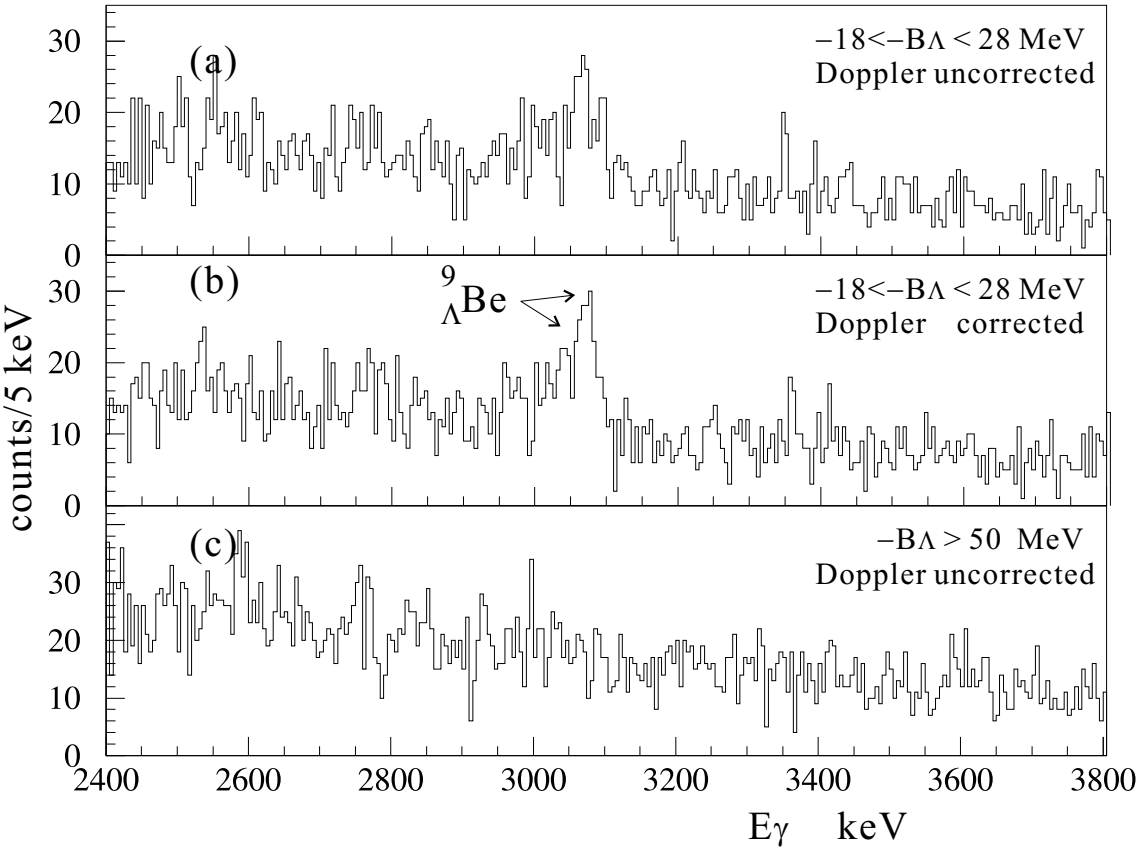

Figure 6.5: *Mass-gated γ-ray spectra in the ^{10}B $(K^-, \pi^-\gamma)$ reaction. (a) is plotted for $-18 < -B_\Lambda < 28$ MeV without Doppler-shift correction, (b) is for $-18 < -B_\Lambda < 28$ MeV with Doppler-shift correction and (c) is for $-B_\Lambda > 50$ MeV without Doppler-shift correction.*

Table 6.2: *Summary of $^{9}_{\Lambda}Be$ γ rays*

transition	E2($\frac{3}{2}^+ \rightarrow \frac{1}{2}^+$)	E2($\frac{5}{2}^+ \rightarrow \frac{1}{2}^+$)
energy [keV]	3067 (fixed)	3024 (fixed)
yield [counts]	$127 \pm 18^{+15}_{-3}$	$34 \pm 19^{+10}_{-13}$
ratio N(3024)/N(3067)	$0.27 \pm 0.13^{+0.08}_{-0.10}$	

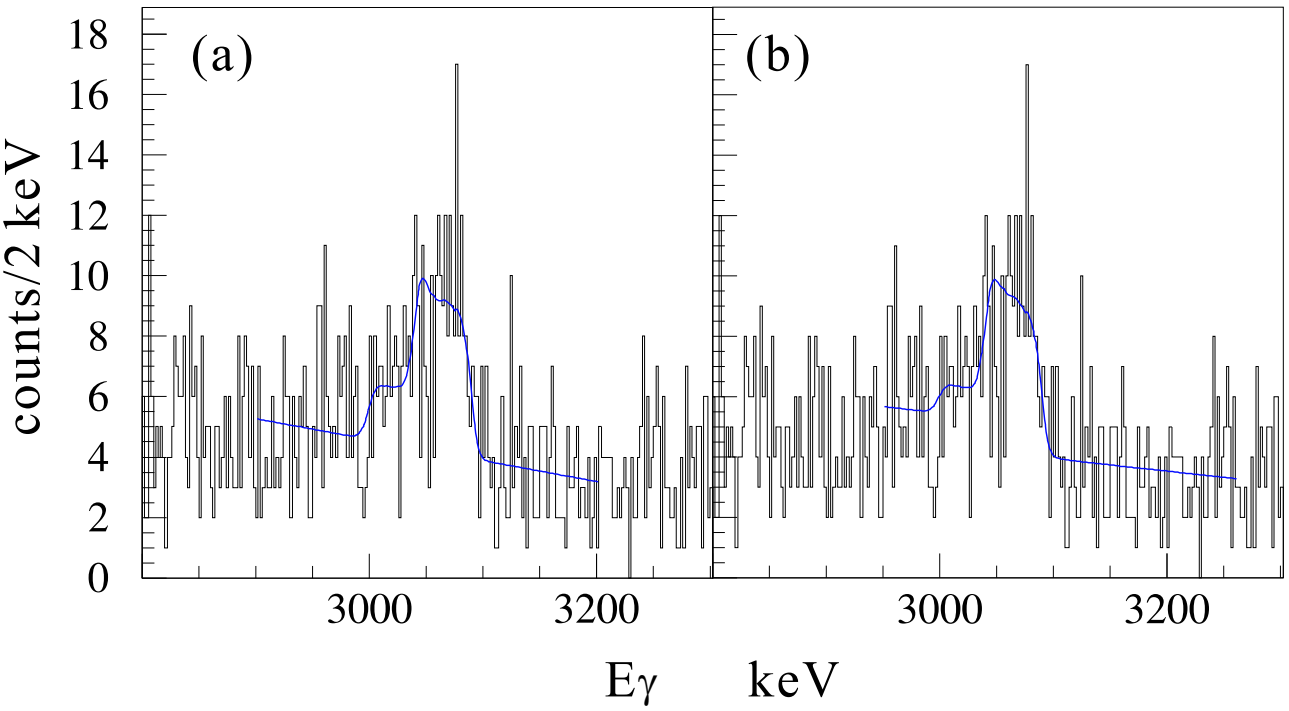

Figure 6.6: *γ-ray spectrum around the peak of ${}^{9}_{\Lambda}$Be with the fitting (a) is the fitting with a linear background (corresponding to Fig. 4.22 (a)), (b) is the fitting with a liner and a combined-linear background (Fig. 4.22 (b)). The peaks are fitted with simulated peak shape and the peak energies are fixed at 3024 keV and 3067 keV.*

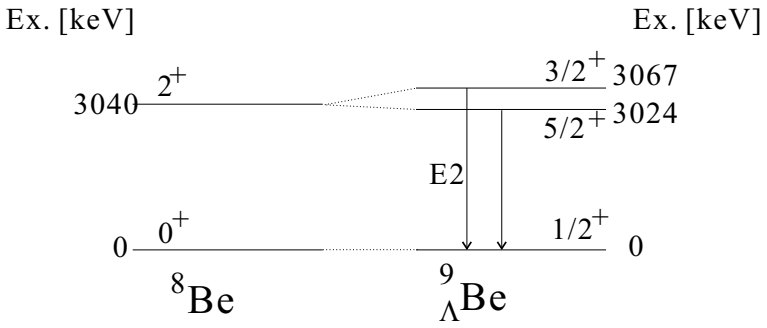

Figure 6.7: *Experimentally determined level scheme of ${}^{9}_{\Lambda}$Be*

6.3 The observed γ rays of ${}^{7}_{\Lambda}$Li via ^{3}He emission

6.3.1 The E2 transition and the spin-flip M1 transition

Since the ground state of ^{10}B has spin of 3^+, it is possible that the highly-excited substitutional state of ${}^{10}_{\Lambda}$B corresponding to the configuration of $[(s_{1/2})_n^{-1}(s_{1/2})_\Lambda]_{3^+}$ decays into the large spin states of ${}^{7}_{\Lambda}$Li ($\frac{5}{2}^+$ and $\frac{7}{2}^+$) via $l = 0$ ^{3}He emission. This substitutional ${}^{10}_{\Lambda}$B state is expected to have a mass of about 20 MeV in $-B_\Lambda$ and a broad width. We defined the mass gate of $0 < -B_\Lambda < 40$ MeV for this state. Figure 6.8 and Fig. 6.9 are the mass-gated γ-ray spectra without Doppler-shift correction. Both (a) are plotted for the s-substitutional region and both (b) are for the highly unbound region. We observe the two γ-rays from ${}^{7}_{\Lambda}$Li with energies of 2050 keV and 692 keV. They were observed in the previous experiment with Hyperball (KEK E419) [9, 15, 10] and already assigned as the E2 transition ($\frac{5}{2}^+ \rightarrow \frac{1}{2}^+$) and the ground state spin-flip M1 transition ($\frac{3}{2}^+ \rightarrow \frac{1}{2}^+$). We fitted them with a Gaussian function and obtained energies of 691.5 $\pm$ 0.6 (stat.) $\pm$ 0.6 (syst.) keV and 2050.1 $\pm$ 0.4 (stat.)$\pm$ 0.6 (syst.), and the yield of 170 $\pm$ 26 counts and 105 $\pm$ 14 counts. Figure 6.10 (a) and (b) show the γ-ray spectra around the peaks with fitting results. Figure 6.11 shows the γ-ray-energy-gated mass spectrum. (a) is plotted for the γ-ray energy in the range from 687 keV to 697 keV. (b) is for the energy in the range from 2042 keV to 2058 keV. The 10 keV gate for the 692 keV γ ray is set to maximize the S/N ratio. The 16 keV gate width for the 2050 keV γ ray is set to cover all the peak events. The γ-ray-gated mass spectra seem to have some yields above 40 MeV up to 100 MeV. Then we fitted the γ-ray spectra gated for the mass of the range from 0 MeV to 100 MeV and obtained the yields of 201 $\pm$ 34 counts for the 692 keV γ ray and of 132 $\pm$ 18 counts for the 2050 keV γ ray. It is implied that there exist some states contributing to these ${}^{7}_{\Lambda}$Li γ rays above the $s^{-1}s_\Lambda$ state. These results are summarized in Table 6.3.

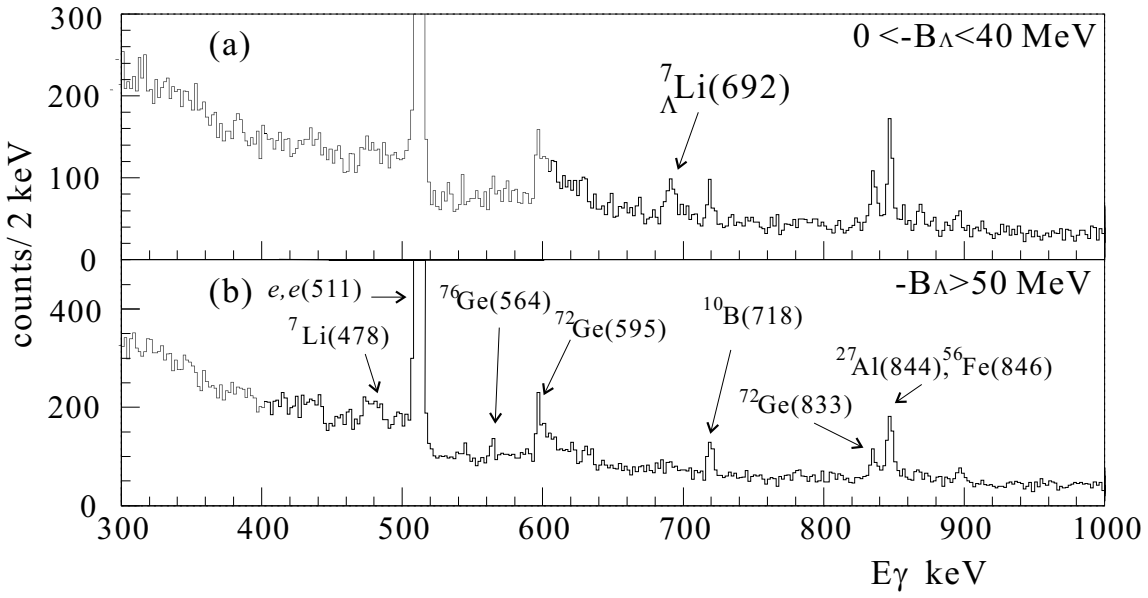

Figure 6.8: *Mass-gated γ-ray spectra around 700 keV in the ${}^{10}B$ (K^-, π^-) reaction. (a) is for $0 < -B_\Lambda < 40$ MeV corresponding to the $s^{-1}s_\Lambda$ state of ${}^{10}_{\Lambda}B$, and (b) is for $-B_\Lambda > 50$ MeV corresponding to the highly unbound state. In both spectra, Doppler shift is not corrected.*

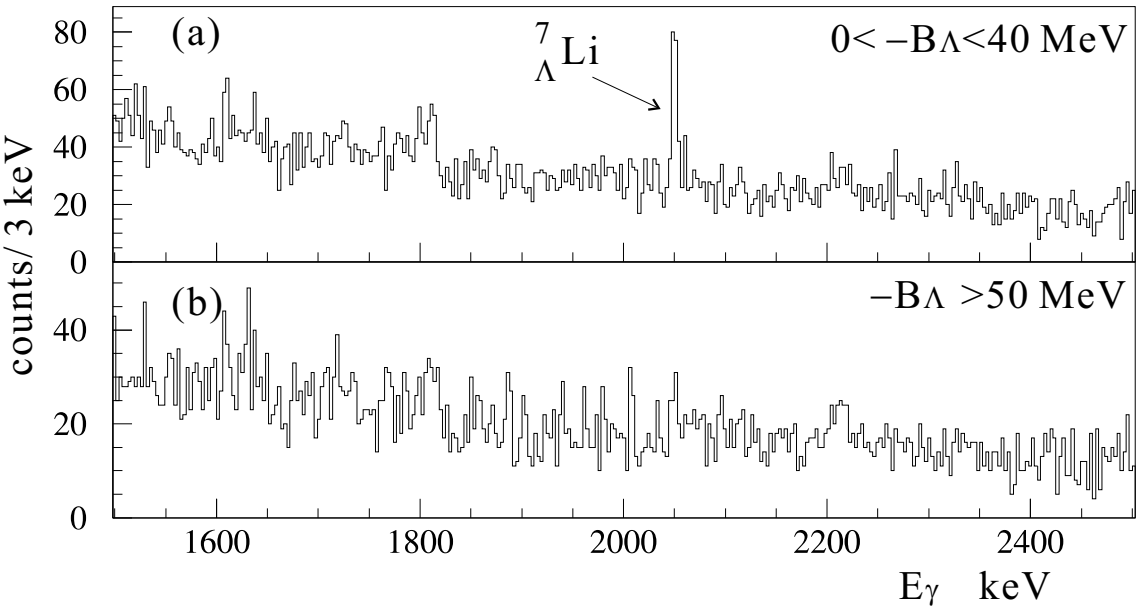

Figure 6.9: *Mass-gated γ-ray spectra around 2 MeV in the ^{10}B (K^-, π^-) reaction. (a) is for $0 < -B_\Lambda < 40$ MeV corresponding to the $s^{-1}s_\Lambda$ state of $^{10}_{\Lambda}B$, (b) is for $-B_\Lambda > 50$ MeV corresponding to the highly unbound states. In both spectra, Doppler shift is not corrected.*

6.3.2 Search for the other M1 transitions

Figure 6.12 shows the mass-gated γ-ray spectra around 3.5 MeV. Both (a) and (b) are plotted for the *s*-substitutional state region, and (a) is Doppler-shift uncorrected and (b) is Doppler-shift corrected. We could not find the M1 transitions of $^{7}_{\Lambda}$Li from the $\frac{1}{2}^+$;T=1 at 3.88 MeV to the ground-state doublet with the energies of 3877 keV and 3186 keV. These γ rays were previously observed in E419. The germanium detector efficiency ratio for 692 keV and 3186 keV γ rays is roughly 4:1. Therefore, if we assume that the $\frac{3}{2}^+$ state in the ground-state doublet is always produced via the γ transitions from the $\frac{1}{2}^+$;T=1 state at 3.88 MeV, the expected yield if 3186 keV γ ray is roughly 50 counts. In reality, the $\frac{3}{2}^+$ state was expected to be produced mainly or partly by baryonic decay from $^{10}_{\Lambda}$B directly. So the expected yield of 3186 γ ray is less than 50 counts. In addition, the expected lifetime of the $\frac{1}{2}^+$;T=1 state is of the order of 0.1 fs and thus the γ-ray energies are Doppler shifted. We also estimated the Doppler-shift correction power by a simulation in which the A = 10 nucleus divides the recoil momentum into A = 3 and A = 7 nuclei. The simulation showed that the correction power was not good enough. The Doppler-shifted peak width was about 57 keV in σ and the corrected peak width was about 52 keV in σ. Therefore, the non-observation of the M1 transitions from $\frac{1}{2}^+$ (3.88 MeV) to the ground-state doublet is reasonable.

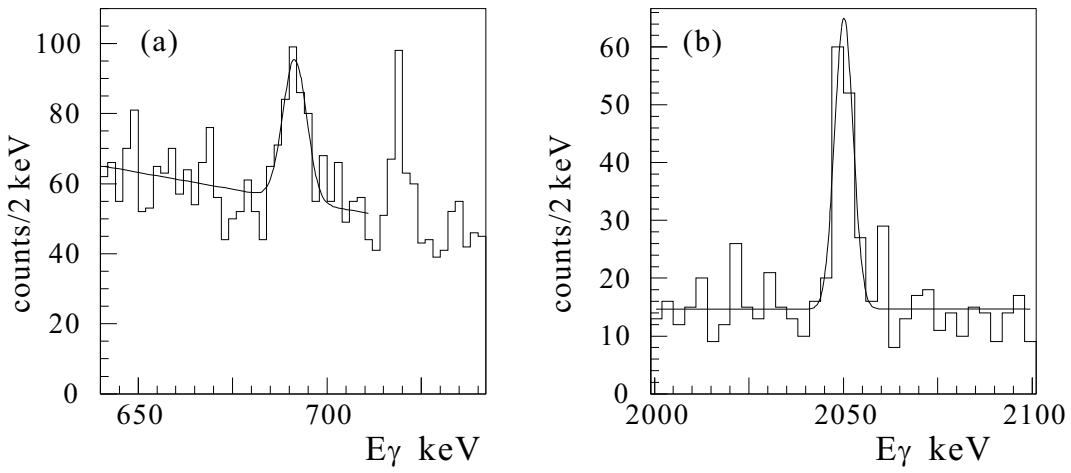

Figure 6.10: *Mass-gated γ-ray spectra around the γ-ray peaks of ${}^{7}_{\Lambda}Li$ with fitting results. (a) is around the ground-state M1 transition peak, and (b) is around the E2 transition peak. Each spectrum, the result of the fitting with a Gaussian and a linear background is shown in the solid line.*

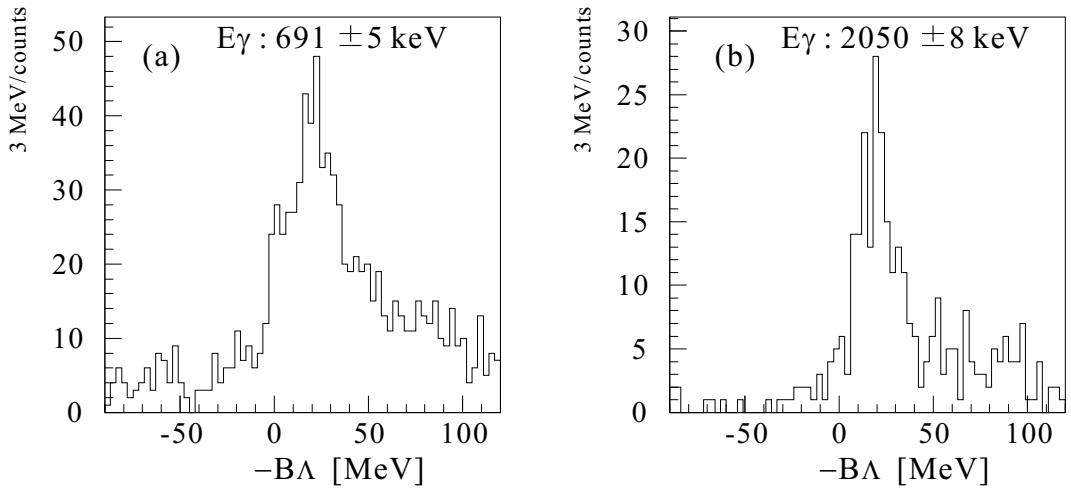

Figure 6.11: *γ-energy-gated mass spectra of ${}^{10}_{\Lambda}B$. (a) is gated for the ground state M1 transition and (b) is for the E2 transition.*

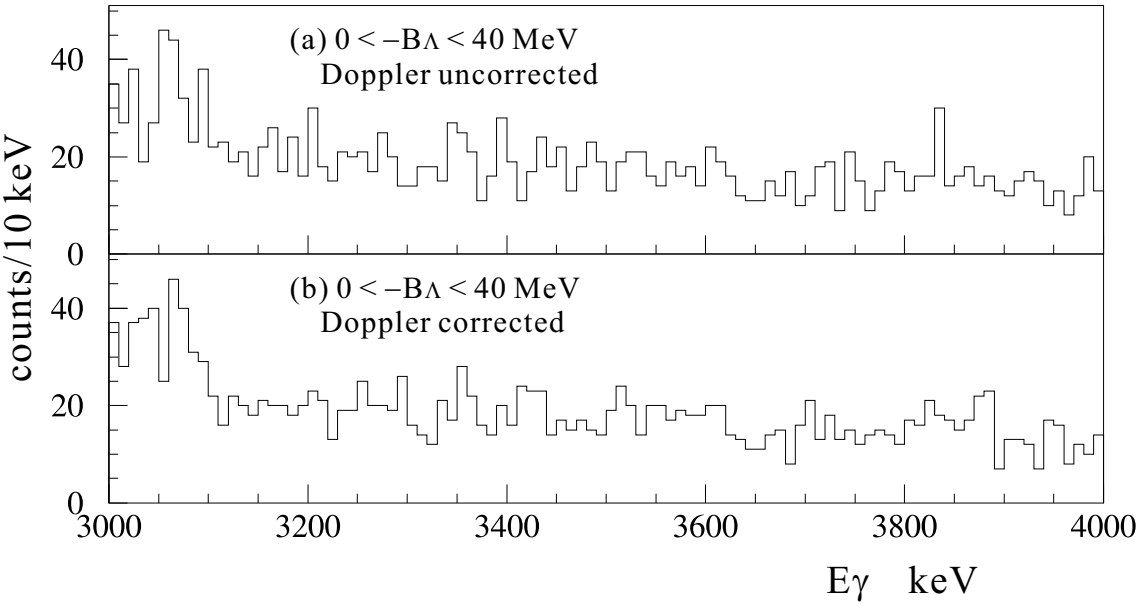

Figure 6.12: *Mass-gated γ-ray spectra around 3.5 MeV in the ^{10}B (K^-, π^-) reaction. Both (a) and (b) are plotted for s-substitutional state region, and (a) is Doppler-shift uncorrected and (b) is Doppler-shift corrected.*

6.3.3 γ- γ coincidence with E2 transition

We could not find a prominent peak around 400 keV corresponding to the M1 transition ($\frac{7}{2}^+ \rightarrow \frac{5}{2}^+$). However, since the transition is expected to make a Doppler broadened peak and the background level is high, the sensitivity for detecting the M1 transition is expected to be small. We performed γ-γ coincidence with the 2050 keV γ ray with a loose mass gate of $0 < -B_\Lambda < 100$ MeV (see Fig. 6.13). Figure 6.14 shows the γ-ray spectra in coincidence with another γ ray at (a) 2050 $\pm$ 8 keV, (b) 2020 $\pm$ 8 keV and (c) 2080 $\pm$ 8 keV. In Fig. 6.14 (a), a prominent peak appears at 470 keV with low background.

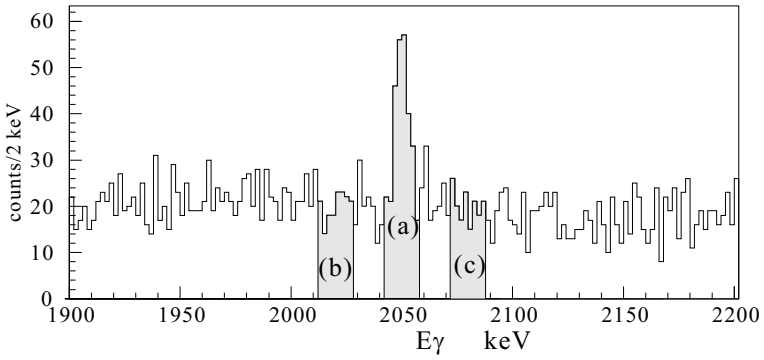

Figure 6.13: *Loose mass-gated ($0 < -B_\Lambda < 100$ MeV) γ-ray spectrum around 2050 keV peak. (a), (b) and (c) shows the regions for γ-γ coincidence (see Fig. 6.14)*

Probability of random fluctuation

We considered the probability of seven background events appearing in the narrow region of 470 $\pm$ 10 keV produced by random fluctuation. Figure 6.15 shows the loose mass-gated γ-ray spectra in coincidence. (a) is in coincidence with the E2 transition of ${}^{7}_{\Lambda}$Li (the same spectrum as Fig. 6.14 (a)) and (b) is in coincidence with another γ ray at $2100 < E_\gamma < 4000$ keV. The singles γ-ray count at $2042 < E_\gamma < 2058$ was 292 counts, and that at $2100 < E_\gamma < 4000$ was 10327 counts. Then, Fig. 6.15 (b) right axis shows the expected background counts for 292 single counts per each 5 keV bin. Then we obtained the background counts to be 0.509 ± 0.120 at 470 $\pm$ 10 keV. The distribution of background events can be expressed by a Poisson distribution. The probability of making a peak of more than 7 counts with 20 keV width by random fluctuation is estimated as

$$P(\geq 7) = 1 - \sum_{i=0}^{6} P(i) = 1.13^{+3.28}_{-0.89} \quad \times 10^{-6}$$

$$P(i) = \frac{0.509^i \cdot e^{-0.509}}{i!}$$

So, the probability that such peak accidentally appears anywhere in 1 MeV energy region by random fluctuation is

$$1.13 \times 10^{-6} \times 1000/20 = 0.56 \times 10^{-2} \quad \%.$$

As a result, the possibility that the 470 keV peak is due to a fluctuation is rejected.

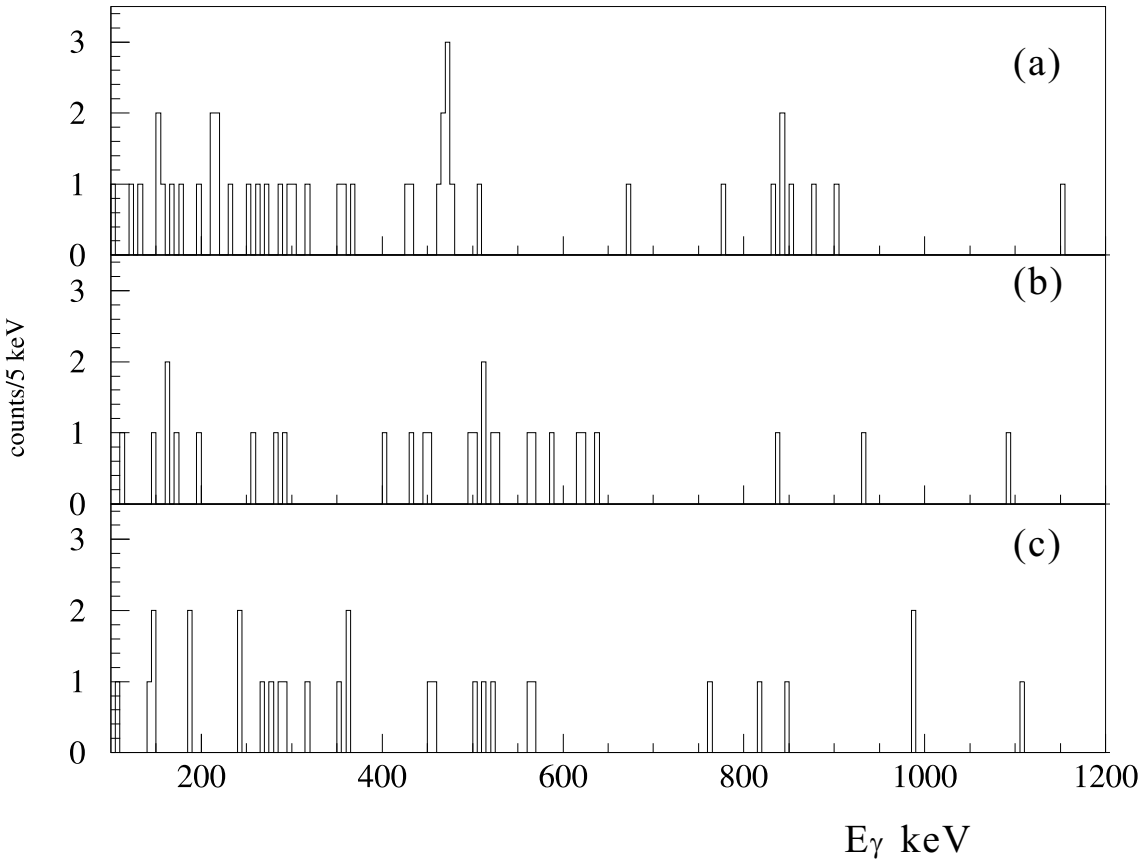

Figure 6.14: *γ-γcoincidence with the E2 transition of ${}^{7}_{\Lambda}Li$ and near energies (a) is in coincidence with another γ far at 2050 $\pm$ 8 keV, (b) is in coincidence with 2020 $\pm$ 8 keV, and (c) is in coincidence with 2080 $\pm$ 8 keV. All the spectra are plotted for $0 < -B_{\Lambda} < 100$ MeV (see Fig. 6.13).*

We estimated the probability P_{E_γ} that the observed counts within $E_\gamma \pm 10$ keV appear by random fluctuations of the background. P_{E_γ} is given by

$$P_{E_\gamma}(\geq N_{coin}) = 1 - \sum_{i=0}^{Ncoin-1} P(i), \qquad P(i) = \frac{N_{b.g}(E_\gamma)^i \cdot e^{-Nb.g}}{i!}$$

where N_{coin} is measured counts in the range from $E_\gamma - 10$ keV to $E_\gamma + 10$ keV, and $N_{b.g}$ is the estimated background counts in the same range. Figure 6.16 shows the probability P_{E_γ} as a function of energy in 5-keV bins. In Fig. 6.16 we also observed another gathering of four events around 840 keV. The probability was estimated to be $7.71^{+6.80}_{-4.43} \times 10^{-3}$. Existence of another peak at 840 keV can not be rejected, but the probability that such events occur due to background in any of the 20 keV-wide bins in the region from 0 to 1 MeV is 38.6 %, which shows that such an event frequently happens.

Fitting

We fitted the 470 keV peak with a Gaussian function and a constant background. Figure 6.17 shows the γ-ray spectrum around the peak and the result of the fit. We obtained a γ-ray energy of 470.4 $\pm$ 1.8 (stat.) $\pm$ 1.1 (sys.) keV, a yield of 6.7 $\pm$ 2.6 (stat.) $\pm$

0.1 (sys.) and the peak width of 10.1 ± 3.0 keV (FWHM). The results of the fit are summarized in Table 6.3.

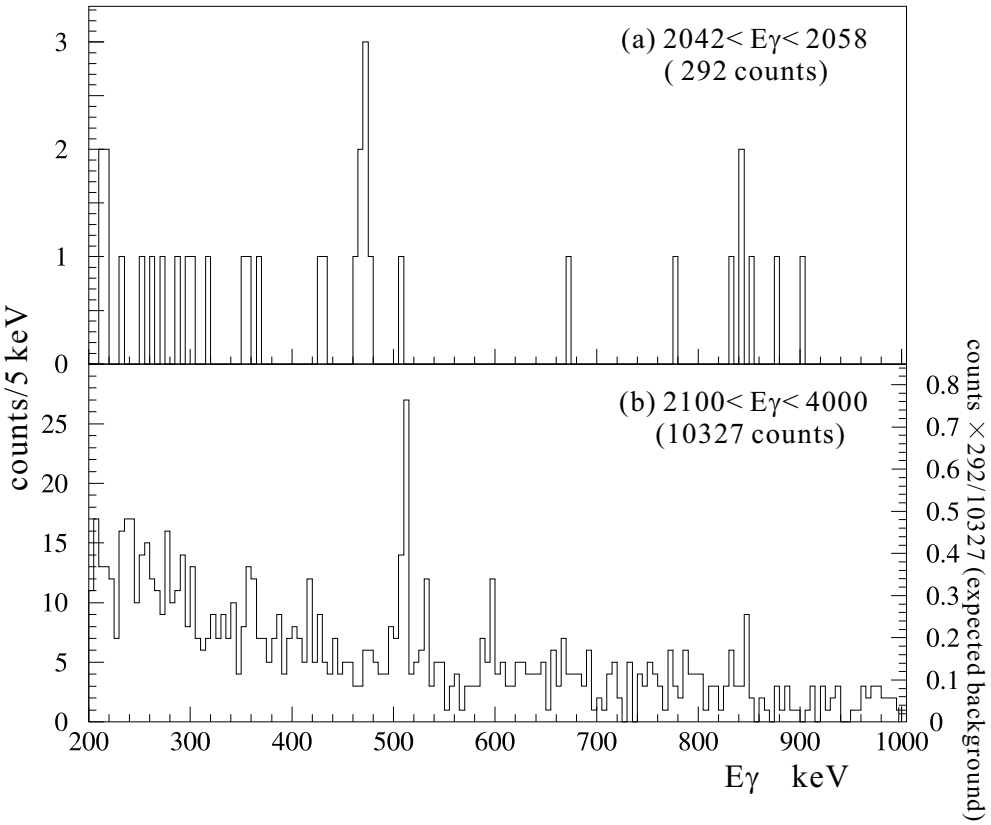

Figure 6.15: *γ-γ coincidence spectra in the $^{10}B(K^-,\pi^-)$ reaction. (a) coincidence with E2 transition of $^{7}_{\Lambda}Li$ and (b) coincidence with 2100 < E_γ < 4000 keV. (b) is used to estimate of background in the spectrum (a).*

6.3.4 Level assignment

γ-rays which can be emitted in coincidence with the E2 transition of $^{7}_{\Lambda}$Li ($\frac{5}{2}^+ \rightarrow \frac{1}{2}^+$) are as follows.

- The γ rays emitted after weak decay of $^{7}_{\Lambda}$Li.
- The spin-flip M1 transition of the upper doublet $^{7}_{\Lambda}$Li ($\frac{7}{2}^+ \rightarrow \frac{5}{2}^+$).

First, we consider whether the observed γ ray of 470 keV is emitted from ^{7}Li* (478 keV) which is produced after weak decay of $^{7}_{\Lambda}$Li, although the observed γ-ray energy is significantly lower than the γ-ray energy from ^{7}Li* (478 keV). The ground state of $^{7}_{\Lambda}$Li decays into ^{7}Be or ^{7}Li through the π^- or π^0 mesonic weak decays, respectively. When $^{7}_{\Lambda}$Li decays into their first excited states ^{7}Be$^*(\frac{1}{2}^-)$ or ^{7}Li$^*(\frac{1}{2}^-)$, γ ray of 429 keV or 478 keV is emitted subsequently. The decay branching ratio of $^{7}_{\Lambda}$Li into ^{7}Be (429 keV) and ^{7}Li (478 keV) were theoretically calculated by Motoba et al. [45] to be 5.8 % and 2.9 %, respectively. The branching ratio into ^{7}Be (429 keV) was measured with Hyperball [46] to be 6 %. Figure 6.18 shows the expected and experimentally obtained level scheme

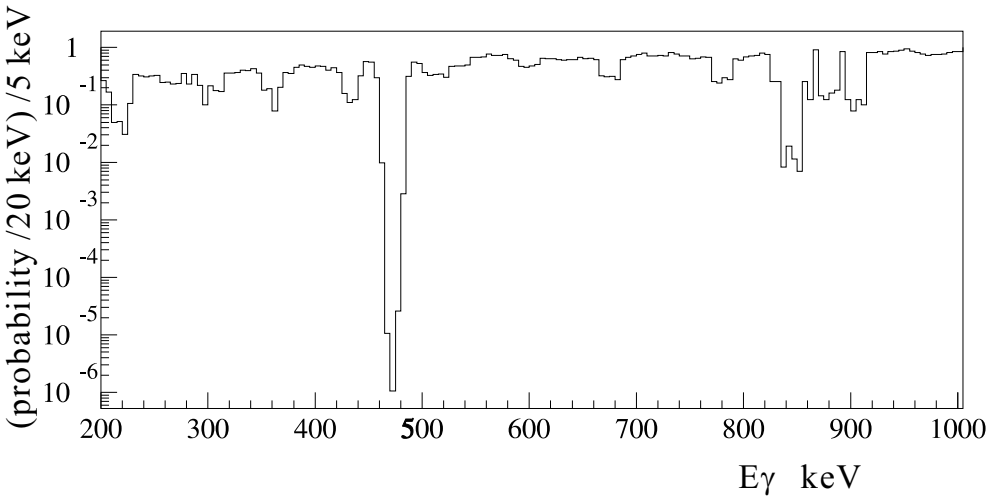

Figure 6.16: *Random fluctuation probability*

of the weak decay and branching ratio of ${}^{7}_{\Lambda}$Li. We estimated the expected counts of the ^{7}Li* 478 keV γ ray as

$$N = \varepsilon_{\gamma}(478) \cdot N_{\gamma}^{single}(2050) \cdot BR_{weak}({}^{7}_{\Lambda}\mathrm{Li}^{*}(478)) = 0.19 \pm 0.03 \quad [\mathrm{counts}], \tag{6.1}$$

where

$$BR_{weak}({}^{7}_{\Lambda}\mathrm{Li}^{*}(470)) = 2.9 \times 10^{-2}, \varepsilon_{\gamma}(470) = 5.0 \pm 1.5 \times 10^{-2}, N_{\gamma}^{single}(2050) = 132 \pm 18.$$

Therefore, the possibility that the observed 470-keV γ ray is emitted from ^{7}Li following weak decay is rejected. In addition, the γ-ray emitted after weak decay does not make such a broad peak, because the ground state of ${}^{7}_{\Lambda}$Li decays after it completely stops in the target medium.

Because of these reasons, the observed γ-ray of 470 keV is assigned as the spin-flip M1 transition ($\frac{7}{2}^{+} \rightarrow \frac{5}{2}^{+}$) of ${}^{7}_{\Lambda}$Li. Figure 6.19 shows the experimentally determined level scheme of ${}^{7}_{\Lambda}$Li. We have thus determined all the bound states of ${}^{7}_{\Lambda}$Li. It is remarkable that we observed the spin-flip M1 transition of the upper doublet ($\frac{7}{2}^{+}, \frac{5}{2}^{+}$) only in 48 hours beam time.

We estimated the decay branching ratio between ${}^{10}_{\Lambda}\mathrm{B} \rightarrow {}^{7}_{\Lambda}\mathrm{Li}(\frac{5}{2}^{+})$ (+ ^{3}He) and ${}^{10}_{\Lambda}\mathrm{B} \rightarrow {}^{7}_{\Lambda}\mathrm{Li}(\frac{7}{2}^{+})$ (+ ^{3}He) $\rightarrow {}^{7}_{\Lambda}\mathrm{Li}(\frac{5}{2}^{+}) + \gamma(471)$ as

$$R\left(\frac{7/2^{+}}{5/2^{+} + 7/2^{+}}\right) = \frac{N_{\gamma}^{coin}(471)/\varepsilon_{\gamma}(471)}{N_{single}(2050)} = 1.01 \pm 0.51 \tag{6.2}$$

Consequently, more than a half of the $\frac{5}{2}^{+}$ state events are produced via ${}^{10}_{\Lambda}\mathrm{B} \rightarrow {}^{7}_{\Lambda}\mathrm{Li}(\frac{7}{2}^{+}) +$ ^{3}He.

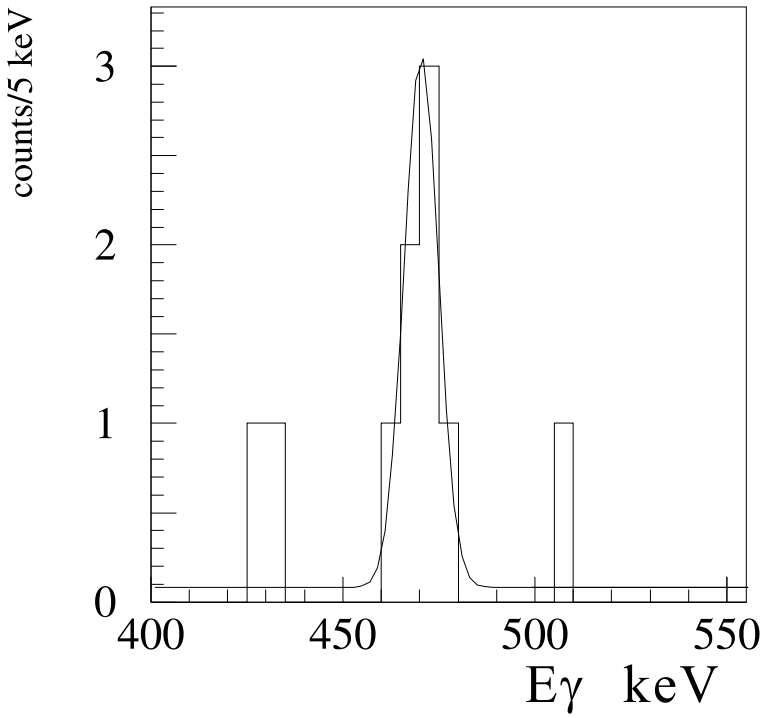

Figure 6.17: *γ-ray energy spectrum in coincidence with the 2050 keV γ-ray. The results of the fit is shown in the solid line.*

Table 6.3: *Summary of ${}^{7}_{\Lambda}Li$ γ rays from ${}^{10}_{\Lambda}B$*

transition	M1($\frac{3}{2}^+ \rightarrow \frac{1}{2}^+$)	E2($\frac{5}{2}^+ \rightarrow \frac{1}{2}^+$)	M1($\frac{7}{2}^+ \rightarrow \frac{5}{2}^+$)
energy [keV]	$691.5 \pm 0.6 \pm 0.6$	$2050.1 \pm 0.4 \pm 0.6$	$470.7 \pm 1.8 \pm 1.1$
single counts ($0< -B_\Lambda <40$)	170 ± 26	105 ± 14	–
single counts ($0< -B_\Lambda <100$)	201 ± 34	132 ± 18	–
coincidence counts	–	–	6.7 ± 2.6
peak width (FWHM) [keV]	7.3 ± 1.5	5.7 ± 1.0	10.1 ± 3.0

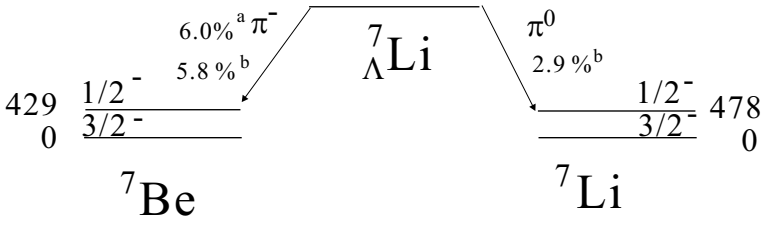

Figure 6.18: *Schematic diagram of ${}^{7}_{\Lambda}Li$ mesonic weak decay. a; experimentally determined [46] and b; theoretical calculation by Motoba et al [45].*

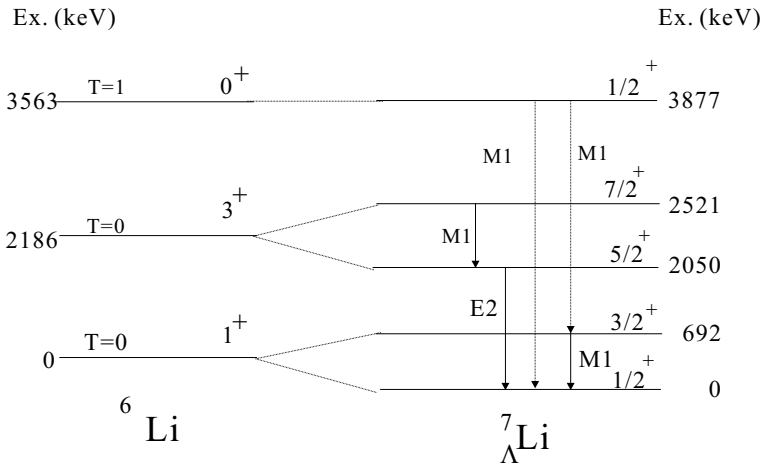

Figure 6.19: *Experimentally determined level scheme of* ${}^{7}_{\Lambda}Li$*. from present experiment and previous experiment (KEK E419) [9, 15, 10]*

6.4 Sensitivity of M1 transition of ${}^{10}_{\Lambda}$B

In the ^{10}B (K^-, π^-) reaction, we observed 160 $\pm$ 35 counts for the ${}^{9}_{\Lambda}$Be $(\frac{5}{2}^+, \frac{3}{2}^+ \rightarrow \frac{1}{2}^+)$ E2 transitions. However, we did not observed the ${}^{10}_{\Lambda}$B$(2^- \rightarrow 1^-)$ M1 transition.

Although a quantitative assessment is difficult, most of the ${}^{9}_{\Lambda}$Be states are produced from the $p_n^{-1}s_\Lambda$ states of ${}^{10}_{\Lambda}$B as summarized in Table 6.1. The formation strength for the 2^- state in the ground-state doublet is 0.292 and for the others is 0.742. The observed γ-ray yield of the 3-MeV E2 transitions of ${}^{9}_{\Lambda}$Be was $N_\gamma(3024) + N_\gamma(3067) = 160 \pm 35$ counts with an efficiency of $\varepsilon_\gamma(3000\ \mathrm{keV}) = 1.2\ \%$. The expected γ-ray yield of the ${}^{10}_{\Lambda}$B$(2^- \rightarrow 1^-)$ is roughly obtained by

$$Y_{M1}(E_\gamma) = (N_\gamma(3067) + N_\gamma(3026)) \times R \times \frac{0.292}{0.742} \times \frac{\varepsilon_\gamma(E_\gamma)}{\varepsilon_\gamma(3000\ [\mathrm{keV}])}$$

where E_γ is the energy of the $(2^- \rightarrow 1^-)$ transition and R is the production rate of the ${}^{9}_{\Lambda}$Be excited states $(\frac{3}{2}^+, \frac{5}{2}^+)$ from the $p_n^{-1}s_\Lambda$ states of ${}^{10}_{\Lambda}$B and defined as

$$R = \frac{N(p_n^{-1}s_\Lambda \rightarrow {}^{9}_{\Lambda}\ \mathrm{Be}^*)}{N(p_n^{-1}s_\Lambda \rightarrow {}^{9}_{\Lambda}\ \mathrm{Be}^*) + N(p_n^{-1}p_\Lambda \rightarrow {}^{9}_{\Lambda}\ \mathrm{Be}^*)}.$$

Here, the efficiency ratio $\varepsilon_\gamma(E_\gamma)/\varepsilon_\gamma(3000\ [\mathrm{keV}])$ is estimated to be 9.1 for E_γ=100 keV, 6.9 for 200 keV and 5.3 for 300 keV (see Fig. 4.15). The p-substitutional states are expected to decay primarily by Λ emission and the excited states of ${}^{9}_{\Lambda}$Be are dominantly produced from the $p_n s_\Lambda$ states. Therefore, R is expected to be close to 1 [27]. If we assume $R = 1$ (0.5), the yield Y_{M1} is estimated to be 572 (286) counts for $E_\gamma = 100$ keV, 434 (217) counts for 200 keV and 334 (167) counts for 300 keV. Since for these γ-ray energies, the energy is expected not to be broadened by Doppler shift, the peaks width is expected to be the same as the energy resolution of 3.5 keV(FWHM). In this yield estimation, we assumed that, when the γ-ray energy is larger than 100 keV, the competition with the weak decay is negligible. The sensitivity of the γ-ray detectopm is expected to be large enough. Therefore, the M1 transition γ-ray energy is determined to be smaller than 100 keV. With high statistics, our result confirmed the old experiment using germanium detectors by the ^{10}B (K^-, π^-) ${}^{10}_{\Lambda}$B reaction [11] which reported that the spacing $E(2^-) - E(1^-)$ is smaller than 80 keV.

Chapter 7

Discussion

In this chapter, firstly, we will discuss the tensor force strength from the ground-state doublet of ${}^{16}_{\Lambda}$O on the assumption that all the other parameters were already determined uniquely. Next, we will discuss all the spin-dependent ΛN interactions.

7.1 Background to the parameterization

7.1.1 Previous values of the parameters

The strengths of the ΛN spin-dependent interactions were determined in the previous experiments except for the tensor force. For example, the strength of the spin-spin force was derived to be $\Delta = 432$ keV from the ground-state doublet spacing of ${}^{7}_{\Lambda}\mathrm{Li}(\frac{3}{2}^{+}, \frac{1}{2}^{+})$. Although the sign of S_Λ was not determined from the previous ${}^{9}_{\Lambda}$Be data, we took a negative value, because the ${}^{13}_{\Lambda}$C data suggested a negative value [47]. Table 7.1.1 shows the hypernuclear levels measured in the previous experiments and the parameter values derived from them.

Table 7.1: *Spin-dependent ΛN interaction parameters derived from the previous data (original values)*

	Δ	S_Λ	S_N
measured levels	${}^{7}_{\Lambda}\mathrm{Li}(\frac{3}{2}^{+}, \frac{1}{2}^{+})$[9]	${}^{9}_{\Lambda}\mathrm{Be}(\frac{3}{2}^{+}, \frac{5}{2}^{+})$[12]	${}^{7}_{\Lambda}\mathrm{Li}(\frac{5}{2}^{+}, \frac{1}{2}^{+})$[9]
derived values [keV]	432	$-20 \sim -3/(15 \sim 30)$	-380

7.1.2 Radius dependence of the parameters

Although in an earlier paper [6] the parameters were assumed to be constants throughout the p-shell hypernuclei, in reality the parameters should take larger values for the heavier hypernuclei, because both the nucleon and Λ orbits becomes more deeply bound with more confined wave functions despite an $A^{1/3}$ increase in the radius of the Woods-Saxon potential wells. Table 7.2 shows for the $p_N s_\Lambda$ parameters as a function of A for Wood-Saxon wave functions and scale factors of the parameters for the hypernuclei (This table is give in Table 2 of Ref. [48] and modified). We defined the scale factor for

Table 7.2: *Radius dependence for the parameters. $p_n s_\Lambda$ as a function of A for Woods-Saxon wave function, where $r_0 = 1.25$ fm and $a = 0.6$ fm for nucleons, and $r_0 = 1.128 + 0.439A^{2/3}$ fm and $a = 0.6$ fm for Λ.*

	${}^{7}_{\Lambda}$Li	${}^{9}_{\Lambda}$Be	${}^{16}_{\Lambda}$O	${}^{10}_{\Lambda}$B	${}^{15}_{\Lambda}$N
$B_\Lambda(0s)$ [MeV]	5.58	6.73	13.0		
$B_n(0p)$ [MeV]	5.56	18.90	16.31		
$<r^2>^{1/2}(0s_\Lambda)$ (fm)	2.63	2.55	2.32		
$<r^2>^{1/2}(0p_N)$ (fm)	2.86	2.34	2.66		
scale factor	1	1.29	1.08	1.06	1.08

${}^{7}_{\Lambda}$Li to be 1. The scale factors for ${}^{10}_{\Lambda}$B and ${}^{15}_{\Lambda}$N were not presented in Ref. [48], we used 1.06 for ${}^{10}_{\Lambda}$B and 1.08 for ${}^{15}_{\Lambda}$N [27]. Of the parameters given in Table 7.1.1, Δ and S_N are applicable values to ${}^{7}_{\Lambda}$Li, and S_Λ is applicable value to ${}^{9}_{\Lambda}$Be. Therefore the values should be corrected to apply to other hypernuclei. The corrected values of parameters are given in Table 7.3, in which they are applicable to ${}^{7}_{\Lambda}$Li and ${}^{16}_{\Lambda}$O.

Table 7.3: *Spin-dependent parameters corrected from 7.2 for the variation in radial wave functions with size and binding energy. These are the same values in Table 7.1.1.*

	Δ	S_Λ	S_N
values in ${}^{7}_{\Lambda}$Li [keV]	432	$-15 \sim -2$	-380
values in ${}^{16}_{\Lambda}$O [keV]	467	$-16 \sim -2$	-410

7.2 Determination of the tensor force

I will derive the strength of the tensor force from the ground-state doublet spacing of ${}^{16}_{\Lambda}$O. We have determined experimentally the separation energy and spins of the ground-state doublet of ${}^{16}_{\Lambda}$O. The spacing is given, as in Section 1.5.1, by

$$E(1^-_1) - E(0^-) = -0.382\Delta + 1.378S_\Lambda - 0.004S_N + 7.850T + \Lambda\Sigma$$

$$= 26 \quad \text{[keV]}.$$

In this equation, we input the parameter values shown in Table 7.3 and $\Lambda\Sigma = -30$ keV (calculated by Millener[8]). Then we derived the strength of the tensor force, $T = +31 \sim 34$ keV. This is the first experimental determination of the strength of the tensor force.

7.3 Improvement and consistency check

By the determination of the tensor force strength, we have obtained the strengths of all the ΛN spin-dependent interactions. Previously, the Δ, S_Λ and S_N parameters

were determined in spite of the lack of experimental data for the tensor force. It was assumed that the tensor force is as small as the predicted values by meson-exchange models ($T = 0.02 \sim 0.06$ MeV). Now we can improve all the parameters with the experimentally determined tensor force strength and check the consistency of all the parameters with new data.

The procedure to derive parameter values is as follows. First, we estimate one parameter and fix it while we estimate the other parameters. Then we estimate the former parameter using the improved values of of the latter parameters and so on until converged. Table 7.4 gives the levels for which measurements were made in the present and previous experiments and the strengths of all the ΛN spin-dependent parameters derived from them in following subsections. All the values are scaled to the values for ${}^{7}_{\Lambda}$Li. In the following subsections, we discuss each parameter and try to determine optimal values for them.

Table 7.4: *Strengths of all the spin-dependent interactions. Values are scaled for* ${}^{7}_{\Lambda}Li$

	strength [keV]	level
Δ	$440 \sim 335$	${}^{7}_{\Lambda}\mathrm{Li}(\frac{3}{2}^+,\frac{1}{2}^+)$, ${}^{7}_{\Lambda}\mathrm{Li}(\frac{7}{2}^+,\frac{5}{2}^+)$, ${}^{15}_{\Lambda}\mathrm{N}(\frac{3}{2}^+_2,\frac{1}{2}^+_2)$
S_Λ	$-15 \sim 0/12 \sim 23$	${}^{9}_{\Lambda}\mathrm{Be}(\frac{3}{2}^+,\frac{5}{2}^+)$
S_N	$-440 \sim -450$	${}^{7}_{\Lambda}\mathrm{Li}$ $(\overline{(\frac{7}{2}^+,\frac{5}{2}^+)},\overline{(\frac{3}{2}^+,\frac{1}{2}^+)})$
T	$24 \sim 30$	${}^{16}_{\Lambda}\mathrm{O}(1^-_1,0^-)$

7.3.1 The spin-spin force

Strength of the spin-spin force, Δ, was already determined to be ~ 0.4 MeV from the ground-state doublet spacing of ${}^{7}_{\Lambda}\mathrm{Li}(\frac{3}{2}^+,\frac{1}{2}^+)$. To reproduce the ground-state doublet spacing of 692 keV, Δ was derived to be 440 keV with the $\Lambda-\Sigma$ coupling and other improved parameters (in Table 7.4) included.

In the present experiment, we measured three doublet spacings which have a large contribution from the spin-spin force. They are the ground-state doublet spacing of less than 100 keV for ${}^{10}_{\Lambda}\mathrm{B}(2^-,1^-)$, the upper-doublet spacing of 471 keV for ${}^{7}_{\Lambda}\mathrm{Li}(\frac{7}{2}^+,\frac{5}{2}^+)$ and the upper-doublet spacing of 481 keV for ${}^{15}_{\Lambda}\mathrm{N}(\frac{3}{2}^+_2,\frac{1}{2}^+_2)$. We now derive Δ independently using these results.

(1) ${}^{10}_{\Lambda}\mathbf{B}(2^-,1^-)$

First, we discuss the ground state of ${}^{10}_{\Lambda}\mathrm{B}(2^-,1^-)$. The level scheme is shown in Fig. 6.3. The spacing is given by,

$$E(2^-)-E(1^-) = 0.578\Delta + 1.414S_\Lambda + 0.014S_N - 1.068T + \Lambda\Sigma$$

$$< 100 \qquad [\mathrm{keV}]$$

where the values of the parameters we used are given as follows except for Δ.

	input				output
	S_Λ	S_N	T	$\Lambda\Sigma$	Δ
scaled to ${}^{10}_{\Lambda}\mathrm{B}$ [keV]	-12	-472	29	-15	$-50 < \Delta < 298$

Then, we derived $-50 < \Delta < 310$ keV, which corresponds to $-47 < \Delta < 292$ keV when scaled to ${}^{7}_{\Lambda}$Li.

(2) ${}^{15}_{\Lambda}$N$(\frac{3}{2}^{+}_{2}, \frac{1}{2}^{+}_{2})$

Second, we discuss the upper-doublet spacing of 481 keV for of ${}^{15}_{\Lambda}\mathrm{N}(\frac{3}{2}^{+}_{2}, \frac{1}{2}^{+}_{2})$. The level scheme is shown in Fig. 5.14. The spacing is given by,

$$E(\tfrac{3}{2}^{+}_{2}) - E(\tfrac{1}{2}^{+}_{2}) = 1.373\Delta + 0.117S_{\Lambda} + 0.064S_{N} - 1.579T + \Lambda\Sigma$$

$$= +481 \text{ or } -481 \qquad \text{[keV]},$$

where the parameters are given as follows.

	input				output
	S_{Λ}	S_{N}	T	$\Lambda\Sigma$	Δ
scaled to ${}^{15}_{\Lambda}$N [keV]	-12	-480	29	63	362
					-339

When we assume that the upper level of the doublet is $\frac{3}{2}^{+}$, we find $\Delta = 363$ keV, while the assumption that the upper level of the doublet $\frac{1}{2}^{+}$ leads to $\Delta = -339$ keV, which correspond to$\Delta = 335$ keV and $\Delta = -314$ keV when scaled to ${}^{7}_{\Lambda}$Li.

(3) ${}^{7}_{\Lambda}$Li$(\frac{7}{2}^{+}, \frac{5}{2}^{+})$

Third, we discuss the upper-doublet spacing of ${}^{7}_{\Lambda}$Li The spacing is given by,

$$E(\tfrac{7}{2}^{+}) - E(\tfrac{5}{2}^{+}) = 1.311\Delta + 2.141S_{\Lambda} + 0.024S_{N} - 2.324T + \Lambda\Sigma$$

$$= 471 \qquad \text{[keV]}$$

where the parameters are given as follows.

	input				output
	S_{Λ}	S_{N}	T	$\Lambda\Sigma$	Δ
scaled to ${}^{7}_{\Lambda}$Li [keV]	-11	-445	28	74	378

Then we derived $\Delta = 378$ keV.

In the previous ${}^{7}_{\Lambda}$Li experiment, Δ was derived to be $\Delta \sim 0.4$ MeV. We checked the consistency of Δ with new data for three independent hypernuclear levels. Both of the upper-doublet spacing of ${}^{7}_{\Lambda}$Li and ${}^{15}_{\Lambda}$N give a consistent result with the ground-state doublet spacing of ${}^{7}_{\Lambda}$Li. However, the ${}^{10}_{\Lambda}$B data give a value less than 0.3 MeV. One suggestion to explain the spacing of ${}^{10}_{\Lambda}$B is a possible larger contribution of ΛNN three body force. Therefore, more theoretical examination is necessary to explain the ground-state doublet spacing of ${}^{10}_{\Lambda}$B as well as other doublet spacings, and more experimental data which give information on Δ are necessary.

In the following discussion, we fix Δ to be $335 \sim 440$ keV (scaled to ${}^{7}_{\Lambda}$Li) and used the scaled values for each hypernucleus.

7.3.2 The tensor force

We measured the energy of the ground-state doublet spacing of ${}^{16}_{\Lambda}$O and an upper limit energy of the ground-state doublet spacing of ${}^{15}_{\Lambda}$N. We will discuss again the strength of the tensor force using these results.

(1) ${}^{16}_{\Lambda}\mathbf{O}(1^-, 0^-)$

We derive the strength of the tensor force from the ground-state doublet spacing of ${}^{16}_{\Lambda}$O. We obtained the spacing energy and spins of the ground-state doublet of ${}^{16}_{\Lambda}$O. The spacing is given by,

$$E(1^-_1) - E(0^-) = -0.382\Delta + 1.378S_\Lambda - 0.004S_N + 7.850T + \Lambda\Sigma$$

$$= 26 \quad [\text{keV}].$$

where the parameters we used were as follows.

	input				output
	Δ	S_Λ	S_N	$\Lambda\Sigma$	T
scaled to ${}^{16}_{\Lambda}$O [keV]	$475 \sim 365$	-12	-481	-30	$26 \sim 32$

Then we derive the strength of the tensor force to be $T = +32$ keV with $\Delta = 475$ keV and $T = +26$ keV with $\Delta = 365$ keV.

(2) ${}^{15}_{\Lambda}\mathbf{N}(\frac{1}{2}^+_1, \frac{3}{2}^+_1)$

Next, we discuss the ground-state doublet spacing of ${}^{15}_{\Lambda}$N. From the experiment we limited the spacing to be less than 100 keV. The spacing is given by

$$E(\tfrac{3}{2}^+) - E(\tfrac{1}{2}^+) = 0.756\Delta - 2.25S_\Lambda + 0.035S_N - 9.862T + \Lambda\Sigma$$

$$< 100 \quad [\text{keV}]$$

where the parameters are given as follows.

	input				output
	Δ	S_Λ	S_N	$\Lambda\Sigma$	T
scaled to ${}^{15}_{\Lambda}$N [keV]	$475 \sim 365$	-12	-481	46	$23 < T < 52$

Then we derive $+32 < T < +52$ keV with $\Delta = 475$ keV, and $+23 < T < +43$ keV with $\Delta = 365$ keV.

The derived strengths of the tensor force are not inconsistent with each other. Even with $\Delta \sim 0.3$ MeV, T is derived to be $+20$ keV from the spacing of ${}^{16}_{\Lambda}$O, and the spacing energy of ${}^{15}_{\Lambda}$N becomes ~ 80 keV.

The predicted values of T by the Nijmegen meson-exchange models shown in Table 1.1 ($+18 \sim +54$ keV) agree with our result.

7.3.3 The Λ-spin-dependent spin-orbit force

The strength of the Λ-spin-dependent spin-orbit force was already determined ($|S_\Lambda|<$ 0.03 MeV) from the spacing of ${}^{9}_{\Lambda}\mathrm{Be}(\frac{3}{2}^+, \frac{5}{2}^+)$ in the previous experiment. However, at that time the spins were not determined. When a value for S_Λ was derived, the strength of the tensor force, T, was assumed to lie in their range $0.02 < T < 0.06$ predicted by meson-exchange models because of a lack of experimental data on T. In the present experiment, the spins of the states were assigned and the strength of the tensor force has been experimentally determined.

${}^{9}_{\Lambda}\mathrm{Be}(\frac{3}{2}^+, \frac{5}{2}^+)$

The doublet spacing of ${}^{9}_{\Lambda}\mathrm{Be}$, which is mainly determined by S_Λ and T, is given by

$$E(\tfrac{3}{2}^+) - E(\tfrac{5}{2}^+) = -0.037\Delta - 2.464S_\Lambda + 0.003S_N + 0.994T + \Lambda\Sigma$$

$$= +43 \qquad [\mathrm{keV}]$$

where the parameters are given as follows,

	input				output
	Δ	S_N	T	$\Lambda\Sigma$	S_Λ
in ${}^{9}_{\Lambda}\mathrm{Be}$ [keV]	$567 \sim 436$	-568	$39 \sim 32$	-8	-14

Then, S_Λ is derived to be $-14 \sim -15$ keV for T of $+32 \sim +39$ keV.

7.3.4 The N-spin-dependent spin-orbit force

The strength of the N-spin-dependent spin-orbit force was previously determined ($S_N = 0.4 \sim 0.5$ MeV) from the measurement of the core-excitation levels of ${}^{7}_{\Lambda}\mathrm{Li}$, ${}^{13}_{\Lambda}\mathrm{C}$ and ${}^{12}_{\Lambda}\mathrm{C}$. However, no measurement was made from the energy spacing between the spin-weighted average of the two doublets, which is almost only determined on the S_N term. Since in the present experiment we determined all the spins and all the energies for the bound states of ${}^{7}_{\Lambda}\mathrm{Li}$, we can determine an S_N value with smaller ambiguity.

${}^{7}_{\Lambda}\mathrm{Li}$ $(\overline{(\frac{7}{2}^+, \frac{5}{2}^+)}, \overline{(\frac{3}{2}^+, \frac{1}{2}^+)})$

We will derive S_N from the ground-state doublet $(\frac{3}{2}^+, \frac{1}{2}^+)$ and upper-doublet states $(\frac{7}{2}^+, \frac{5}{2}^+)$ of ${}^{7}_{\Lambda}\mathrm{Li}$. The spin-averaged excitation energy is described as,

$$\overline{E}(\tfrac{7}{2}^+, \tfrac{5}{2}^+) - \overline{E}(\tfrac{3}{2}^+, \tfrac{1}{2}^+) = \Delta E_{core} - 0.06\Delta + 0.08S_\Lambda + 0.68S_N - 0.05T$$

$$= 1858 \qquad [\mathrm{keV}]$$

where $\overline{E}$ denotes spin-averaged energy of the doublet and ΔE_{core} corresponds to the core-excitation energy of ${}^{6}_{\Lambda}\mathrm{Li}(3^+)$ of 2186 keV, and other parameters are given as

	input				output
	ΔE_{core}	Δ	S_Λ	T	S_N
in ${}^{7}_{\Lambda}\mathrm{Li}$ [keV]	2168	$440 \sim 335$	-11	28	$-440 \sim -450$

Then we derived $S_N = -440 \sim -450$ keV.

7.3.5 Summary on the spin-dependent interaction parameters

We summarize the spin-dependent interaction parameters obtained in the present experiment. Before the present experiment, the experimental information on the parameters was limited. The sign of S_Λ and the value of T were not experimentally determined, and Δ and S_N were determined only from ${}^{7}_{\Lambda}\mathrm{Li}(\frac{5}{2}^+, \frac{3}{2}^+, \frac{1}{2}^+)$ levels. Owing to the results from the present experiment, all these uncertainties are removed, and all the previous values are improved. Table 7.5 lists again the previous and the present values of the spin-dependent interactions in Table 7.3, and in Table 7.4.

Table 7.5: *Summary on the Strengths of all the spin-dependent interactions, previous and present.*

	previous [keV]	present [keV]
Δ	432	$335 \sim 440$
S_Λ	$-15 \sim -2/12 \sim 23$	-11
S_N	-380	$-440 \sim -450$
T	–	$24 \sim 30$

7.4 Comparison with baryon-baryon interaction models

The strengths of all the spin-dependent interactions are determined from the results of the present experiment and the previous experiments with Hyperball. In particular, we experimentally obtained the strength of the tensor force for the first time.

The small strength of the tensor force T is predicted by the meson-exchange models and the predicted values are consistent with our result. On the other hand, both strength of the spin-orbit forces (S_Λ and S_N) seems to be explained well by quark model rather than the meson-exchange models. The meson-exchange models [49] and quark model [50, 51] predict almost the same strength for the symmetric LS force (SLS, $\propto \boldsymbol{l}_{N\Lambda}(\boldsymbol{s}_\Lambda+\boldsymbol{s}_N)$) of ~ 0.2 MeV, but, they predict different strength for the antisymmetric LS force (ALS, $\propto \boldsymbol{l}_{N\Lambda}(\boldsymbol{s}_\Lambda - \boldsymbol{s}_N)$) $\sim +0.05$ MeV (meson-exchange model) and $\sim +0.2$ MeV (quark model). Therefore, meson-exchange models predict S_Λ (SLS+ALS) to be -0.15 MeV and S_N (SLS$-$ALS) to be -0.25 MeV, while quark model predicts S_Λ to be almost zero and S_N to be -0.4 MeV. From the result ($S_\Lambda = -0.01$, and $S_N = -0.45$), it is established that the existing meson-exchange models can not explain the LS force, but quark model can.

It is interesting to point out that the tensor force is explained by the meson-exchange models, but, the LS force seems to be explained by the quark model. The LS force of NN interaction can be understood by both by the meson-exchange models and by the quark model, the LS force for ΛN interaction gives a clue to understand the origin of the LS force in baryon-baryon interactions.

7.5 New future possibility of γ spectroscopy using hyperfragments

We succeeded in measurement of the spin-flip M1 transition between the upper-doublet states of ${}^{7}_{\Lambda}$Li which corresponds to the transition of $\frac{7}{2}^{+} \rightarrow \frac{5}{2}^{+}$ in only 48 hours of beam time.

The $\frac{7}{2}^{+}$ state was produced by ^{3}He emission from the substitutional state of ${}^{10}_{\Lambda}$B and the M1 transition was found by the γ-γ coincidence technique. This is the first success of the γ- γ coincidence for hypernuclei. In addition, we also found γ-rays via the proton emission from ${}^{16}_{\Lambda}$O and ${}^{10}_{\Lambda}$B.

The success of the γ spectroscopy of hyperfragments opens new experimental possibilities in the future with an upgraded Hyperball and with a good kaon beam line at J-PARC.

Chapter 8

Conclusion

We performed a γ-ray spectroscopy experiment on p-shell hypernuclei with a germanium detector array, Hyperball, at BNL-AGS D6 line (BNL E930 '01). The purpose of the experiment is experimental determination of the strengths of the ΛN spin-dependent interactions for p-shell hypernuclei. We took data on the ^{16}O $(K^-, \pi^-\gamma)$ reaction to determine the strength of the tensor force and on the ^{10}B $(K^-, \pi^-\gamma)$ reaction to cross check the strengths of the ΛN spin-spin, Λ-spin-orbit and nucleon-spin-orbit interactions which were already determined from previous Hyperball experiments.

We succeeded in measurement of the γ rays of $^{16}_{\Lambda}$O and $^{15}_{\Lambda}$N by the ^{16}O (K^-, π^-) reaction. The observed γ rays of $^{16}_{\Lambda}$O were assigned to be the M1 transitions from the excited state (1^-_2) to both of the ground-state doublet members $(1^-_1, 0^-)$, and their energies were determined to be 6534.1 $\pm$ 1.5 (statistical) $\pm$ 1.7 (systematic) keV and 6560.2 $\pm$ 1.3 $\pm$ 1.7 keV. Then, we obtained a spacing energy of 26.1 $\pm$ 2.0 $\pm$ 0.2 keV and a yield ratio N(6534)/N(6560)=0.64 $\pm$ 0.12. From the γ-ray yield ratio, the spins of the ground-state doublet were determined to be 0^- for the lower state and 1^- for the upper state. From the spins and spacing energy, we derived the strength of the tensor force, T, to be 32 keV. This is the first time that the precise information on the ΛN tensor force was obtained experimentally. The meson-exchange baryon-baryon models predict T to be a few tens keV (20 keV $\sim$ 60 keV), consistent with our result. Therefore, it is found that the ΛN tensor force can be well described by the meson exchange picture.

We also measured γ rays of $^{15}_{\Lambda}$N which were produced via proton emission from the substitutional states of $^{16}_{\Lambda}$O. They are assigned as M1 transitions from the upper doublet states $(\frac{1}{2}^+_2, \frac{3}{2}^+_2)$ to the $\frac{1}{2}^+$;T=1 state and as an M1 transition from the $\frac{1}{2}^+$l;T=1 state to the $\frac{3}{2}^+$ member of the ground-state doublet. Because of the small branching ratio of the $\frac{1}{2}^+$;T=1 state to the $\frac{1}{2}^+_1$ state of the ground-state doublet, we could not determine the spacing energy of the ground-state doublet of $^{15}_{\Lambda}$N which is also sensitive to the tensor force. On the other hand, we determined the upper doublet $(\frac{3}{2}^+_2, \frac{1}{2}^+_2)$ spacing, though, we could not determine their spins experimentally. The spacing of the upper doublet of 481 $\pm$ 2.1 $\pm$ 1.4 keV gave information on the spin-spin interaction.

We could not detect the spin-flip M1 γ ray corresponding to $^{10}_{\Lambda}$B$(2^- \rightarrow 1^-)$. With consideration of the sensitivity of the experiment, we concluded that the energy spacing of the ground-state doublet of $^{10}_{\Lambda}$B is less than 100 keV. This result is consistent with the old experiment with germanium detectors.

We succeeded in a measurement of the γ rays of $^{9}_{\Lambda}$Be and $^{7}_{\Lambda}$Li via proton emission and ^{3}He emission from excited states of $^{10}_{\Lambda}$B. We measured the E2 transitions $(\frac{3}{2}^+, \frac{5}{2}^+ \rightarrow \frac{1}{2}^+)$

of ${}^{9}_{\Lambda}$Be which were already measured in the previous experiment. From the γ-ray yield ratio of ${}^{9}_{\Lambda}$Be, N(3024)/N(3067)=0.27 $\pm$ 0.13 $^{+0.08}_{-0.10}$, the spins of the doublet were determined; the upper state is $\frac{3}{2}^{+}$ and the lower state is $\frac{5}{2}^{+}$. The determination of the spins confirmed the negative sign of S_{Λ} .

We measured the spin-flip M1 transition ($\frac{3}{2}^{+}\rightarrow\frac{1}{2}^{+}$) and the E2 transition ($\frac{5}{2}^{+}\rightarrow\frac{1}{2}^{+}$) of ${}^{7}_{\Lambda}$Li which were already measured and in the previous experiment. We succeeded in a measurement of the spin-flip M1 transition of the upper doublet states ($\frac{7}{2}^{+}\rightarrow\frac{5}{2}^{+}$) via γ- γ coincidence with the E2 transition. Thus we determined the spins and excitation energies of all the bound states of ${}^{7}_{\Lambda}$Li, and the result provided a value for S_N of -440 keV with high precision.

We obtained all the strengths of the spin-dependent interactions. The small strengths of the tensor force are predicted by the meson-exchange models and the predicted values are found to be consistent with our experimental result. On the other hand, the spin-orbit forces seem to be explained well by the quark model rather than the meson-exchange models. From our experimental results, we established that the existing meson-exchange models can not explain the LS force but the quark model can. We derived the spin-spin force from new experimental data, and obtained the consistent value with the previous ${}^{7}_{\Lambda}$Li data. However the ${}^{10}_{\Lambda}$B ground-state data suggested different values of Δ. Therefore more experimental information on the p-shell hypernuclei and more theoretical studies are necessary. This implies that there is additional physics beyond the parameterization used.

Acknowledgements

The author would like to acknowledge E930('01) collaborators and any persons who supported, advised and encouraged the author to complete present work. The author would like to acknowledge all persons who made her life comfortably during experimental setup and the beam time in Brookhaven.

The author would like to express her sincere gratitude to Prof. Hirokazu Tamura who is her supervisor and the spokesperson of the Hyperball project. He invited the author to this project and gave her a lot. He has shown her the earnest attitude against experiments and physics.

She would like to thank Dr. H. Hotchi, Dr. H. Akikawa and Dr. K. Tanida. They gave her useful advice and taught her about experiments and analysis extensively from an elementary thing. She would express her great appreciation to Mr. Y. Miura and Mr. K. Mizunuma for their contribution in the experiment and their discussion. The author is deeply grateful to above persons who stayed BNL for a long time with her. She could not work pleasantly and joyfully without them.

The author is grateful to Prof. O. Hashimoto for his valuable support and encouragement continuously from when she was under graduate student. He guided her to the experimental nuclear physics. The author would like to thank Prof. K. Imai. He rendered efforts to construction of Hyperball. The author wish to express to Prof. T. Kishimoto, Dr. S. Ajimura, Ms. S. Minami and Mr. T. Hayakawa for their contribution to the experimental setup, DAQ system and start up of the experiment. The author would like to thank Dr. H. Takahasi. He helped during the severe beam time schedule. She would like to thank Ms. A. Banu for her contribution in the beam time and for her advice. She would like to thank Dr. R. E. Chrien and Prof. M. May. They gave her precious advice of physics. She would like to thank A. Rusek for his general support for the experiment and the life at BNL. He provided the author with the comfortable life. She would like to thank Dr. P. Pile for operation of D6line to deliver excellent kaon beam and for support of the beam analysis. She would like to thank Prof. J. Franz, Dr. D. E. Alburger, Dr. R. Sutter, Mr. R. Wall and Mr. E. Myer for their contribution to the idle detectors in D6-line revived and other detectors reconstruction. She would like to thank Prof. B. P. Quinn and Prof. G. B. Franklin for their contribution to the data acquisition system and the off-line analyzer. She is indebted to Prof. T. Nagae, Prof K. Nakazawa, Prof. S. N. Nakamura, Prof. L. Tang, Dr. Y. Sato, Dr. T. Miyashi Dr. L. Yuan, and Mr. Y. Okayasu for their valuable support of the experiment. She is appreciative of all stuffs of BNL, especially stuff of AGS and HEEP.

The author would also express those persons who support my work in Sendai, Dr. T. Takahashi, Dr. Y. Fujii, Mr. M. Kato and Ms. N. Kawamura. She would like to thank Mr. K. Miwa for his advice of Hyperball analysis.

She would also like to thank Prof. D. J. Millener for his valuable advice and discussion as well as theoretical calculations.

Last of all, the author would like to thank Hyperball, all the detectors and the magnets in D6-line, AGS and BNL.

This work is partially supported by Research Fellowship of the Japan Society for the Promotion of Science for Young Scientists.

Bibliography

[1] M. Bedjidian *et al*, Phys. Lett. **62B** (1976) 467.

[2] M. Bedjidian *et al*, Phys. Lett. **83B** (1979) 252.

[3] A. Gal, J. M. Soper, and R. H. Dalitz, Ann. Phys. (N.Y.) **63** (1971) 53.

[4] A. Gal, J. M. Soper, and R. H. Dalitz, Ann. Phys. (N.Y.) **72** (1972) 445.

[5] A. Gal, J. M. Soper, and R. H. Dalitz, Ann. Phys. (N.Y.) **113** (1978) 79.

[6] D. J. Millener *et al.*, Phys. Rev. C **31**, (1985)499.

[7] D. J. Millener, Proc. Int. Conf. on "Hypernuclear Physics with Electromagnetic Probes" (HYPJLAB99), Hampton (1999).

[8] D. J. Millener Proc. Int. Conf. on "Hypernuclear and Strange Particle" (HYP2003), Jlab., (2003), Nucl. Phys. A to be published.

[9] H. Tamura *et al.*, Phys. Rev. Lett. **84** (2000) 5936.

[10] K. Tanida ,Ph. D. dissertation, University of Tokyo, 2000.

[11] R. E. Chrien *et al.*, Phys. Rev. C **41** (1990)1062

[12] H. Akikawa *et al.*, Phys. Rev. Lett. **88** (2002) 082501, and
H. Tamura *et al.*, Proc. Int. Conf. on "Hypernuclear and Strange Particle" (HYP2003), Jlab., (2003), Nucl. Phys. A to be published.

[13] H. Akikawa ,Ph. D. dissertation, University of Kyoto, 2003.

[14] M. May s*et al.*, Phys. Rev. Lett. **51** (1983) 2085.

[15] K. Tanida *et al.*, Phys. Rev. Lett. **86** (2001) 1982.

[16] H. Kohri *et al*, Phys. Rev. C **65** (2002) 034607.

[17] V. N. Fetisov Nucl. Phys. A **691** (2001) 101c

[18] Y. Akaishi *el al.*, Phys. Rev. Lett. **84** (2000) 3539.

[19] O. Hashimoto *et al.*, Nucl. Phys. A **639** (1998) 93c.

[20] P. Pile *et al.*, Phys. Rev. Lett. **66** (1991) 2585.

[21] W. Bruckner *et al.*, Phys. Lett. **62** B (1978) 157.

[22] H. Tamura , Ph. D. Dissertation, Univ. of Tokyo.

[23] K. Itonaga *et al.*, Prog. Theor. Phys. Suppl. **117** (1994) 17.

[24] S. Fujii *et al.*, Phys. Rev. C **66** (2002) 054301.

[25] S. Cohen and D. Kurath, Nucl. Phys. **73** (1965) 1.

[26] T. Motoba private communication.

[27] D. J. Millener private communication.

[28] D. H. Davis, LAMPF Workshop on (π, K) Physics, AIP Conf. Proc. **224** (1991) 38.

[29] L. Majling *et al.*, Czech. J. Phys. **42** (1992) 1197.

[30] V. N. Fetisov, L. Majling, J. Zofka and R. A. Eramzhyan, Z. Phys. A**339** (1991) 399.

[31] E. Hiyama *et al.,* Phys. Rev. C **59** (1999) 2351.

[32] T. Motoba Prog. Theor. Phys. **70** (1983) 189.

[33] E. Hiyama *et al.,* Phys. Rev. Lett. **85** (2000) 270.

[34] P. H. Pile *et al.*, Nucl. Instr. Meth. A **321**,(1992)48.

[35] http://server.c-ad.bnl.gov/esfd/d6.html

[36] V. Sum *et al.*, Nucl. Inst. and Meth. A **321** (1992) 48.

[37] A. G. A. M. Armstrong, C. P. Riley, J. Simkin, *Three Dimensional Computer Program (TOSCA) for Non-Linear Electromagnetic Fields*, RL-81-07057, May 1982.

[38] S. Ajimura, http://km.phys.sci.osaka-u.ac.jp/ ajimura/mem/

[39] Hasegawa *et al.*, Phys. Rev. C **53** (1996) 1210.

[40] M. Juric *et al.*, Nucl. Phys. **52B** (1973) 1.

[41] R. H. Dalitz and A. Gal, Ann. Phys. **116** (1978) 167

[42] A. Gal, Phys. Rev. C **28** (1983) 2186.

[43] R. H. Dalitz and A. Gal, Ann. Phys. **116** (1978) 167.

[44] L. de Bever *et al.*, Phys. Rev. Lett. **80** (1998) 3924.

[45] T. Motoba *et al.*, Nucl. Phys. A **489** (1988) 683.

[46] J. Sasao *et al.*,Phys. Lett. B **579** (2004) 258.

[47] S. Ajimura *et al.*, Phys. Rev. Lett. **86** (2001) 4255.

[48] D. J. Millener, Nucl. Phys. A **691** (2001) 93c.

[49] Th. A. Rijken, V. G. J. Stoks, and Y. Yamamoto, Phys. Rev. C **59** (1999) 21 and references there in.

[50] O. Morimatsu *et al.*, Nucl. Phys. A **420** (1984) 573.

[51] Y. Fujiwara, C. Nakamoto, and Y. Suzuki, Phys. Rev. Lett. **76** (1996) 2242.